SCANNING TUNNELING SPECTROSCOPY ON ORGANIC MOLECULES

A Thesis

Submitted to the Faculty

of

Purdue University

by

André P. Labonté

In Partial Fulfillment of the

Requirements for the Degree

of

Doctor of Philosophy

May 2002

This thesis is dedicated in memory of,

Janice Lynn Dent Labonté
(December 10, 1969 to November 1, 1999),

my loving wife and a terrific mother.

ACKNOWLEDGMENTS

I would like to thank Professor Ronald Reifenberger for his continued support and encouragement over the last four years. He stood by me during my time of greatest need two years ago, after the passing of my wife, Janice. Ron has honed my critical thinking skills and continues to teach me the importance of words and writing. Thank you Ron.

Special thanks go to Dr. Bala Kasibhatla, Professor Clifford Kubiak, Steve Tripp, Professor Alex Wei, Elwyn Shelly and Dr. Jon Preece for synthesizing the molecules and samples used in this research.

I would also like to thank Professor Supriyo Datta, Dr. David Janes, Dr. Takhee Lee and Scott Crittenden for many stimulating discussions and helpful suggestions.

This work was supported by an ARO AASERT Grant to augment contract DAAL03-G-0144 and an ARO/NSF Grant 37584-PH.

TABLE OF CONTENTS

Page

Page

LIST OF TABLES

Table Page

LIST OF FIGURES

Figure Page

Figure Page

Figure Page

Figure Page

Figure Page

Figure Page

Figure Page

ABSTRACT

Labonté, André Paul. Ph.D., Purdue University, May 2002. Scanning Tunneling Spectroscopy On Organic Molecules. Major Professor: Ronald Reifenberger.

Scanning Tunneling Spectroscopy was performed on a number of organic molecules. Current-Voltage response, I(V), and dynamic conductance, dI/dV, data were collected using new systematic techniques. The new techniques are understood in terms of known theories [1] and provide a means by which a scanning tunneling microscope (STM) can perform reproducible two-terminal electrical measurements on an organic film. In particular, STS clearly discerns the relative conductivity (resistivity) of organic films.

The I(V) and dI/dV data collected demonstrate that the conductivity of organic molecules may be changed in a variety of ways, including: altering molecular endgroups, altering morphology, a chemical doping event, altering the orientation of an internal component of the molecule. It has also been demonstrated that organic molecules can exhibit conducting, semiconducting and insulating behaviors. Through measurements performed on the dI/dV data, a table of conduction gaps and E_f - HOMO has been tabulated for the molecules studied. In certain instances (see Chapter 7), molecular resistances have been estimated from the I(V) data.

In summary, this body of work firmly establishes that STS provides a useful tool in the study of the electrical properties of molecular films. Additionally, it has been shown that organic molecules exhibit a broad range of electrical behaviors and that these behaviors can be controllably altered.

INTRODUCTION

1.1 Background

Computers and electronics have revolutionized our world and our lives. Their unique speed and power make them valuable tools in the solution of many of our technical needs and problems. As time progresses, the capabilities of electronic circuits are expanding. Researchers are exploring the use of novel materials combined with electronics to solve problems in robotics, medicine, artificial intelligence, gas sensors, and a host of other applications. Many of these afore mentioned areas of research require electronic systems that mimic the capabilities already present in humans and animals. Therefore, it seems only logical to look toward biological and organic systems to find solutions to newfound problems. Imagine a pair of night visions goggles that work as well as a lion's eyes, or a chemical gas sensor equal to a dog's nose or a robot capable of performing like an Olympic gymnast.

Biologist have been able to explain how these biological systems function but engineers have been unable to reproduce their performance. One of the major obstacles faced by engineers is the current inability to effectively and efficiently probe and manipulate the nanometer-scale "building blocks" (i.e. organic molecules) of biological systems. Consequently, the development of cost-effective techniques of probing and manipulating systems on the nanometer scale is paramount to solving many of the proposed engineering challenges of the future. Scanning probe microscopes have been used extensively to probe nanostructured materials and molecules.[1-14] In particular, scanning tunneling microscopes (STM) have been used to probe the conduction properties of organic molecules[1,4,11,12] through a process know as scanning tunneling spectroscopy. [2]

Selecting the correct building blocks is important. Organic molecules provide an immense array of building blocks that all exist on the nanometer scale. Self-assembled monolayers (SAMs) of thiols

and dithiols on metal and semiconductor surfaces have attracted significant interest because of their potential use in nanoscale functional devices[15-25]. Electronic conduction through "molecular wires" has been studied [1,4,5,11,12,14,26-31] and theoretical models have been advanced [1,32-41] in attempts to understand electron transport through molecules.

As molecule-based nanoscale electronic circuits increase in complexity, new organic compounds will be required to fulfill new performance requirements. Several needs that are emerging are: 1) Probing Techniques; a basic, fast and cost effective technique of probing the electrical conductivity of organic nanostructures is needed. This technique will be especially useful if it can be modeled and understood. 2) Nano-Passivation; a nanoscale replacement for SiO_2 is needed to provide electrical insulation to isolate components of the circuit. Additionally, it is desirable that the thickness and/or resistance of the passivating molecule can be controlled. 3) Molecular Doping; molecules with conductivity that can be changed by the introduction of a dopant provides increased flexibility in architecture. 4) Information Library; a library of basic information on organic molecules is need. In particular, conduction spectrum and conduction gap information on organic molecules are useful if circuits are to be designed using these molecules as the primary building blocks.

The research presented in this thesis is centered around organic molecules that potentially fulfill one or more of needs listed above. STS work started by Dorogi et. al. [4] and continued by Hong et. al. [12] and myself has resulted in the development of a useful technique for probing the conductance spectra of organic molecule films. Resorcinarene molecules synthesized by Steve Tripp under the guidance of Professor Wei (Department of Chemistry; Purdue University) have been studied as molecular electrical insulators. Benzene-based thiol molecules that form charge complexes with tetracyanothylene (TCNE) have been studied for their molecular doping properties. The benzene based molecules were synthesized by Bala Kasibhatla under the direction of Professor Kubiak (Department of Chemistry & Biochemistry; University of California San Diego). Alkane-esters were synthesized by Elwyn Shelly under the direction of Professor Preece (Haworth School of Chemistry, University of Birmingham, U.K.) Alkane-esters are of interest because they contain variable chemical

functionality in their geometric center which in turn leads to conduction differences. Finally, through the work above, a library of conductance gap information on these organic molecules has been compiled.

1.2 The STS Niche

"Where does STM and STS fit into the picture of molecular electronics and why are they useful?" A prime difficulty associated with molecular electronics is the intrinsically small scale (nanometers) of molecules. Scanning tunneling microscopes provide one of the best current means of "seeing" and manipulating nanometer scale objects. The advantages to this approach are many:

- Availability: STMs are relatively easy to construct and numerous commercial versions are available. Also, anyone with an STM can perform the experiments presented herein.
- Non-intrusive: If done carefully, STM does not intrude upon or destroy the sample allowing further processing and probing to be performed on the sample.
- Very General: STMs are capable of probing the electrical conductivity of any nanometer scale object placed on a surface and is not limited to organic or molecular systems.
- Substrate Variability: The only requirement for STM is a conducting or semiconducting substrate.
- Simple Sample Preparation: Using an STM to perform spectroscopy and conductivity measurements only requires the sample to be placed on a surface. Complicated fabrication techniques are avoided using this method.
- Chemical/Conductivity Sensing: STS is highly sensitive to changes in the density of states of the sample on an atomic scale. Consequently, changes in electrical properties of nanoscale objects are easily probed. As will be shown, this can include the detection of a change due to a chemical event.
- Variable Environment: STM and STS can be performed in a variety of environments including variable pressure, variable temperature, alternative gasses and even in solutions.

The disadvantages to this approach are:

- One "Bad" Contact: It is perpetually difficult to precisely characterize the tip-sample contact. The presence of a vacuum tunnel barrier makes absolute conduction measurements difficult at best.

- Flat Samples: STM requires relatively flat samples and is best used on uniform samples such as self-assembled monolayer* (SAMs) forming molecules. A self-assembled monolayer (SAM) refers to a surface monolayer of atoms or molecules that have ordered themselves in a uniform layer on the surface of a substrate. SAM forming molecules are molecules that naturally form a SAM on a particular substrate surface.

Based on these lists it is evident that STM and STS are highly useful in performing a variety of probing experiments at the nanoscale level. Even when absolute conduction measurements are required, STM can be used to perform "screening" experiments where potentially useful molecular circuit elements are identified and characterized. Once the general properties of a molecule or subset of molecules are probed and identified using STS, other more fabrication-involved techniques can be used to obtain absolute conductance. Also, if an independent feedback system (i.e. a feedback system not dependent on sample conductivity; see Chapter 4) for STM can be developed, then it will be possible to eliminate some of the difficulties associated with STS.

1.3 What's New

"How does this body of work improve or increase our knowledge of molecular electronics?" My predecessor, Seunghun Hong, developed some of the basic techniques which I in turn used in performing my experiments. However, Hong's work was generally restricted to studying classes of relatively conducting molecules.[12] In particular, Hong studied several molecules with different endgroups (mono- and di-, thiols and isocyanides) and showed that endgroups have significant effects on molecular conductivity. Additionally, he examined mono and dithiol versions of the same molecule and showed that one method of changing the conduction of an organic molecule is to alter its endgroups. The questions arises: "What other methods can be used to change the conduction of an organic molecule?" My work has expounded upon this question and I have been able to show that the conduction of an organic molecule can be changed by:

- changing the morphology of the molecule on the surface.
- a chemical doping event.

- altering the orientation of a small internal component of a molecule (i.e. altering the position of a small number of atoms in the center of the molecule).

Additionally, I have been able to demonstrate that organic molecules can exhibit conducting, semiconducting and insulating behavior.

1.3.1 Inducing Conduction Changes by Changing the Morphology of a Molecule

Datta et.al.[1] established that conduction through organic molecules in an STS experiment occurs via electron tunneling. Simmons et.al.[42] established that in a tunneling experiment the tunneling current depends exponentially on the barrier width (see equation 3.2). Additionally, as stated above, Hong et.al.[12] established that the molecular endgroups and thus the tip-sample electronic coupling have significant effects on molecular conduction. A change in the morphology of a molecule changes both its physical height and the atoms of the molecule (i.e. the endgroup) presented to the probing STM tip. Consequently, it is expected that the morphology of a molecule will significantly change its electronic conduction as measured by STS.

Bumm et.al.[5-7] has already shown that similarly structured molecules (alkanethiols) with different heights alters electrical conductivity of the molecules in a manner consistent with Simmons predictions. Additionally, I have studied the conductance spectra (i.e. I(V) response) of alkanethiols and shown that conduction depends on the alkane-chain length (see Chapter 7). However, these studies look at "similar structured" molecules of different height, not the same molecule with two different orientations. In this thesis data is presented that demonstrates that the conductivity of a molecule changes when its physical orientation on a surface is changed (see Chapter 6 for full details). Tetramethyl xylyl dithiol, TMXYL (see Figure 6.4), was examined in an "Upright" and a "Flat" orientation as shown in Figure 1.1 (also see Figure 6.5). As a result of the morphology change between TMXYL-upright and TMXYL-flat, both the physical height and the "endgroup" presented to the STM tip are changed. Figure 1.2 (also see Figure 6.10) shows I(V) and dI/dV data taken on both orientations of TMXYL. A factor of 5 to 10 change in conductivity is evident from the dI/dV data

(consistent with Simmons[42]), thus establishing that the morphology of a molecule effects its electrical conduction (see Chapter 6 for full details).

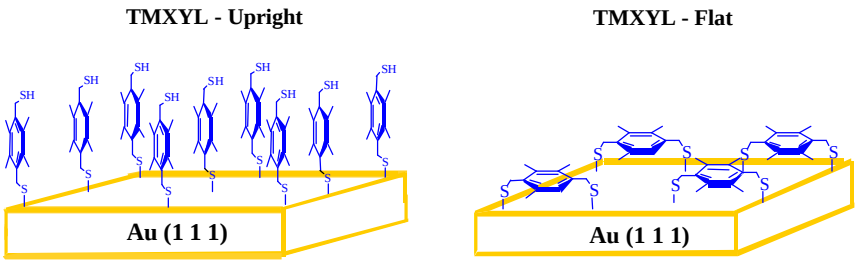

Figure 1.1

A schematic of TMXYL-upright and TMXYL-flat. TMXYL-upright is single-thiol bonded to Au(111) with an upright orientation. TMXYL-flat is in a horizontal orientation, indicative of a molecule bonded to the Au(111) substrate via both thiol end-groups. RAIRS (Table 6.1) confirms the orientations of the molecules and the height changes observed using elipsometry are consistent with the calculated height changes (see Table 6.2).

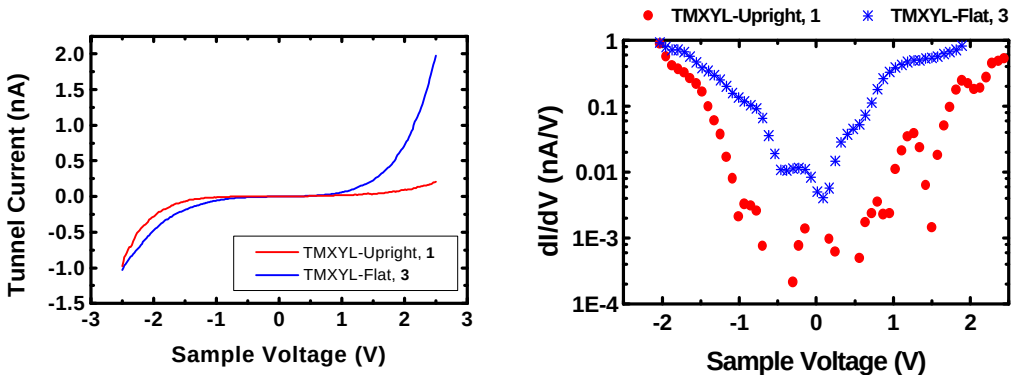

Figure 1.2

I(V) data from TMXYL clearly shows that TMXYL is an insulator for small bias voltages regardless of orientation. The reduced conductivity of TMXYL-Upright, **1**, relative to TMXYL-Flat, **2**, is due to the increased height of **1** relative to **2**.

1.3.2 Inducing Conduction Changes Through the Use of a Chemical Doping Event

Appelbaum et.al. and Feuchtwan et.al.[43,44] demonstrated that electrical conduction through a system is dependent upon the density of states (DOS) of the system. Thus, if the DOS of a molecule is changed, then its electrical conduction should also change. Prof. Kubiak (Department of Chemistry & Biochemistry, University of California, San Diego) suggested that the formation of a charge-transfer (CT) complex between an electron donor and an electron acceptor, could significantly modify the energy state configuration of the electron donor. The change in the energy state configuration of the donor should result in a measurable change in the electrical conduction of the molecule. To test this hypothesis, TMXYL-flat, an electron donor, was doped with Tetracyanoethylene (TCNE; see Figure 6.3), an electron acceptor (see Chapter 6 for full details). I(V) were measured on TMXYL with and without the TCNE present (see Figure 1.3 and Figure 6.8). This data clearly shows a change in the low-bias (V_{bias} < 0.5V) behavior of the TMXYL. TMXYL changes from insulating to conducting behavior when the CT complex with the TCNE is formed. The key result is that the electrical conduction of a molecule can controllably be changed through the use of a chemical doping event.

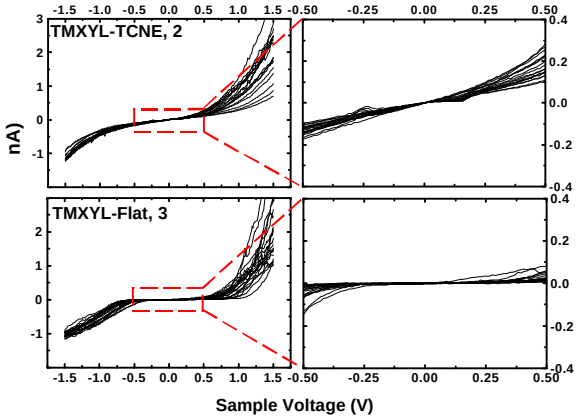

Figure 1.3

I(V) data from TMXYL-TCNE indicates that the CT complex is an electrical conductor, with a nearly linear I(V) behavior at V=0. When the TCNE molecule is removed, I(V) data from TMXYL-flat indicates that for small voltages (|V| < 0.5V), TMXYL is an electrical insulator. This data combined with the I(V) data on TMXYL-TCNE indicates that the change from insulator to conductor through the formation of a CT complex results from a change in the molecular energy levels. Approximately 25 separate I(V) spectra, taken from various regions across the sample, are plotted simultaneously to indicate the overall reproducibility of the data. The data have been reproduced on two separate samples.

1.3.3 Inducing Conduction Changes by Altering Internal Components of a Molecule

Above, we have already discussed a number of methods for changing the configuration of a molecular system. The question then arises: "can the electrical conduction of a molecule be change if a few of its atoms near the center (i.e. away from the contacts) are rearranged?" In this case, morphology and endgroups remain the same and chemical doping is not occurring, nor is the atomic composition of the molecule changing (i.e. number of atoms of each element remains constant). What is occurring is a change in the position of a "few" non-identical atoms near the "center" of the molecule. Quantum mechanics[45,46] predicts that the energy states of a system are highly dependent upon the detailed configuration of the system and that quantum mechanical effects dominate away from the classical limit (i.e. bulk materials). The implication is that if the positions a few atoms near the center of a molecule are switched, the electronic structure, and thus the conductivity of the molecule should also change. As a test of this hypothesis, two variations on an alkane-ester molecule were examined (see Figure 1.4 and Figure 8.1). The difference between the two molecules is the orientation of the ester group in the center of the alkane-chain; the endgroups, orientation and chemical composition of the molecules remains the same. Figure 1.5 (see also Figure 8.2) shows I(V) data taken on both molecules; significant changes in their conduction for positive bias voltages are evident; thus, demonstrating that the conduction of a molecule can be altered by changing a small internal component of the molecule (see Chapter 8 for full details).

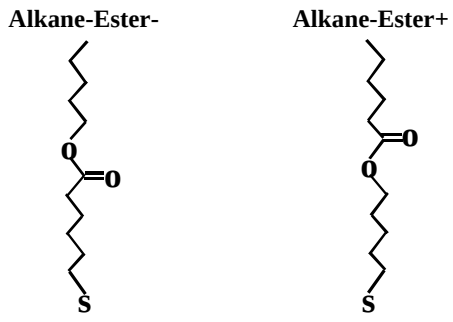

Figure 1.4

Schematic of Alkane-Ester- and Alkane-Ester+. The difference between the two molecules is the orientation of the ester group within the alkane chain.

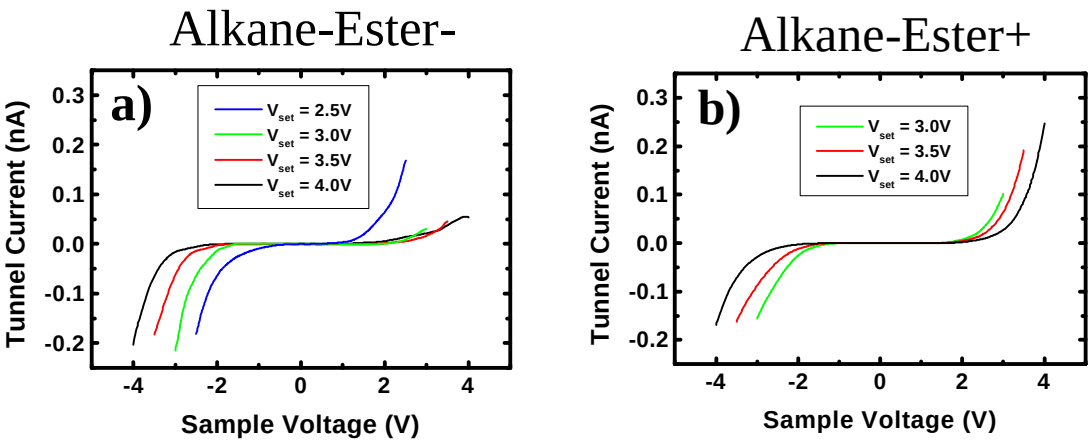

Figure 1.5

a) I(V) data for Alkane-Ester-. As V_{set} is increased above 2.5V, the current for high positive bias voltages is suppressed relative to negative bias voltages. **b)** I(V) data for Alkane-Ester+. As V_{set} is increased above 3.0V, the current for high positive bias voltages increases relative to negative bias voltages.

1.4 Summary

The contributions of this work to molecular electronics are two-fold: i) The method of scanning tunneling spectroscopy (STS) on molecular systems has been refined and new techniques have been developed. ii) Through the use of STS, it has been demonstrated that the conductivity of molecules can be changed in a variety of ways and that molecules can exhibit a variety of behaviors. These demonstrations will hopefully help form part of the foundation of molecular electronics in the future.

2. EXPERIMENTAL SETUP

All data was taken using a home-built Ultra-High Vacuum (UHV; pressure ≤ 1 x 10^{-9} torr) Scanning Tunneling Microscope (STM). The STM is inside a stainless-steel chamber; vacuum is maintained with ion pumps. Figure 2.1 is a picture of the vacuum chamber enclosing the STM head; this entire chamber floats on air pistons to isolate it from ground vibrations. Figure 2.2 is a labeled cross-section of the same chamber as depicted in Figure 2.1.

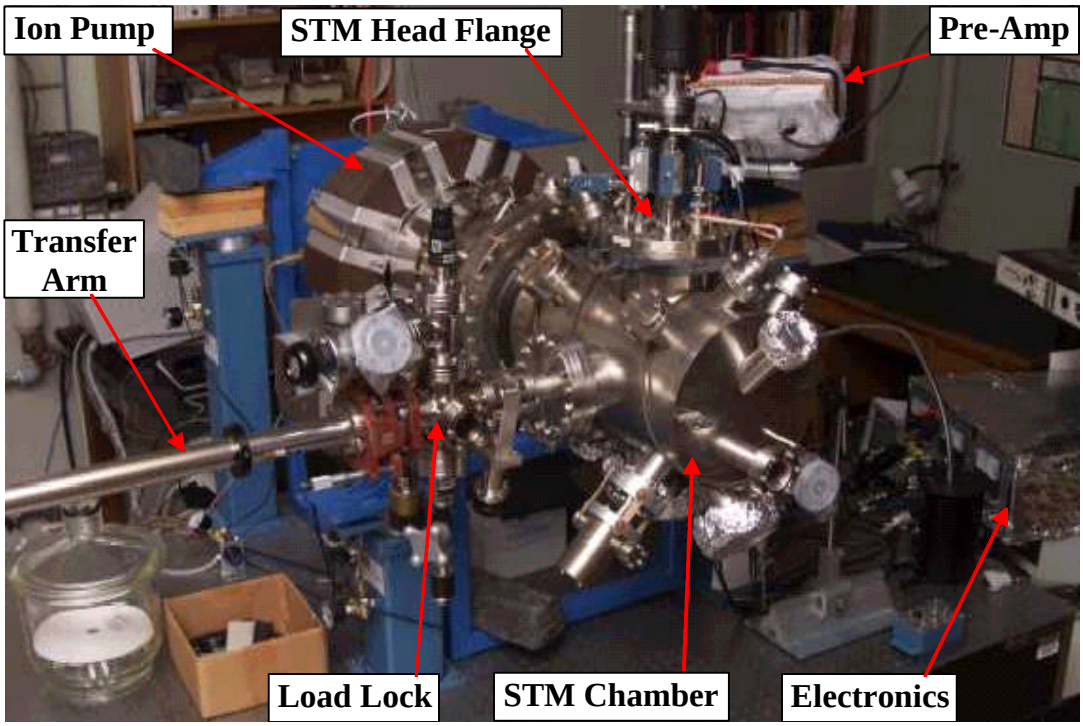

Figure 2.1

Picture of the UHV chamber that houses the home-built STM used for the experiments discussed in this thesis.

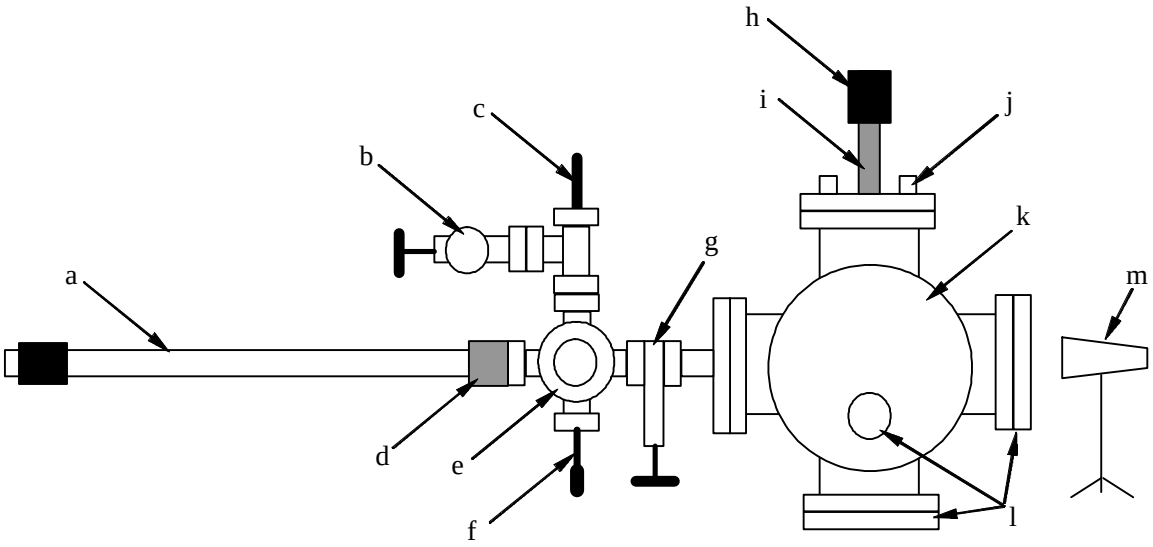

Figure 2.2

Cross-section of the STM chamber and its components; **a)** Linear Transfer Arm; **b)** Gate Valve; **c)** Sample Manipulator; **d)** Pivot Joint. **e)** Load Lock Chamber; **f)** Sample Holder Disk Manipulator; **g)** Chamber-to-Chamber Gate Valve; **h)** Support Hook Manipulator; **i)** Linear Head Translator; **j)** STM Head Wire Feedthrough; **k)** STM Main Chamber; **l)** Viewports; **m)** Course Approach Telescope.

Maintaining the samples and the STM in ultra-high-vacuum conditions serves two purposes. First, the UHV helps keep the sample and tip free from contamination which would effect the measurements. Since, in principle, the scanning tunneling spectroscopy experiments probe single molecules on the surface of a gold electrode, it is imperative that the surface of the sample be kept clear of contamination. Second, UHV conditions eliminate alternate electrical conduction paths (through a water meniscus or air breakdown), thus ensuring that the observed electron current is due to tunneling between the tip and sample.

Raising the chamber on air pistons is not sufficient to eliminate all "harmful" vibrations (as will be explained later). A spring-supported, three-stage, magnetically-damped isolation system is used to further eliminate mechanical vibrations. Figure 2.3 is a diagram of the STM head and its vibration isolation system. A piezo tube is used to control tip position and make topographic images.

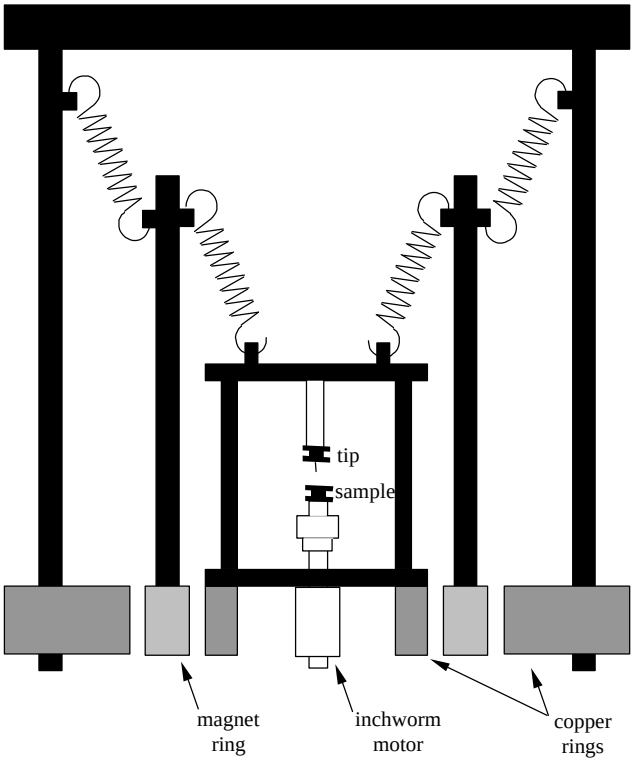

Figure 2.3

STM head and the spring-supported, magnetically damped, three-stage, vibration isolation system.

Scanning Tunneling Microscopes (STM's) acquire data by bringing a sharp metallic tip into close proximity (~ 1nm) to the surface of an electrically conducting sample[47,48]. Tip sample separation is maintained by a piezo tube. Signal inputs to the piezo tube are controlled by software designed to emulate a Proportional-Integral-Differential (PID)[50-52] feedback circuit. The feedback works in the following manner: a set voltage, V_{set}, and a set current, I_{set}, are specified. V_{set} is applied to the sample and the tip is approached (from a distance of several microns) until a tunneling current equal to I_{set} is obtained in the signal circuit. Once the tip is approached the feedback software controls the piezo tube so as to maintain I_{set}. Since the feedback is based upon the tunneling current, STM's are primarily sensitive to the local density of states at the surface of the sample and less sensitive to the surface morphology.

Figure 2.4 is a schematic of the STM control electronics. Data acquisition and feedback are provided by Universidad Autonoma de Madrid (UAM) Scanning Probe Software which is PC-based and requires the use of a Digital Signal Processor (DSP) card (Spectrum^{TM} model PC/C31). The PID feedback program (running in the DSP) takes the place of an actual PID feedback circuit. This program communicates with the general control/acquisition program running on the microprocessor of the PC. Control signals are determined by the programs running on the DSP and the PC; these signals are sent to the voltage amplifier, which in turn, applies the required voltage signals to the piezo tube. Additionally, the DSP applies a fixed voltage to the sample, this establishes a tunnel current between the sample and the STM tip. This current is fed into a Pre-Amplifier which converts the current into a voltage. The voltage representing the tunnel current is fed back into the DSP and used by the feedback program; thus, completing the feedback loop.

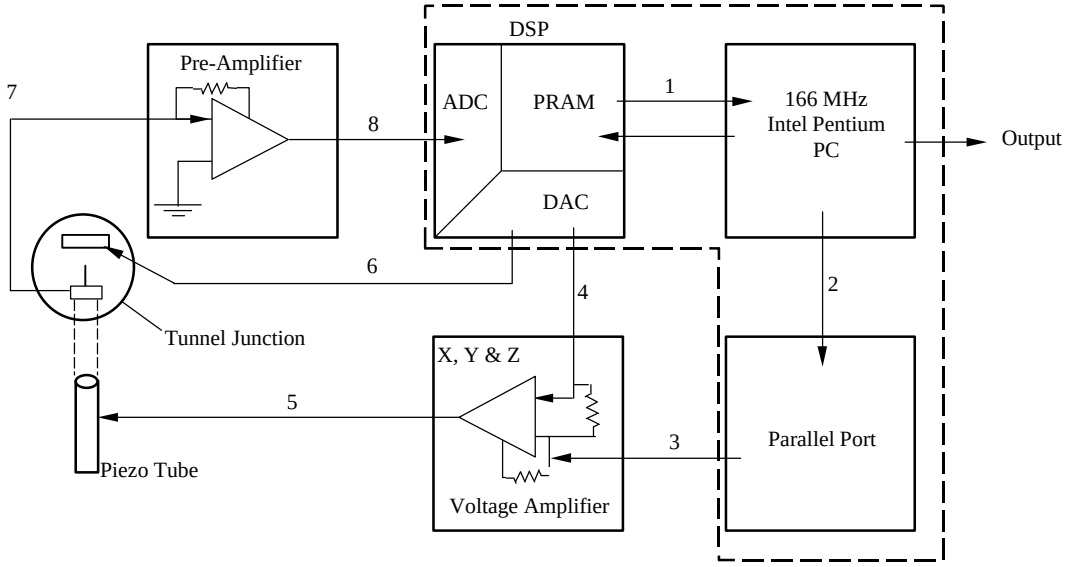

Figure 2.4

General schematic of the electronics used to control the STM. **1)** Communication between the PID feedback program running on the DSP and the control/acquisition program running on an IBM compatible PC. **2,3)** Gain and offset signals via the Parallel Port to the Voltage Amplifier. **4)** Feedback signals to the Voltage Amplifier. **5)** Voltage signals placed on the Piezo Tube. **6)** Set Voltage to the sample. **7)** Tunnel current goes from the sample to the STM tip, and then to a Pre-Amplifier. **8)** The voltage representing the tunnel current is fed back into the DSP.

The load lock chamber (see Figure 2.2**e**) serves two purposes: First, the load lock chamber allows the insertion of new samples and tips without venting the main STM chamber; this saves time and protects the STM from contamination and damage. Under normal operation, (i.e. when not inserting new samples and tips) the load lock chamber is maintained at a pressure of ~2 x 10^{-9} torr. Second, the load lock chamber is used to store samples and tips not currently under investigation in the STM chamber. Up to three samples and four tips may be stored in the load lock chamber at any one time. As with the main STM chamber, UHV helps keep the tips and samples free of contamination.

Tip and samples are mounted are special holders that are designed to be picked up by manipulator forks. The manipulator forks are mounted magnetically coupled linear translation arm (Figure 2.2**a**) that transfers the sample to and from the load lock chamber and the STM chamber. Within each chamber, vertically mounted linear translators (Figure 2.2 **f** and **i**) are used to lift and lower samples and tips onto the manipulator forks. Within the load lock chamber, the samples and tips are placed on a rotary disk (Figure 2.2**i**); this allows different samples and tips to be selected with the manipulator forks.

3. STM & STS THEORY

3.1 General STM

STM is performed by bringing a sharp metallic tip (in my experiments: 80% Pt, 20% Ir) close (0.5-2.0nm) to a conducting substrate (Figure 3.1). At this distance, there is significant overlap between the electron wave functions of the tip and substrate; the space between the tip and substrate (the vacuum gap) plays the role of a potential barrier (Figure 3.2). Treating the tip and substrate as ideal conductors with work functions φ_t and φ_s respectively, and assuming electrical equilibrium (i.e. aligned Fermi-levels), we arrive at an equilibrium energy diagram as depicted in Figure 3.2a. The slanted top of the potential barrier is a result of the work function difference between the two metal contacts.

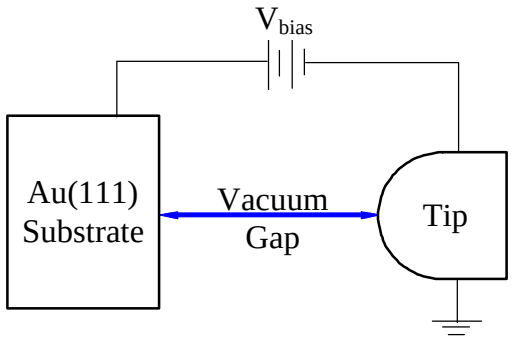

Figure 3.1

Schematic of STM tunnel junction.

a) Tunnel junction at zero bias **b)** Tunnel junction at V_{bias}

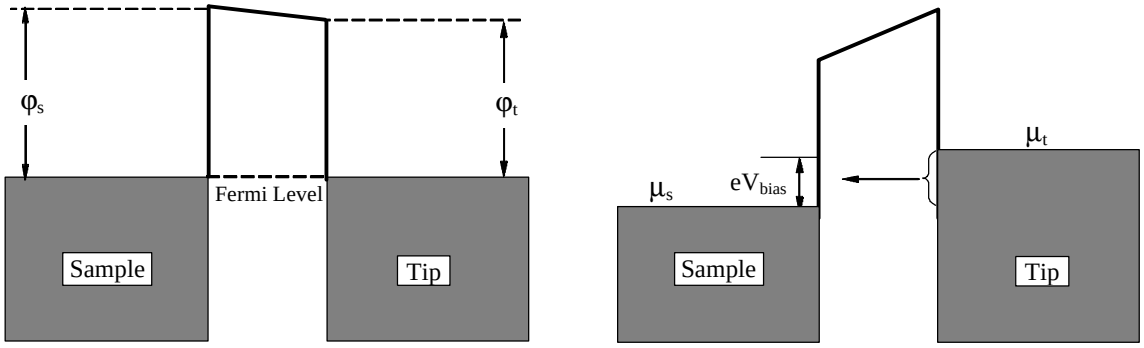

Figure 3.2

a) Energy Band diagram of STM tunnel junction at equilibrium. φ_s and φ_t are the workfunctions of the sample and tip respectively. **b)** Energy Band diagram of STM tunnel junction biased with a positive voltage, V_{bias}, relative to the sample. μ_s and μ_t are the chemical potentials (Fermi energies) of the sample and tip respectively.

If we bias the tunnel junction by placing a voltage, V_{bias}, onto the sample, a tunnel current is established. Electrons in the tip with energy between Fermi energies of the sample and tip (i.e. μ_s and μ_t) are free to tunnel into the unoccupied states of the sample's conduction band; this is illustrated in Figure 3.2b.

For a square potential barrier, the solution of Schrödinger's equation in the barrier region is of the form:

$$\psi \propto e^{-\kappa z} \tag{3.1}$$

Based on this and the Wentzel-Kramers-Brillouin (WKB)[46] approximation, it has been shown that for small applied voltages, the transmission probability, and thus the tunneling current, decays exponentially within the barrier[42]

$$I \propto e^{-2\kappa z} \tag{3.2}$$

In Equation 3.1 the decay constant takes the form:

$$\kappa = \frac{2\pi}{h}[2m\,\varphi]^{0.5} \tag{3.3}$$

where,

$$\varphi = (\varphi_s - eV_{bias} + \varphi_t)/2 \tag{3.4}$$

Given that: m = 9.10 x 10^{-31} kg = 5.11 x 10^5 eV/c^2, h = 4.136 x 10^{-15} eV·s, and most metallic work functions are ≈ 5 eV we get $\kappa \approx 10$ nm^{-1}. Consequently, for a 0.1nm change in tip-sample separation, the current changes by an order of magnitude. This in turn gives STM a "best" vertical resolution of 1.0 x 10^{-2} nm[47,48]. Lateral resolution is limited by the end-radius of the tip, which in theory is a single atom based on equations 3.2 and 3.3. Consequently, the "best" lateral resolution for an STM is on the order of 0.1nm[47,48]. However, in order to achieve this extraordinary resolution, it is necessary to place an extreme effort on vibrational isolation of the STM instrument; this is illustrated by the damped, three-stage, vibration isolation system depicted in Figure 2.3. Additionally, resolution is affected by the conductivity of the material and by tip artifacts; both are discussed in Chapter 4.

3.2 Scanning Tunneling Spectroscopy (STS)

Of particular interest to my work is the use of an STM as an instrument to perform spectroscopy on a variety of molecular samples. To do this, we must examine and understand the relationship between the tunneling current and the band structure of the sample. Tersoff and Hamann showed that the tunneling current is proportional to the local density of states (LDOS) of the sample.[53,54] To do this, Tersoff and Hamann made the following assumptions:

1) The tip has a uniform density of states. This is a good assumption for small energy ranges (i.e. low voltages) since the tip is always made of a highly conducting material such as Pt.
2) Tip-Sample interactions are weak, thus unperturbed wave functions for each may be used. This is a valid assumption given the normal tip-sample separation is on the order of 0.5 to 2.0nm.
3) The bias voltage is low (i.e. $V_{bias} \leq 1$ volt). This assumption is required for two reasons; the first is already stated as part of assumption 1. The second reason is to prevent the distortion of the

tunnel barrier so that the methods used in approximating the tunnel current (most notably, the WKB approximation) are valid. However, in practice, this assumption is often ignored since STM is often done at voltages greater then one volt. The effects of this are shown in more detail in Chapter 5.

4) In the tip, only s-wave functions are important.

Others have shown using the WKB approximation that the tunneling current can be expressed as:[43,44]

$$I = \int_{-\infty}^{\infty} [f(E-eV) - f(E)]\, \rho_s(z,E)\, \rho_t(z,E-eV)\, T(z, E, eV)\, dE \tag{3.5}$$

where:

f(E-eV)	= Fermi-Dirac distributions for the tip,
f(E)	= Fermi-Dirac distributions for the sample,
$\rho_t(z,E-eV)$	= density of states for the tip,
$\rho_s(z,E)$	= density of states for the sample,
$T(z, E, eV)$	= the transmission probability,
z	= the tip-sample separation,
E	= energy measured with respect to Fermi energy of the sample,
V	= V_{bias}

In the limit of low temperatures ($kT << eV_{bias}$; T = Temperature) we can treat the Fermi-Dirac distribution as a step function; consequently:

$$[f(E-eV) - f(E)] = \begin{cases} 1; & 0 < E < eV_{bias} \\ 0; & E < 0,\ E > eV_{bias} \end{cases} \tag{3.6}$$

Consequently, equation 3.5 may be rewritten as:

$$I = \int_{0}^{eV} \rho_s(z,E)\, \rho_t(z,E-eV)\, T(z, E, eV)\, dE \tag{3.7}$$

Thus we see that the tunneling current at any given voltage is dependent upon the density of states in the tip and sample and the appropriate transmission function for the tunnel barrier.

3.3 Molecular I(V)

Now that we have established the basics of STS theory, we can extend the theory to more complicated systems. Of particular interest is the tunneling current through a molecule; the tunnel junction with a molecule present is shown schematically in Figure 3.3a. For this new arrangement, the molecule takes the place of the vacuum tunnel barrier and the density of states in both the substrate and tip are assumed to be uniform. Applying these assumptions to equation 3.7 we obtain equation 3.8 given below.[32-35,37]

$$I = \frac{2e}{h}\int_{-\infty}^{\infty} dE\ T(E,V)[\, f(E-\mu_t) - f(E-\mu_s)] \tag{3.8}$$

Here μ_t and μ_s are the electrochemical potentials of the tip and substrate respectively (which are assumed to remain in local equilibrium), f(E) is the Fermi function and T(E,V) is the transmission function which can be calculated from a knowledge of the molecular energy levels and their coupling to a substrate. At room temperature, the Fermi-Dirac distributions are treated as exhibiting a sharp transition at μ_t and μ_s respectivly.[55] Consequently, equation 3.8 indicates that at room temperature the current is obtained simply by integrating the transmission function from μ_t to μ_s. The answer clearly depends on where μ_t and μ_s are located with respect to any structure in the transmission function produced by the molecular energy levels

Our present understanding of the current-voltage relation, I(V), for a molecule relies on a Landauer-Buttiker approach in which the conductance is estimated from the transmission probability of an electron through a molecule. This is the starting point for many calculations of the conductance spectrum (dI/dV vs. V). As discussed elsewhere,[1,36,38] two parameters, namely the equilibrium Fermi energy of the molecule and the voltage division of the applied bias across the molecule, are crucial in determining the conductance spectrum. Two molecules with identical energy levels can give rise to a totally different conductance spectra if these quantities are different due to the details of molecular bonding to different substrates.

Several limitations must be considered when using equation 3.8. First, the assumption made in applying equation 3.8 is that the density of states, DOS, of each of the contacts (i.e. the substrate and tip) are uniform. In reality, this is not accurate; however, examining the electron configuration of the metals used in the contacts, $[Xe]6s^{1}5d^{9}$ for the Pt tip and $[Xe]6s^{1}5d^{10}$ for the Au substrate,[56] we see that electrical conduction through both metals are dominated by 6s electrons leading to the free-electron model for metals and thus the "uniform DOS" assumption.[57] If variations in the density of states of the contacts become a concern, then the effects can be included as part of T(E,V). The second consideration is that equation 3.8 implicitly neglects inelastic scattering and assumes that elastic scattering processes dominate the tunnel current.[34] Finally, equation 3.8 is a one-dimensional approximation to the three-dimensional STM tunnel junction; however, the implications of equation 3.2 justify this approximation.

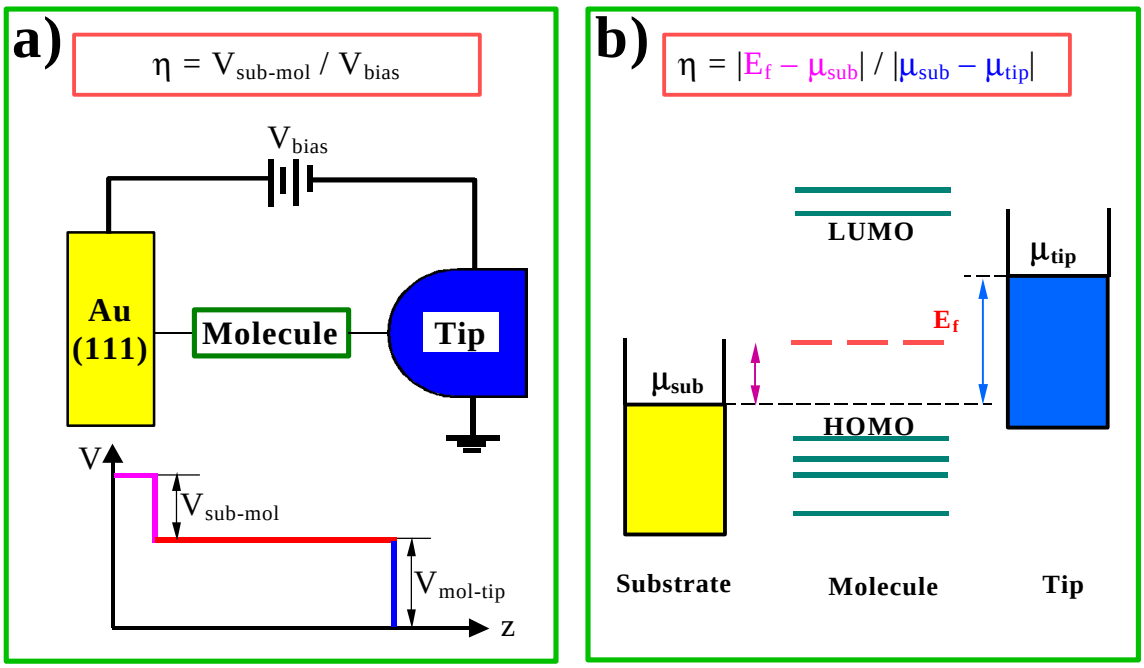

Figure 3.3

a) Tunnel Junction and Voltage profile. **b)** Corresponding Energy Diagram

In STM experiments, the lowest order of approximation assumes that the molecular energy levels simply float up by an amount $eV_{sub\text{-}mol}$ equal to the average electrostatic potential in the molecule.[1] More conveniently, the molecular energy levels can be considered as a fixed reference and the substrate can float down by $eV_{sub\text{-}mol}$ so that the electrochemical potentials in the substrate, μ_s, and in the tip, μ_t, can be written as (see Figure 3.3b):

$$\begin{aligned} \mu_s &= E_f - eV_{sub\text{-}mol} \\ &= E_f - \eta eV_{bias} \end{aligned} \tag{3.9}$$

$$\begin{aligned} \mu_t &= E_f + eV_{bias} - eV_{sub\text{-}mol} \\ &= E_f + (1 - \eta eV_{bias}) \end{aligned} \tag{3.10}$$

In equation 3.9 and equation 7.3, E_f is the equilibrium Fermi energy and the factor η describes how the electrostatic potential difference, V_{bias}, is divided between the two junctions: $\eta \equiv V_{sub\text{-}mol}/V_{bias}$. In STM measurements this factor can be made close to 0.5, since, in order for the current to be measurable, the probe has to be within a few angstroms of the molecule which is comparable to the molecule's distance from the substrate.

We find this parameter, η, to be a useful way to describe the potential profile especially for short molecules where the electric field inside the molecule seems to have a minimal effect on the conductance spectrum.[1] For longer molecules the electric field inside the molecule may play a more significant role depending on the internal structure of the molecule. Also, at high bias, change in the charge density ($\delta\rho$) inside the molecule can be significant and its contribution to the potential profile leads to an effective decrease in the value of η.

4. EXPERIMENTAL PROCEDURES

4.1 Topography Data

Using a scanning tunneling microscope (STM), two primary types of data are taken: topography images and I(V) data. A topography image is taken by rastering the tip across the sample surface while maintaining a constant I_{set}. By monitoring the Z-piezo voltage, we get a direct measure of surface morphology, assuming uniform surface density of states and conductivity (Figure 4.1a). If the surface conductivity and charge density are not uniform, the topographic data will not be a true measure of surface morphology but will be a reflection of the lateral conductivity variation across the surface of the sample (Figure 4.1b). Conduction variation effects on the topography images were minimized by using flat (111) Au substrates and uniform self-assembled monolayers (SAMs) of the desired molecules.

In addition to lateral variations in surface electrical conductivity, there are other tip artifacts to be considered. Tip artifacts result from the size and shape of the tip. Most common among tip artifacts is the softening of sharp features on small scale objects. A complete description of various forms of tip artifact associated with scanning probe microscopes is given by Westra[58] and references therein.

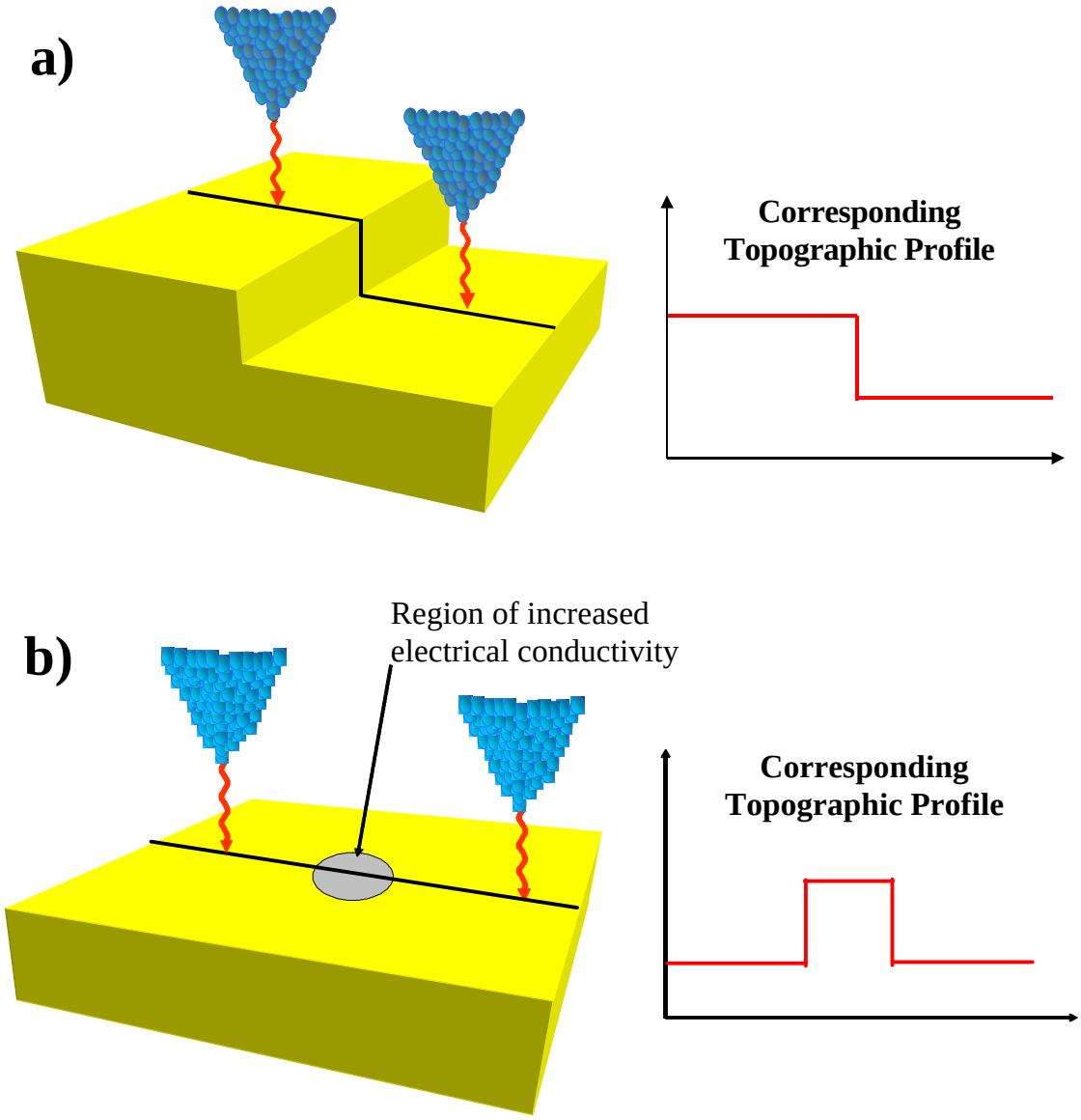

Figure 4.1

a) Topography under uniform surface conductivity conditions. The resulting topography trace maps the actual topography of the sample. **b)** Topography under non-uniform surface topography conditions. The resulting topography trace has an "artificial" plateau in the region of higher conductivity.

4.2 I(V) Data

The second form of data taken with an STM is I(V) data; which is obtained through a process called scanning tunneling spectroscopy (STS)[2,3,59]. I(V) data is taken by placing the STM tip over a specific spot on the sample. The feedback is shut off and tunnel current is measured as the sample voltage is ramped from V_{set} to $-V_{set}$.

Like the topography data, I(V) data is effected by the same issues discussed in the previous section. Consequently, in order to obtain repeatable and reliable results, it is important that I(V) data is obtained from flat monolayer surfaces. By doing this, the tunneling current is dominated by the tip-apex atom and the point on the sample directly below the tip-apex atom; thus, effects due to tip shape are minimized. Additionally, when making an I(V) measurement it is desirable to perform the measurement on a "single" molecule. This requires that the I(V) measurement be performed in less time then it takes the tip to laterally drift a distance equal to the radius of a single molecule. Typical drift rates (at room temperature) are on the order of 1nm/min or 2×10^{-2} nm/s. I(V) measurement take between three to five second which corresponds to a tip drift $\approx$ 0.06 to 0.1 nm. Of the molecules I have examined, dodecanethiol (DDT) has the smallest lateral radius (r_{DDT} = 0.21 nm)[13,60,61]. Clearly the STM tip drifts less then the radius of a molecule during the measurement of a single I(V).

Many of the plots of I(V) data shown in this paper are actually an aggregate of numerous voltage sweeps. To understand this we must examine the details of how I(V) data is taken; appropriate definitions are given in Table 4.1. These definitions will be used throughout this thesis. Additionally, Figure 4.2 schematically illustrates how the I(V) data is taken and Figure 4.3 provides the corresponding flow chart. The exact parameters used to take I(V) data are determined by what is required to obtain repeatable data without the loss of information.

Table 4.1

Definitions of I(V) data parameters.

Parameter	**Definition**
Voltage Sweep	A single sweep of the voltage from V_{set} to $-V_{set}$ (forward). or $-V_{set}$ to V_{set} (reverse).
I(V) data or I(V)	Average of "forward" or "reverse" Voltage Sweeps. Typically ~ 40 voltage sweeps per I(V). i.e. for a given voltage the corresponding Data Point from 40 Voltage Sweeps are average to create single I(V) Data Point. The I(V) Data Points are then assembled as a function of voltage to "build" the I(V).
forward	Refers to the Voltage Sweep from V_{set} to $-V_{set}$.
reverse	Refers to the Voltage Sweep from $-V_{set}$ to V_{set}.
Data Point	A single data point on a Voltage Sweep. 128, 256 or 512 Data Points per Voltage Sweep; usually 256. Each Data Point consists of an average of 3 to 8 measurements.
Measurement	For a given voltage, the current is recorded, resulting in a measurement.
I(V) Data Point	A single data point on the I(V) which is an average of Data Points from multiple Voltage Sweeps.

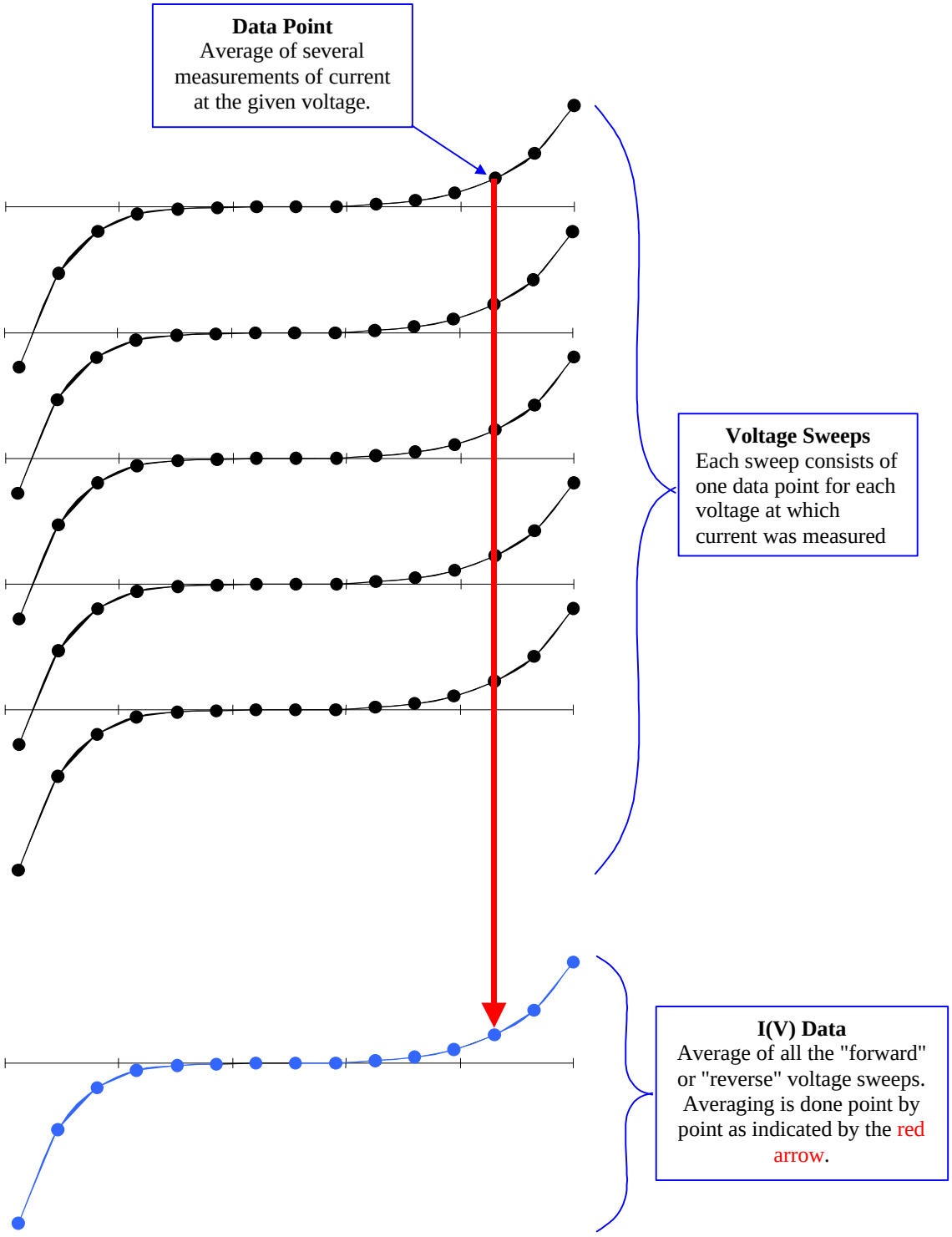

Figure 4.2

Schematic illustrating I(V) data acquisition process. This process is performed separately for the forward and reverse sweeps of the voltage bias.

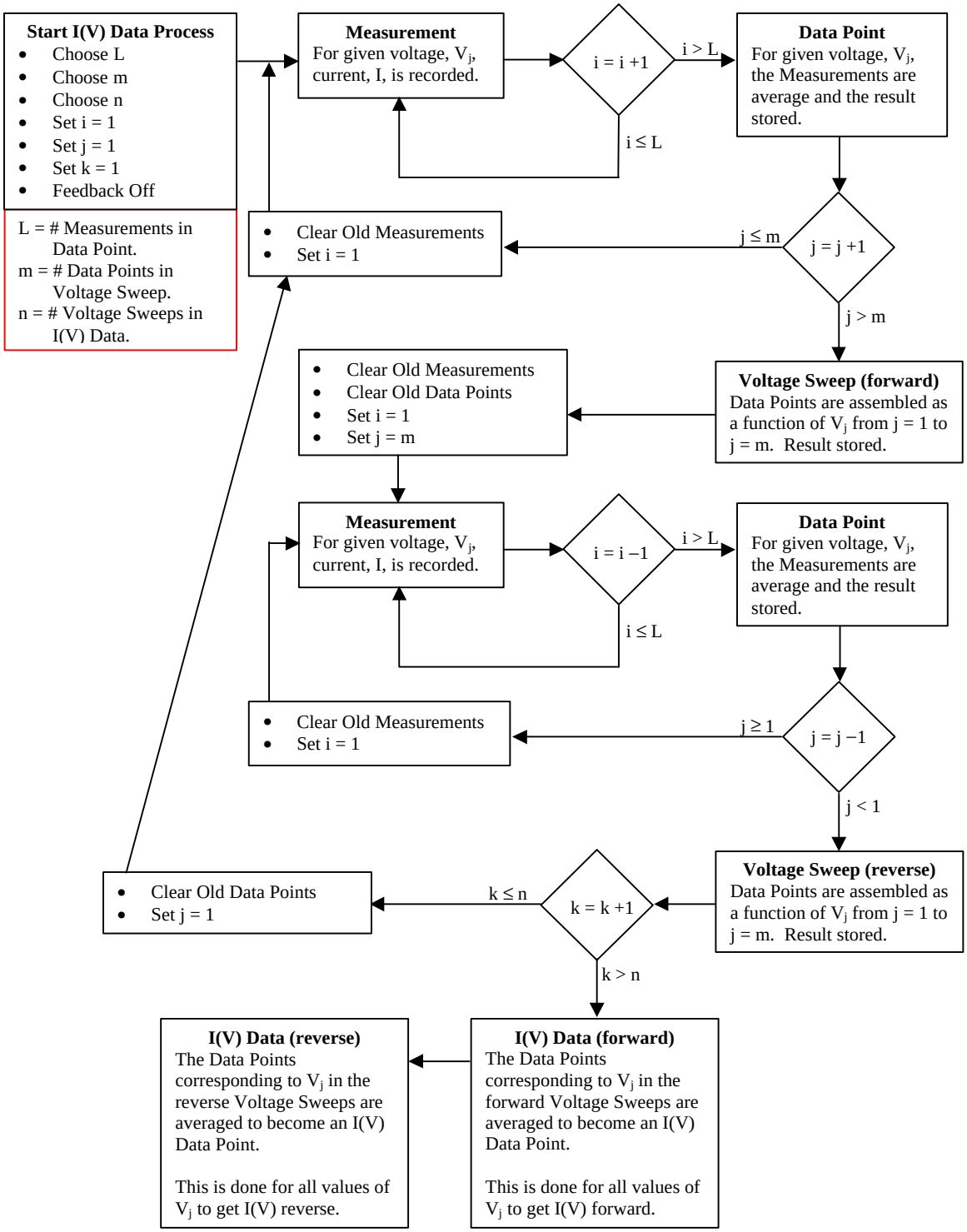

Figure 4.3

Flow chart outlining the steps taken in recording I(V) data.

4.3 Current Imaging Tunneling Spectroscopy

Current Imaging Tunneling Spectroscopy (CITS)[62] is a method of taking data where topography and I(V) are taken simultaneously; this is illustrated in Figure 4.4. A scan line (128 points) for the topography is taken by rastering the tip across the sample. The tip is moved back along the scan line and an I(V) is taken at each point along the topography scan line. When performing CITS, each I(V) consists of a single voltage sweep and each voltage sweep has 44 data points. The topography-I(V) correlation provided by this method provides a powerful diagnostic tool; in particular, regions of different local electronic structure can be identified. However, due to the low number of averages in the CITS I(V), the "normal" method of taking I(V) is a more reliable measure of the scanning tunneling conductance.

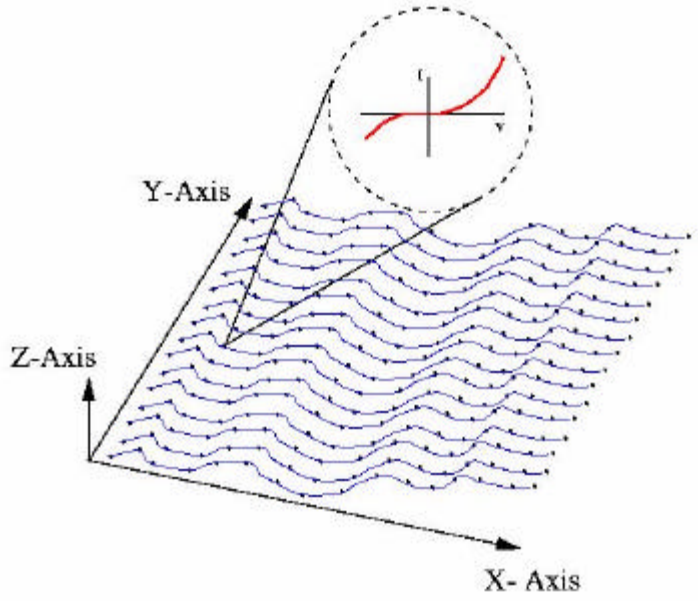

Figure 4.4

Schematic of how CITS data is taken. After a scan line is taken for the topography, an I(V) is taken at each point along the topography scan line.

4.4 Substrate Preparation & Characterization

All substrates consist of a layer of Cr (1-4 nm) and Au (200-300 nm) evaporated onto a borosilicate glass surface (thickness = 1.1 ± 0.1 mm; size = 11.0 x 11.0 ± 0.2 mm). Gold is the desired substrate, the chrome is for adhesion purposes. These samples are purchased from the Metallhandel Schröer GmbH company in Lienen, Germany.

Before use, all Au substrates are front-side propane flamed until bright red for two to three seconds. The purpose of the flaming is to clean the Au surface and make it flat. It is believed that the flat grain surfaces are Au (111)[10,63]. Once flamed, samples are batch characterized in a Park Scientific air STM; i.e. checked for flatness and contamination. Figure 4.5 is a topographic image of one of the substrates taken with the UHV STM described in Chapter 2.

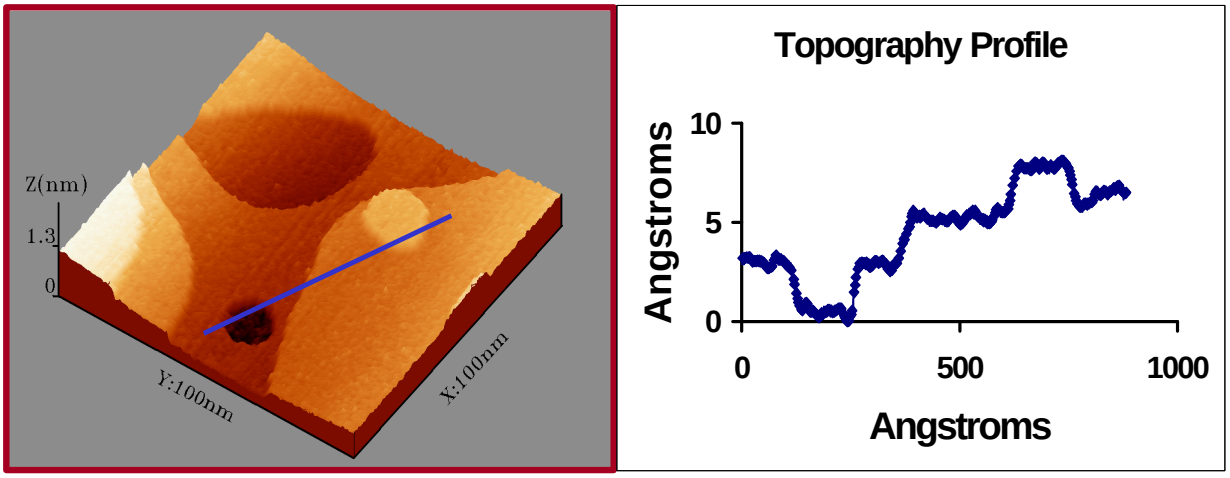

Figure 4.5

Image of Au(111) substrate taken in a UHV STM and a topography profile taken from the image as shown by the blue line.

To ensure the cleanliness of the substrates, they are always handled with clean tweezers and transported in a nitrogen-purged vacuum desiccator pumped to mili-torr pressures. Substrates are

always flamed less than hour before use and are rinsed with distilled ethanol immediately before immersion into the desired molecular solution.

4.5 Sample Characterization

Prior to performing STM experiments, samples must be synthesized and characterized. Sample creation for each molecule studied will be described in an appropriate chapter to follow. Characterization techniques are similar across samples and a basic understanding of the information they provide is needed to understand the procedures required for STS. The characterization measurements include:

- Ellipsometry measurements[64] provide the average film thickness of an organic film on the Au substrate.
- RAIR Spectroscopy[60,64] provides the average orientation of the organic molecules in a film on the Au substrate.
- Electrochemistry[64] provides information on pinhole defects in the organic film layer.
- Water Contact Angle[60] provides a comparative measure to indicate changes in film layers and provides a qualitative measure of SAM quality.
- AFM Topography images[65] provide independent verification of the presence of an organic film on the Au substrate.
- AFM Surface Potential measurements[65] provide information about the average surface dipole moment induced on the substrate surface by the presence of the organic molecule.

Information gathered using ellipsometry and RAIR combined is sufficient to determine the thickness and orientation of an organic film on an Au substrate. Using the known structure of the molecule, monolayer thickness for various orientations can be calculated. The RAIRs data determines the orientation of the molecular film. Thus, from these two pieces of information, the presence of a SAM, on average over the samples surface, can be deduced. Electrochemistry and water contact angle provide further information about film quality.

Finally, AFM topography provides qualitative information on the organic film, such as roughness and identifying pinholes. The AFM surface potential measurements determine the dipole moment of

the SAM layer. From the known structure of the molecule, the expected dipole moment for the molecule can be calculated and checked for consistency with RAIR data.

Taken in total, the characterization methods described above verify the presence of a SAM , on average, over the surface of the Au substrate. Furthermore, other studies[5,8-10,13,61,63,66-68] have shown that sulfide and thiol terminated organic molecules form SAMs on the flat Au(111) crystal surfaces. These same studies show that ordering is best in the center of the grains, fare from edge effects and defects.

4.6 Taking Data

The first five sections of this chapter describe the basics types of data obtained using an STM and the methods used to characterize samples. Equally important is the procedures followed to obtain a data set on a particular sample. It is necessary to first establish that the I(V) data is taken on a region of the substrate covered by a SAM. This is accomplished by taking a "large-scale" topography image (1.0 X 1.0 μm) of the sample and locating a flat Au grain (Figure 4.6). A "small-scale" topography image (100 X 100 nm) of the center of the grain surface is taken (Figure 4.7) and atomically flat terraces are located. I(V) data is then taken at the center of one of these terraces. This is repeated for several spots per sample and for several samples. The result is that if the I(V) data is consistent across spots and samples, and the afore described characterization indicates the presence (on average) of a SAM, then we are confident that the I(V) data is taken on a SAM of the molecule.

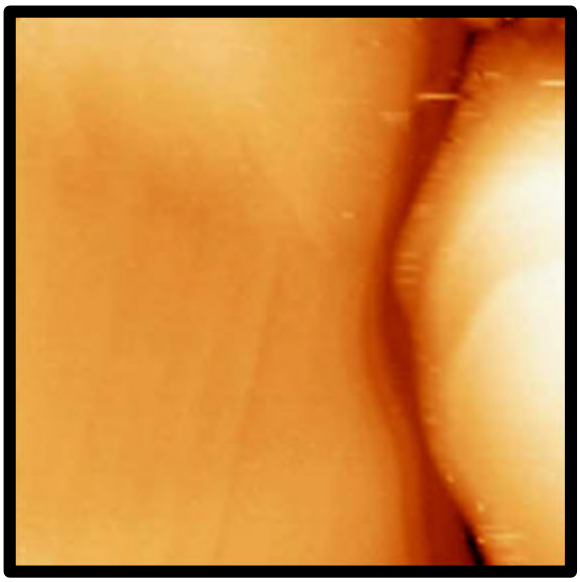

Figure 4.6

1.0 X 1.0 μm topography image of a TMXYL coated Au (111) grain.

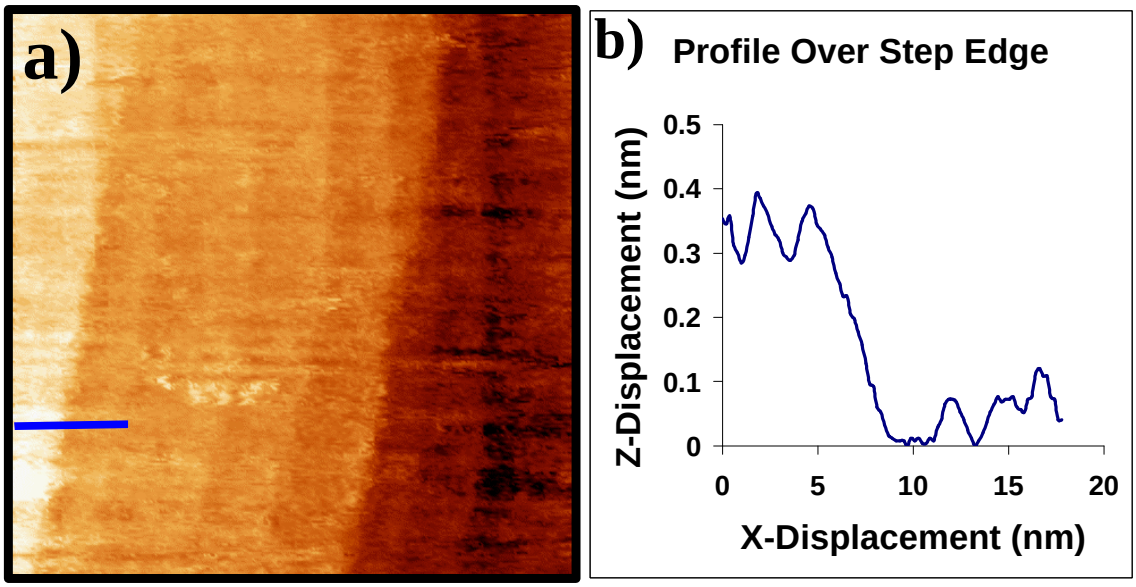

Figure 4.7

a) 100 X 100 nm topography image of a TMXYL coated Au (111) grain. **b)** Corresponding line trace from the topography image (blue line) is consistent with an atomic step edge of Au (111).

The tunnel current is a function of both applied bias and tip-sample separation (see equations 3.2 to 3.4). Increased V_{bias} results in increased tunnel current for a fixed tip-substrate separation, $D_{t\text{-}s}$. Consequently, the tip-substrate separation is a function of V_{set}, and I_{set} (see Table 4.2). This distance is critical since it determines if the tip is buried into the SAM. Initially, when the topography images are taken, a high V_{set} and low I_{set} are used to ensure that the tip is not buried. I(V) data is then taken for a series of V_{set} and a fixed value of I_{set}; the magnitude of V_{set} is decreased in fixed increments. Typical values of I_{set} are 0.2nA and 1.0nA and of V_{set} are 0.5V to 5.0V in 0.5V increments. The results are data sets as shown in Figure 4.8. Next to the I(V) plot is a corresponding "asymmetry" plot where the functional form is:

$$A_N = 2 * \{ I(+V) + I(-V) \} / | I(+V) \;\; I(-V) | \qquad 4.1$$

Equation 4.1 takes into account that generally I(+V) is a positive number and I(-V) is a negative number. The asymmetry number, A_N, is a useful relative measure of the asymmetry present in an I(V) and will be used in later chapters to compare and explain results. Based on equation 4.1, when A_N = 1, then the difference between I(+V) and I(-V) is equal to the average value of the tunnel current at that value of the voltage.

Table 4.2

Response table shows the relative change in tip-sample separation, $D_{t\text{-}s}$, in response to a change in V_{set} or I_{set}. For example, on the first line this table indicates that $D_{t\text{-}s}$ will decrease if V_{set} is fixed and I_{set} is increased. Functional dependence is given in equations 3.2 to 3.4.

$D_{t\text{-}s}$	**V_{set}**	**I_{set}**
Decrease	Fixed	Increase
Increase	Fixed	Decrease
Increase	Increase	Fixed
Decrease	Decrease	Fixed

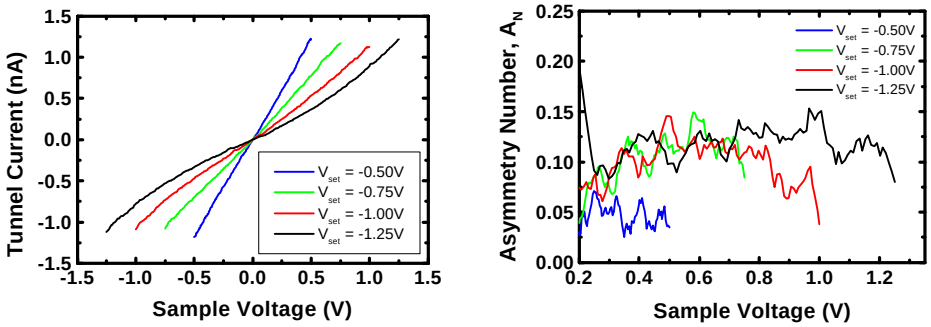

Figure 4.8

Left, I(V) data for Au (111) The plot shows the range of set conditions used to collect the data, in this case, I_{set} = 1.0nA and V_{set} was varied from -0.50V to -1.25V in 0.25 increments. **Right**, Corresponding plot of the asymmetry number, A_N, which shows the difference between I(+V) and I(–V). A_N is only valid for voltages where the tunnel current is above the noise level of the instrument ~ 5pA.

4.7 Asymmetry and η.

In the Introduction it was stated that a new method for taking systematic I(V) data on molecular monolayers was developed and implemented. The method consisted of taking I(V) data on a molecule for a series of V_{set} values and a fixed value of I_{set}. These results are shown in Chapters 6, 7 and 8 and are summarized below in Figure 4.9. On almost every organic molecule studied in this fashion, the I(V) are nearly or relatively more symmetric at a characteristic value of V_{set} (i.e. "critical V_{set}") and become more asymmetric for higher values of V_{set}. For low values of V_{set} (i.e. V_{set} < "critical V_{set}"), the tip is believed to be buried in the SAM. This was determined by monitoring the AC noise on the Z-piezo voltage. Under normal operation (i.e. the tip not in contact with the sample) with the feedback on and the scan size set to zero, the AC noise on the Z-piezo is minimal as shown in Figure 4.11(a). However, if the tip should come into contact with the SAM surface, the noise on the Z-piezo increases significantly as shown in Figure 4.11(b). The transition in the I(V) and the change in the AC noise on the Z-piezo occur near the same value of V_{set} to within ± 0.25V. Consequently, "critical V_{set}" is defined as the value of V_{set} below which the feedback becomes unstable due to contact with the SAM.

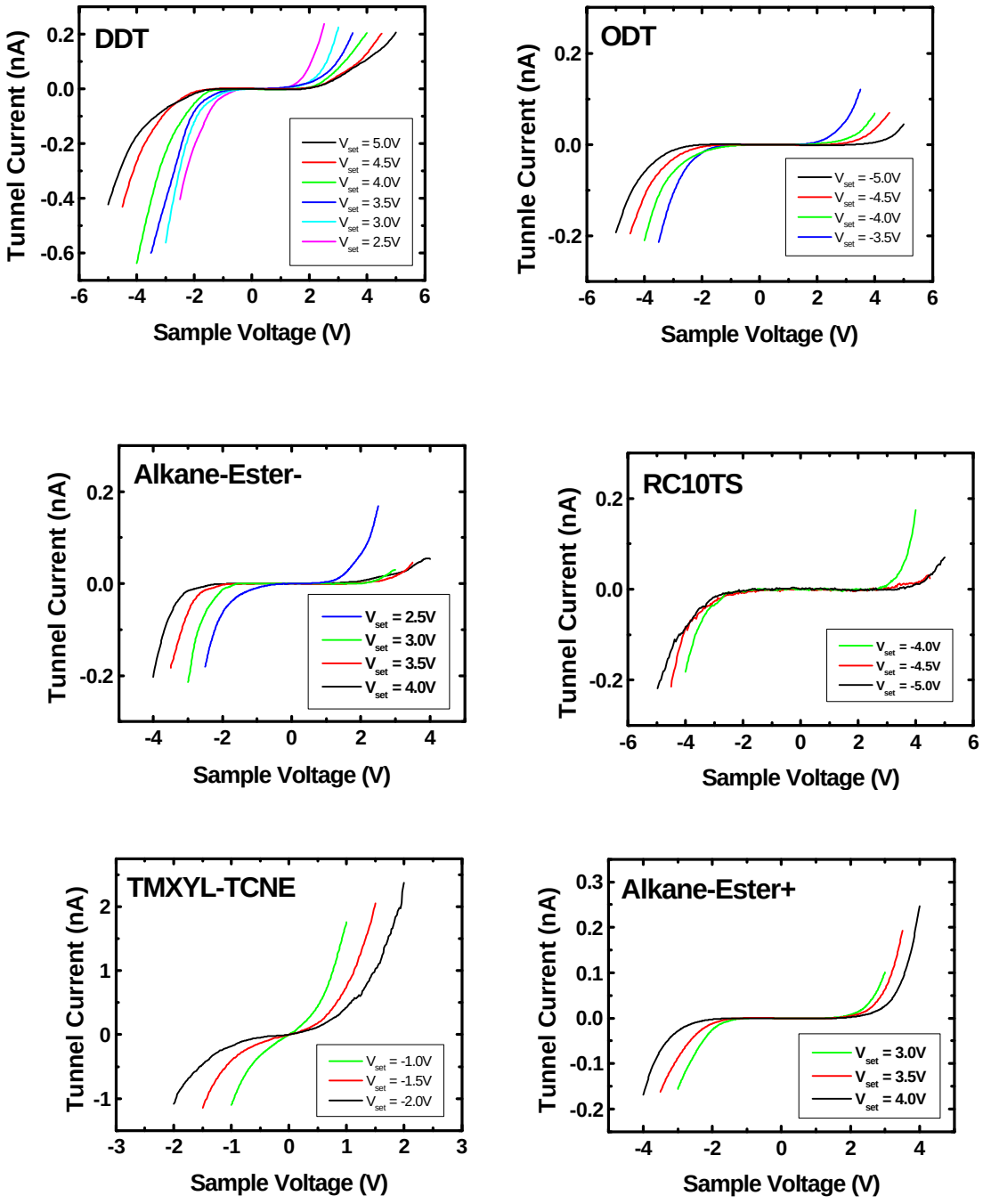

Figure 4.9

I(V) taken on several of the molecules studied herein. All the molecules shown exhibit an increasing amount of asymmetry as the value of V_{set} is increased. This is understood as a lowing of the voltage division factor, η. A decrease in current flow for positive biases (DDT, ODT, Alkane-Ester- and RC10TS) indicates poor coupling to the LUMO level or that the LUMO level is sufficiently removed from the Fermi energy. An increase in current flow for positive bias (TMXYL-TCNE and Alkane-Ester+) indicates that the LUMO levels are being probed.

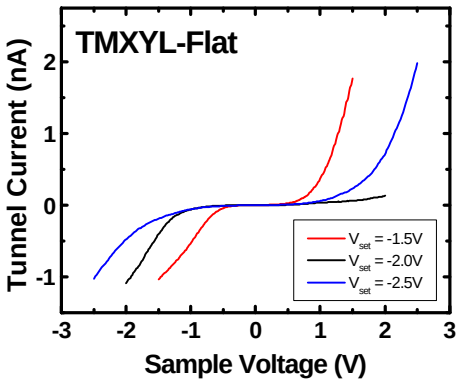

Figure 4.10

TMXYL-Flat appears to be the one exception to the behavior exhibited by the other molecules (see Figure 4.9). Due to its flat orientation to the Au surface, TMXYL-Flat is difficult to interpret based on the theoretical framework presented.

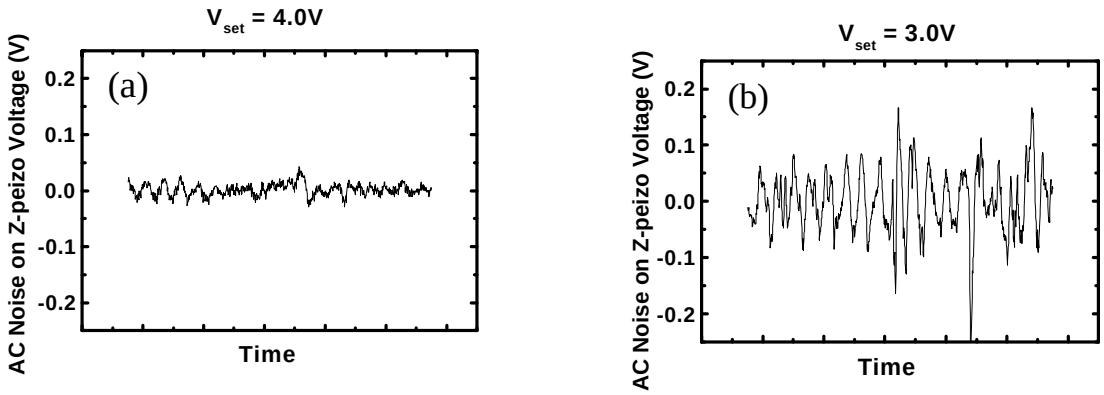

Figure 4.11

The AC noise on the Z-piezo voltage for different values of V_{set} while probing resorcinarene. **(a)** V_{set} = 4.0V corresponds to the "critical" voltage for resorcinarene. **(b)** V_{set} = 3.0V is well below the "critical" voltage and the tip is believed to be buried in the SAM. The result is a significant increase in the noise level.

Based on these observations, the change in the general shape of the I(V) from asymmetric to more symmetric as V_{set} is lowered to its "critical" value is believed to result from a change in the electrostatic coupling between the tip and molecule. In terms of published theories (see Chapter 3 and

references 1, 34, 36 and 38) this may be interpreted as a change in the voltage division factor, η. Numerous factors control the value of η, including:

- asymmetric contacts
- asymmetric coupling to the contacts (even if the contacts are the same)
- charging effects within the molecule
- internal dipoles
- localization of molecular states

In these experiments, the implication is that η 0.5 when the tip is very close (~ 1 or 2 Å) to the top of the molecule and the value of η decreases as the tip is withdrawn from the molecule (by increasing V_{set}).

Since thiols and sulfides are known to transfer charge to the Au substrate, the equilibrium Fermi energy is closer to the HOMO then the LUMO. Also, HOMO levels are generally more delocalized and consequently exhibit greater electron transmission in tunneling experiments. For values of η 0.5 conduction is therefore dominated by the HOMO levels.

The consequences of lowering η, even by a small amount are: i) for negative values of V_{bias}, the HOMO levels are more deeply probed, ii) for positive values of V_{bias} the LUMO levels are more deeply probed (see Figure 4.12). Consequently, a decrease in current flow for positive biases (DDT, ODT, Alkane-Ester- and RC10TS) indicates poor coupling to the LUMO level or that the LUMO level is sufficiently removed from the Fermi energy. An increase in current flow for positive bias (TMXYL-TCNE and Alkane-Ester+) indicates that the LUMO levels are being probed and contribute significantly to conduction.

The change from asymmetric to "more symmetric" (i.e. the value of A_N lowers) occurs gradually for DDT and ODT. This same change is abrupt for Alkane-Ester- and RC10TS. The implication is that the HOMO state is extended into the gap region for DDT and ODT. For Alkane-Ester- and RC10TS the HOMO level appears to end more abruptly as the energy gap region is entered.

This work demonstrates that through the systematic probing of a molecule for different set conditions (V_{set} and I_{set}), I(V) that are reasonably symmetric can always be obtained. The results of this new method can be explained by published theories[1,34,36,38] and can be interpreted as a change in the voltage division factor η. The behavior of the I(V) as V_{set} is increased provides useful information regarding the HOMO and LUMO levels of the molecule under study.

$$I = \frac{2e}{h}\int_{-\infty}^{+\infty} dE \;\; T(E,V) \;\; [f(E-\mu_{Tip}) - f(E-\mu_{Sub})]$$

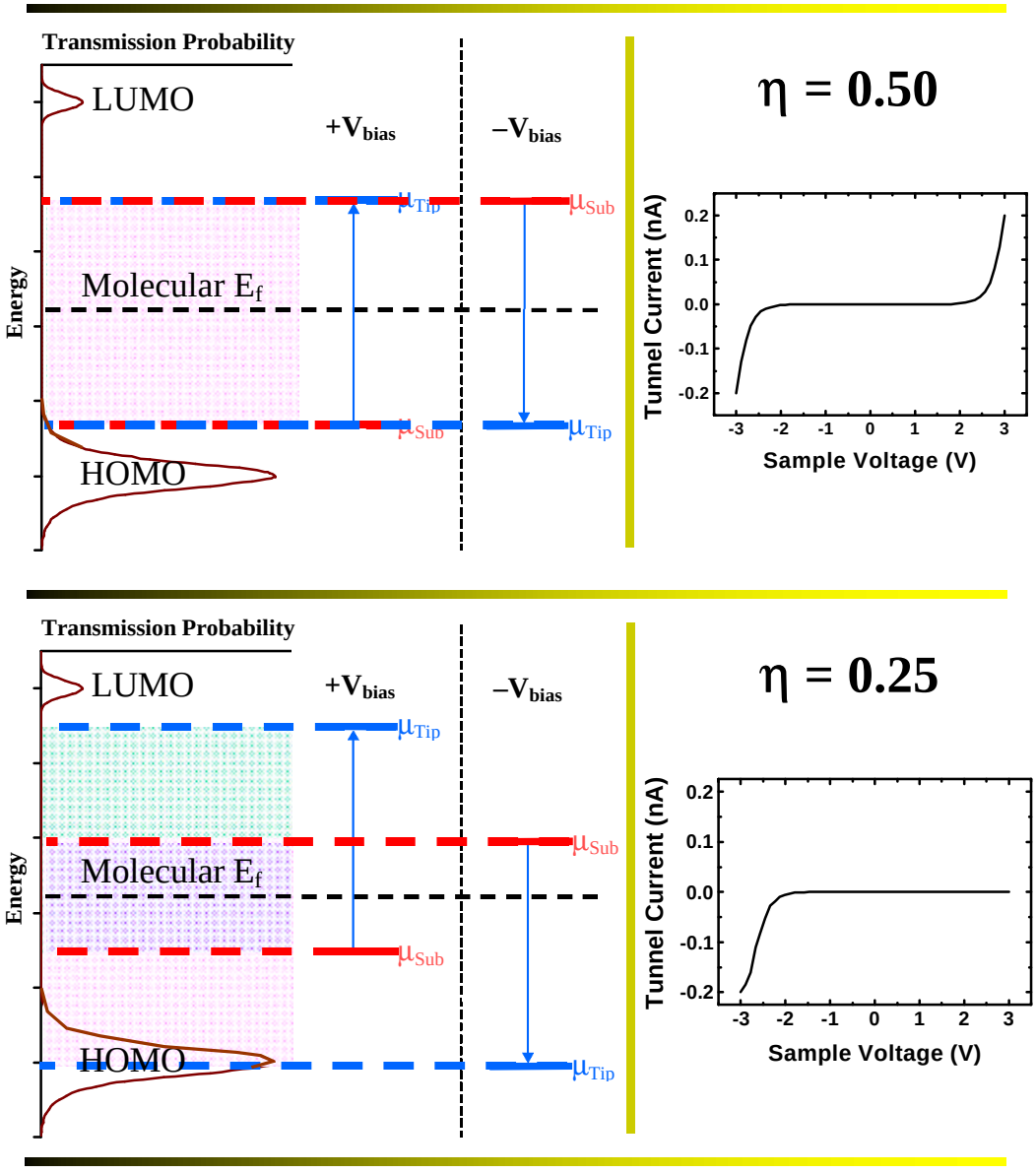

Figure 4.12

The effect of the voltage division factor on the I(V) becomes apparent when you examine its effects on the limits associated with the Landauer-Buttiker formulism (equation 3.8 shown at the top of this figure). For η = 0.5, the I(V) are symmetric because the exact same regions of the transmission function (i.e. the same energy states) are probed for both positive and negative bias voltages. As the value of the voltage division factor drops, the energies regimes probed for positive and negative bias voltages become different leading to an asymmetric I(V).

5. SIMULATIONS

5.1 Introduction

Before we can understand and interpret I(V) data collected using STS, the basic behavior of the STM instrument must be understood. This requires a solid understanding of the simple tunnel barrier on a theoretical and practical level. Presented in this chapter, one-dimensional quantum mechanics is used to numerically model the tunneling barrier between a Au substrate and a Pt tip. Theoretical results are compared experimental results and match to within 5%. In Chapter 9, this model will be expanded to explain certain aspects of STM behavior on molecules.

5.2 Calculating T(E,V)

First, let us consider a simple tunnel junction as depicted in Figure 5.1; for simplicity, the contacts are treated as regions of a free electron gas with a constant value of potential (i.e. Region I and Region III in Figure 5.1) and the barrier region has a potential given by:

$$j_0(z) = \left(\frac{j_t - j_s + V_{bias}}{a} \right) z + (j_s + E_{f,s}) \qquad 5.1$$

Based on the assumption that the tip apex atom dominates the tunnel current, we can, to a good approximation, treat this junction as a one-dimensional tunneling problem. Consequently, we can use equation 3.8 to evaluate the current flowing through the tunnel junction. What remains, is to find an expression for the transmission function, T(E,V). Others[42-44,53,54] have used the Wentzel-Kramers-Brillouin (WKB)[46] approximation to evaluate T(E,V).

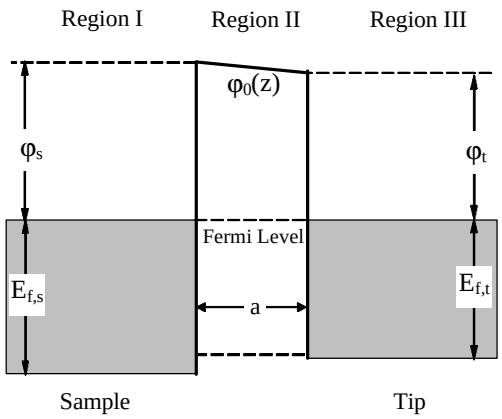

Figure 5.1

Simple schematic of a tunneling barrier resulting from two metals brought within close proximity (~0.3nm to 2.0nm) to each other.

The WKB approach is a method of obtaining approximate solutions to the one-dimensional, time-independent Schrödinger equation. The WKB method is of particular utility in calculating transmission probabilities through tunnel barriers:[46]

$$T(E) = e^{-\frac{2}{\hbar}\int_0^a dz\sqrt{2m[j(z)-E]}} \qquad 5.2$$

where φ(z) is the barrier potential between the region 0 z a and E is the energy of the electron. However, the WKB approximation is known to generate significant error in the transmission probability, especially if the barrier boundary is abrupt.

Figure 5.2 depicts a square tunnel barrier; the square barrier has an exact solution for the transmission probability:[45]

$$T(E) = \frac{(2ka)^2}{(k^2 + a^2)^2 \sinh^2 2a\, a + (2ka)^2} \qquad 5.3$$

where

$$k^2 = \frac{2mE}{\hbar^2} \qquad 5.4$$

and

$$a^2 = \frac{2m(j_0 - E)}{\hbar^2} \qquad 5.5$$

Figure 5.3 shows the results of the WKB approximation of T(E) compared to the exact solution of T(E) for a square barrier. The result is that the WKB approximation gives good order-of-magnitude results for T(E,V) but lacks the accuracy required for accurate modeling. Additionally, the WKB approximation is valid only for tunnel barriers and bound states. Consequently, barriers such as a square well where E > 0 (see Figure 5.6)[46] may not be evaluated using the WKB approximation.

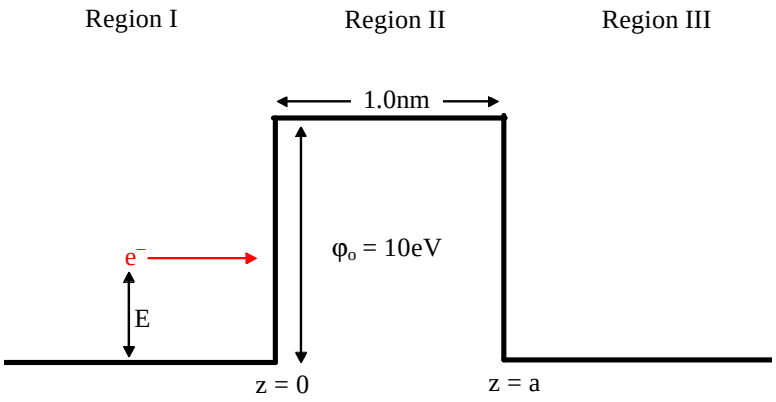

Figure 5.2

Square barrier.

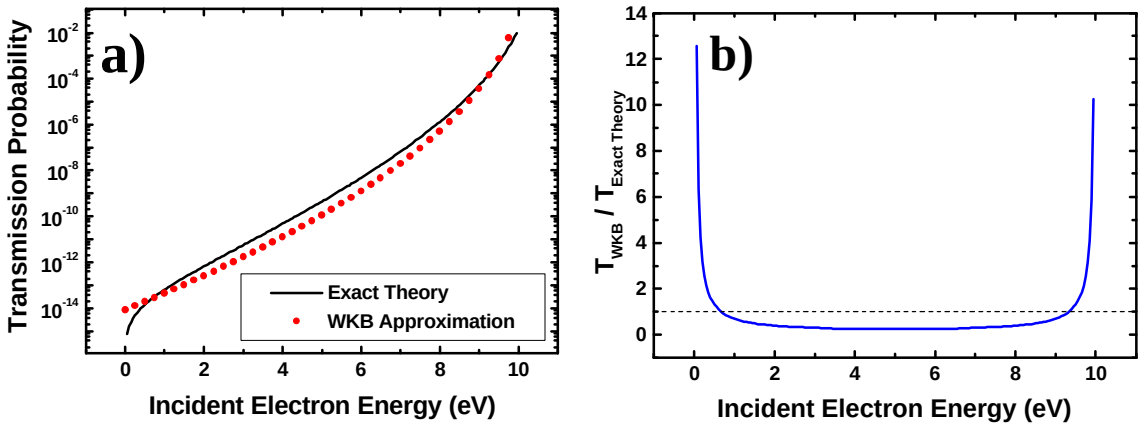

Figure 5.3

a) T(E) for a 10eV high and 1nm wide tunnel barrier as calculated using the exact theory and the WKB approximation. **b)** T_{WKB} / T_{exact} shows the relative error in the WKB approximation when applied to a square barrier.

Lambin & Vigneron[69-71] developed a simple numerical method based on a discretised Schrödinger's equation,

$$\frac{y(z+h) - 2y(z) + y(z-h)}{h^2} = [j(z) - e]y(z) \qquad 5.6$$

for evaluating the transmission probability through a one-dimensional tunnel barrier (henceforth referred to as the L&V method). In equation 5.6 φ(z) is the total barrier potential and ψ(z) is the wave function. The value, h, is proportional to the truncation error and is given by:

$$h = (z_{n+1} - z_0) / (n + 1) \qquad 5.7$$

where the index, n, represents counts the discrete values of z. Obtaining the solution to equation 5.6 is somewhat involved and is shown in detail by Lambin & Vigneron[69-71]. The end result is the transmission coefficient is given by:

$$T = (1 - R) = \left(1 - \left|\frac{R_{-1} - R^-}{R_{-1} - R^+}\right|^2\right) \qquad 5.8$$

where

$$R^{-} = \frac{b_I}{2} - i\left[1 - \left(\frac{b_I}{2}\right)^2\right]^{1/2} \tag{5.9}$$

$$R^{+} = \frac{b_I}{2} + i\left[1 - \left(\frac{b_I}{2}\right)^2\right]^{1/2} \tag{5.10}$$

$$R_{-1} = b_0(E) - \cfrac{1}{b_1(E) - \cfrac{1}{b_2(E) - \ldots}} \tag{5.11}$$

$$\ldots \cfrac{1}{b_n(E) - \cfrac{1}{\cfrac{b_{III}}{2} - i\left[1 - \left(\cfrac{b_{III}}{2}\right)^2\right]^{1/2}}}$$

$$b_i = 2 + h^2[j_i - E] \tag{5.12}$$

$$b_n(E) = 2 + h^2[j(z_n) - E] \tag{5.13}$$

The expression for R_{-1} (equation 5.11) is called a continued fraction and is easily evaluated using a simple computer program (Appendix A). β_i is only defined in Regions I and III (see Figure 5.1); φ_i is the corresponding potential in that region, and the index, i = I, III.

The L&V method has the advantage that its accuracy is related to the number of numerical steps used to model the barrier, thus, any level of accuracy can be obtained by taking enough steps. This is illustrated in Figure 5.4; the L&V method was used to calculate T(E) for a square well using 1000 points to model the barrier. The result is the L&V method matches the exact solutions within 5% for all energies above 0.5eV. For comparison, the results shown in Figure 5.3 and Figure 5.4 are plotted together in Figure 5.5. This figure clearly shows the L&V method offers superior results to the WKB method and has the accuracy required for modeling a general tunneling barrier.

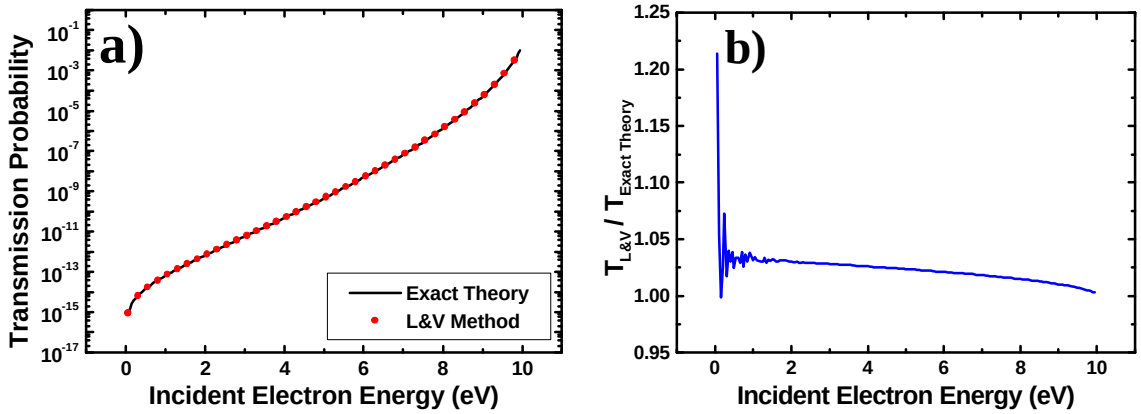

Figure 5.4

a) T(E) for a 10eV high and 1nm wide tunnel barrier as calculated using the exact theory and the Lambin & Vigneron method. **b)** $T_{L\&V}$ / T_{exact} shows the relative error in the Lambin & Vigneron method when applied to a square barrier (1000 points).

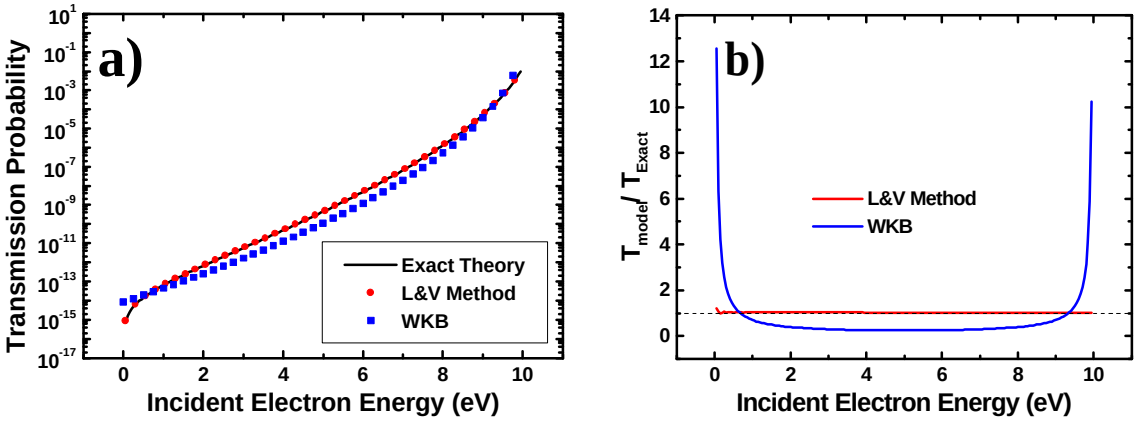

Figure 5.5

a) T(E) for a square barrier as calculated by the Exact Theory, the L&V Method and WKB. **b)** A comparison of $T_{L\&V}$ / T_{exact} to T_{WKB} / T_{exact} shows the greater accuracy of the L&V Method.

Additionally, the L&V method is derived directly from Schrödinger's equation and therefore can be used even if E > φ(z) within the barrier. To illustrate this, the L&V method was applied to a square well as depicted in Figure 5.6 and the results as compared to the exact theory are shown in Figure 5.7. The exact solution for transmission probability above a square well is given by:[46]

$$T^{-1} = 1 + \frac{j_0^2}{4E(E + j_0)} \sin^2\left(\frac{2a}{\hbar}\sqrt{2m(E + j_0)}\right) \qquad 5.14$$

The L&V method matches the exact solutions within 1%.

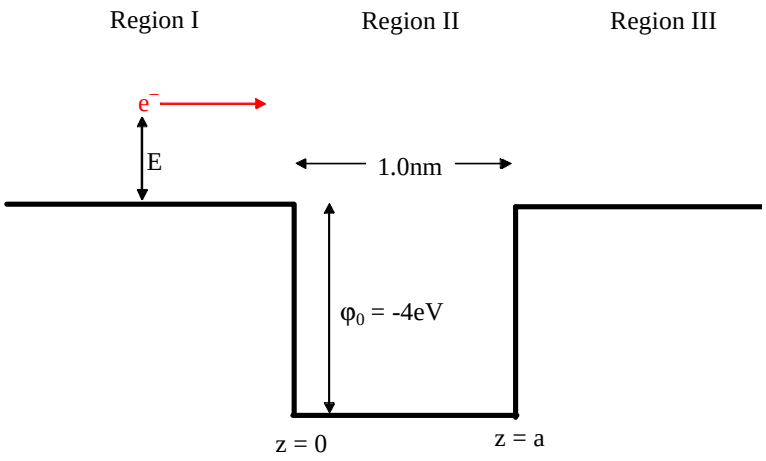

Figure 5.6

Square well barrier.

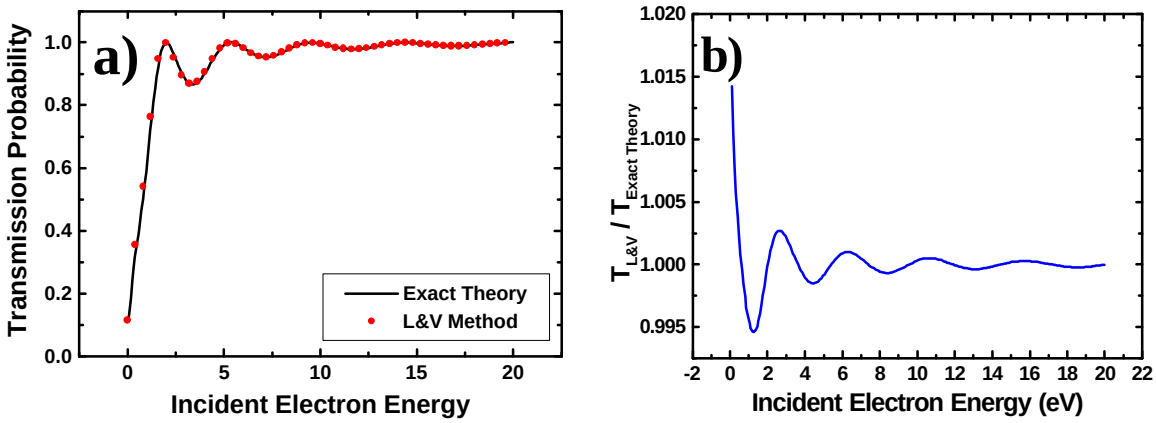

Figure 5.7

a) T(E) for a 4eV deep and 1nm wide square well as calculated using the exact theory and the Lambin & Vigneron method. **b)** $T_{L\&V}$ / T_{exact} shows the relative error in the Lambin & Vigneron method when applied to a square well (1000 points).

5.3 Modeling the STM Tunnel Junction

Equally as important as the method used to calculate T(E,V) is the selection of the model barrier used to model the tunnel junction. The barrier model used can be developed in stages:

1) Simple Barrier based on workfunction values, the Fermi energy and simple geometry.

2) Image charge effects due to the presence of the electron between two conducting surfaces.

3) Electric field enhancement effects to the "sharp" geometry of the tip.

Figure 5.8 shows a schematic of the "simple" tunnel barrier (Region II) between a Au(111) surface (Region I) and Pt(111) surface (Region III). It is assumed that the potential in the contact regions (i.e. Region I and Region III) is a constant value and $E > U_0$.

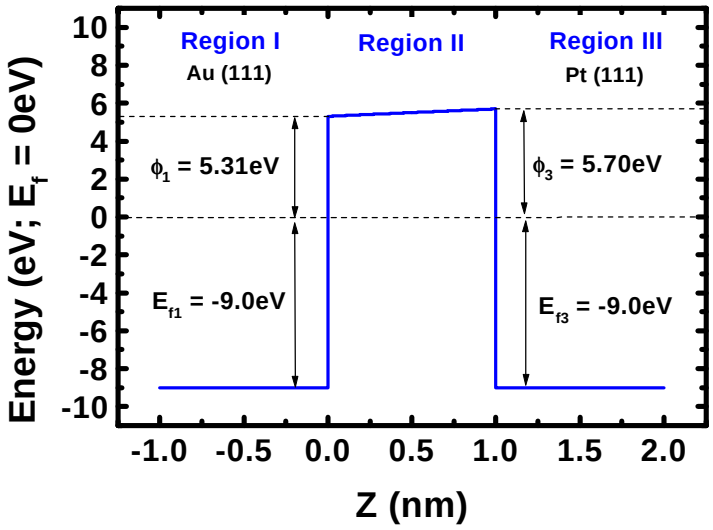

Figure 5.8

Simple model of a one dimensional tunneling barrier between two metal contacts (Au and Pt). The thick blue line represents the barrier as constructed from the bulk properties of the two metal contacts.

A slightly better model of the tunnel junction takes into account that the barrier region will not have the sharp sidewalls present in the original barrier but will have rounded features due to the effects of image charges between the tip and sample. A good first order approximation is to calculate image charge effects by treating the two contacts as infinite conducting planes. The subsequent correction term to the barrier potential is given by[72,73]:

$$\ddot{o}_{ImChg}(z) = -\frac{1.15e^2 \ln(2)}{16\eth\aa_0} \frac{D_{t-s}}{z(D_{t-s} - z)} \qquad 5.15$$

The result is that the total potential in the barrier region is now given by:

$$\ddot{o}_t(z) = \ddot{o}_0(z) + \ddot{o}_{ImChg}(z) \qquad 5.16$$

where ϕ_0 is the original barrier potential. The effect of equation 5.15 is to lower the effective workfunction of the system and round the sharp corners of the barrier. These changes in turn, increase the values of T(E,V). Examining equation 5.15 we see that ϕ_{ImChg} - as z 0 or z d. This of course, is unphysical, so the model is corrected by not allowing ϕ_I to drop below the bottom of the

conduction band of the nearest contact. The end result is a barrier as depicted by the purple line in Figure 5.9.

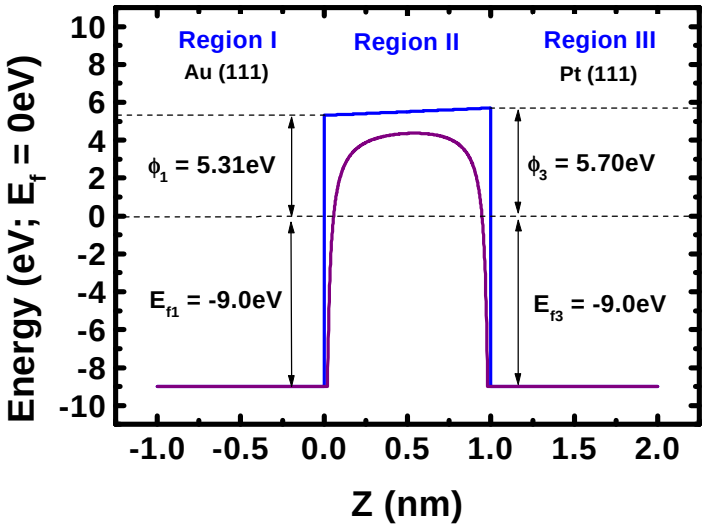

Figure 5.9

The purple line represents the one-dimensional barrier once image charge effects are included in the model. The inclusion of image charge effects lowers the effective barrier height and rounds the sharp edges of the barrier. The work function values were taken from the CRC Handbook of Chemistry and Physics, 74th Ed. 1993.[75]

In this simple model, the applied bias serves to raise ($-V_{bias}$) or lower ($+V_{bias}$) the energy band of the ungrounded contact. By convention[1-4,42] the tip is ground; consequently, electric potential is measured as applied to the sample. Using this model I(V) data can be generated using a computer program (Appendix A). To match experiment, V_{set}, I_{set}, and the work functions of the two contacts are control parameters and the barrier width, d, is adjusted automatically via a feedback loop. A flowchart of the program used is provided in Figure 5.10 and the results of the simulation are shown in Figure 5.11. The 0.6eV workfunction difference between Au and Pt results in a "small" asymmetry between negative and positive values of the voltage bias.

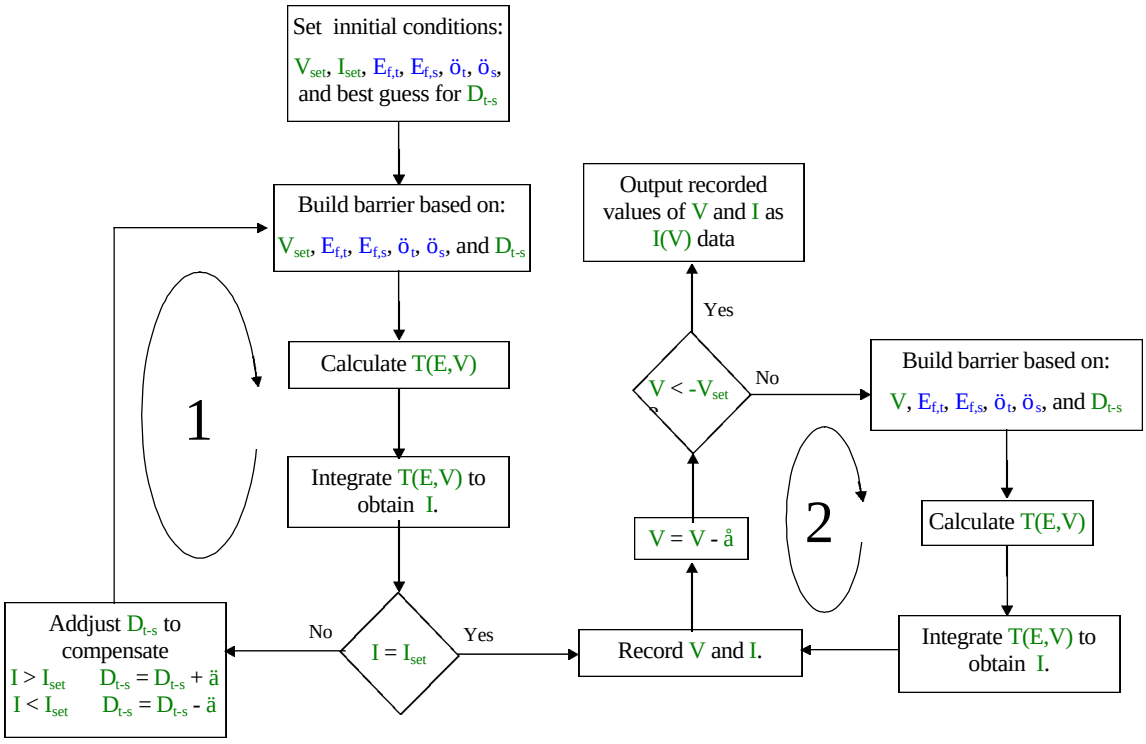

Figure 5.10

Flowchart of the tunnel barrier simulation program used to model a simple tunnel junction. Loop 1 acts like the feedback which sets the barrier width based on the given values of V_{set} and I_{set}. Loop 2 steps the voltage values and generates a corresponding current value; these values are combined to generate an I(V).

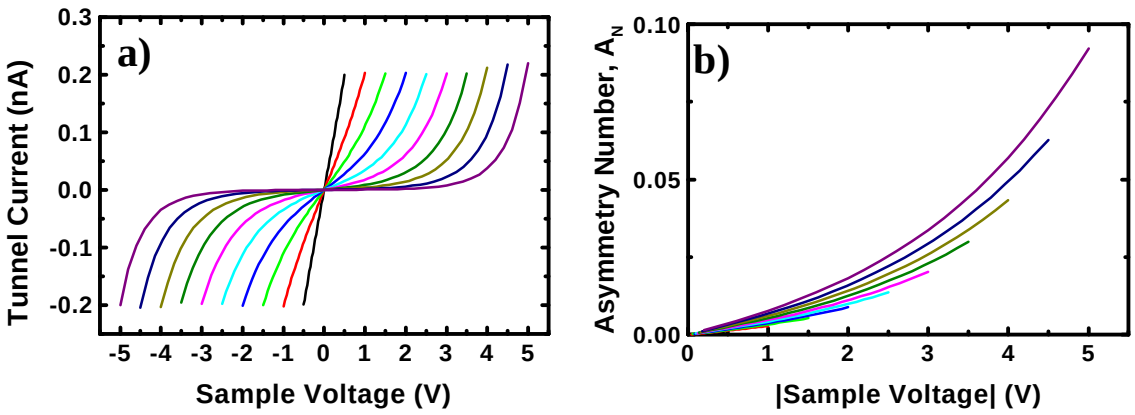

Figure 5.11

a) I(V) data generated using a program based on the model described in this section (i.e. the image charge modified barrier in Figure 5.9); I_{set} = 0.2nA and V_{set} = -0.5V to -5.0V in 0.5V increments. **b)** The slight asymmetry observed between positive and negative bias voltage is a result of the workfunction difference between Au and Pt.

However, due to the fact that the tip is sharp, there is an enhancement of the electric field strength near the tip when a voltage bias is applied across the tunnel barrier. Approximating the tip by a hyperbola[2,74] the effects of having a sharp probe tip on the electric field can be evaluated along the Z-axis of the tunnel junction. Consequently, $V_{bias}(z)$ across the junction can be derived[74]:

$$V_{bias}(z) = \frac{V_0}{\ln\left[\frac{1+h_e}{1-h_e}\right]} \ln\left[\frac{1-\frac{h_e z}{D_{t-s}}}{1+\frac{h_e z}{D_{t-s}}}\right] \qquad 5.17$$

η_e (not to be confused with the voltage division factor η) is given by:

$$h_e = \left(1+\frac{R}{D_{t-s}}\right)^{-\frac{1}{2}} \qquad 5.18$$

where, R = Tip Radius. The subsequent effects on the tunnel barrier for $\pm V_{bias}$ are plotted in Figure 5.12. Negative applied biases tend to increase the average barrier height; the electron is accelerated

from a region of relatively weak electric field. Positive applied biases tend to decrease the average barrier height; the electron is accelerated from a region of relatively strong electric field. The effect on the I(V) data is an increase in asymmetry as a function V_{set}; the results are depicted in Figure 5.13.

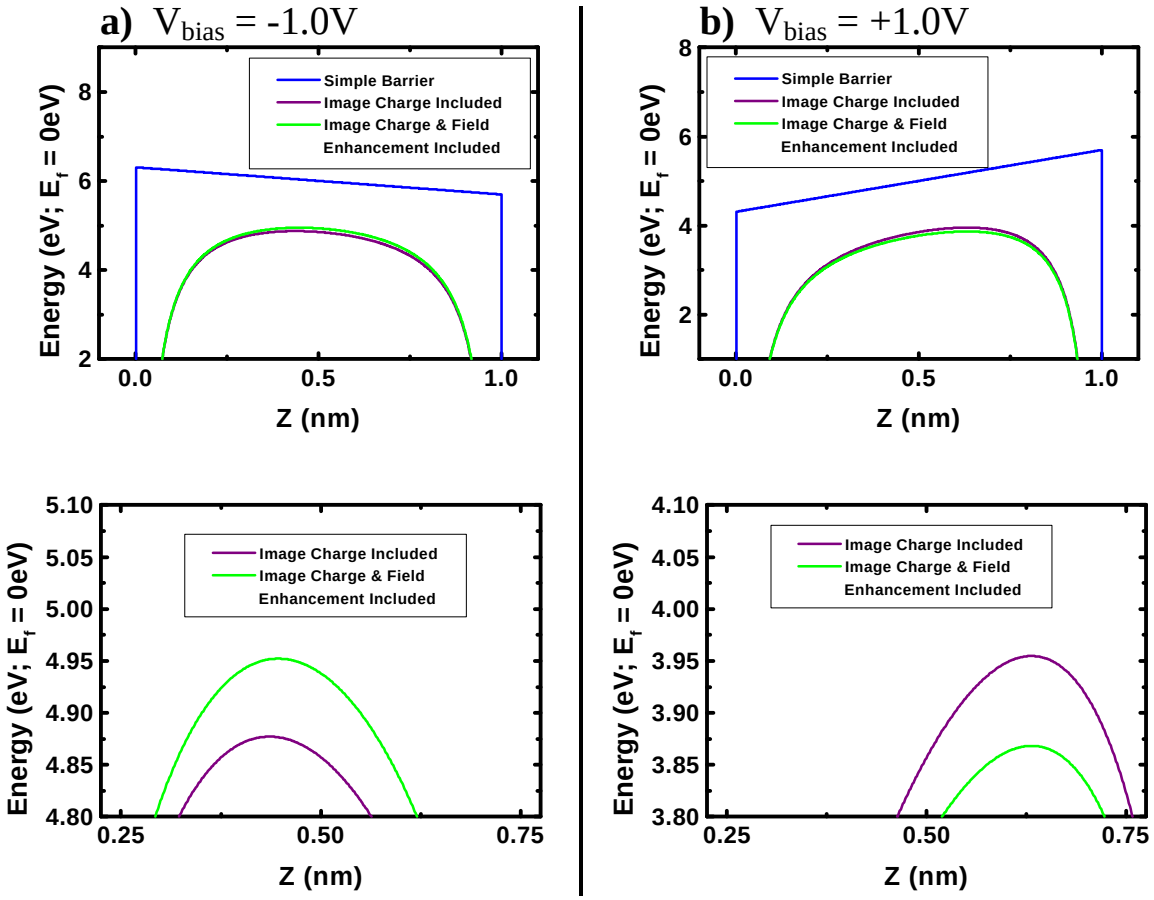

Figure 5.12

The above plots were generated using the barrier depicted in Figure 5.9; a 1.0nm tip radius was used. **a)** When the tunnel junction is biased with a negative voltage (sample relative to tip), the field enhancement due to the tip tends to increase the height of the tunnel barrier (green line). **b)** When the tunnel junction is biased with a positive voltage, the field enhancement due to the tip tends to decrease the height of the tunnel barrier (green line).

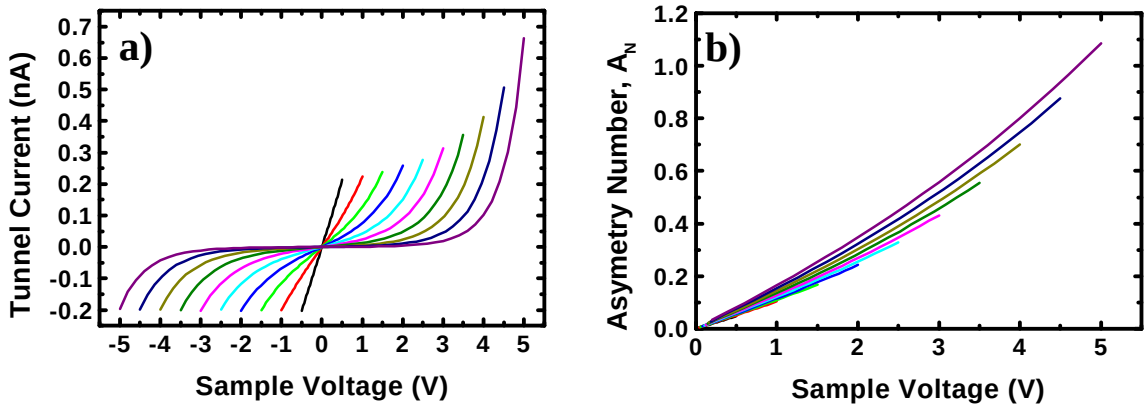

Figure 5.13

a) I(V) data generated using the simulation program on the barrier shown in Figure 5.12; I_{set} = 0.2nA and V_{set} = -0.5V to -5.0V in 0.5V increments. In this case, electric field enhancement effects due to the sharpness of the STM tip are included. **b)** The result is a significant increase in the asymmetry observed, especially for larger values of V_{set}. For this simulation, negative values of V_{set} were used in 0.5V increments.

5.4 I(V) on Au (111)

Using the model and program discussed in the previous section, I(V) data can be generated and compared to experimental results. Figure 5.14 shows I(V) data taken on bare Au(111) and the corresponding theoretical calculations made with the afore mention program. To accurately model the data, the barrier was constructed using the accepted values of the work functions for Au(111) and Pt(111)[75]. The barrier width was calculated self-consistently using a feedback loop and the set conditions (V_{set}, I_{set}) used in the actual experiment. The only unknown parameter was the tip radius, which was initially guessed to be ~1.0nm; the best fit to the data used a tip radius of 2.25nm. The theoretical fits match the general shape of the I(V) as well as the actual values; all of which match to within 5% of the experimentally measured value. Our one-dimensional model works well because it captures the essential elements of the metal-to-metal STM tunnel barrier. In particular, the implications of equation 3.2 allows the greatly simplifying one-dimensional approximation.

Referring back to Figure 4.11, which depicts the asymmetry plots for the I(V) data shown in Figure 5.14, we see that there is a slight asymmetry in the I(V) for Au. Without the inclusions of the

field enhancement due to the sharp tip, the simulation would have failed to match the data correctly; this is shown in Figure 5.15.

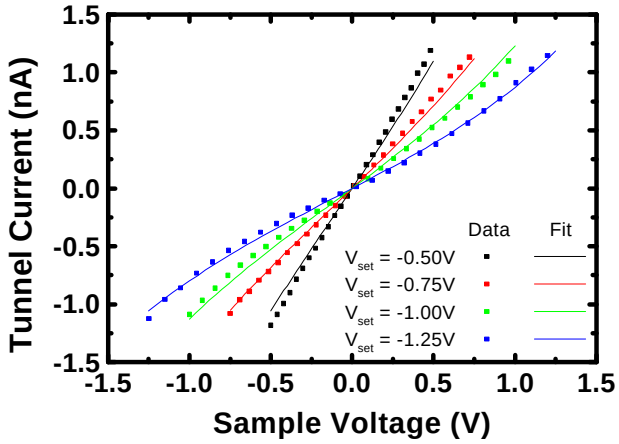

Figure 5.14

I(V) data on Au(111) and corresponding theoretical fits calculated using the model described above (see appendix A for program). The fits were generated by using the set conditions (i.e. V_{set} and I_{set}) used when collecting the I(V) data and the accepted values for the work functions of Au(111) and Pt(111).[75] The only "fitting parameter" was the tip radius which was assumed to be ~2.25nm.

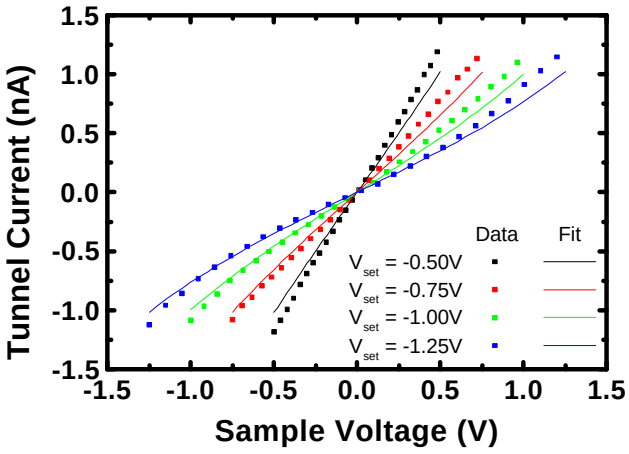

Figure 5.15

I(V) data on Au(111) and corresponding theoretical fits without the inclusion of field enhancement due to the relative sharpness of the STM tip. The result of not using the field enhancement is a poor fit to the data for positive voltages.

5.5 I(Z) on Au (111)

Now that we have a theoretical model that may be used to numerically model STM behavior in a metal-to-metal tunnel junction, the next logical step is to use the model to check or predict other STM behavior. I(Z) is the current response of the STM as a function of tip position. Such data is generated by moving the STM tip through a fixed distance (while at a fixed voltage) and recording the current output. Based on equation 3.2,

$$I \propto e^{-2\kappa Z} \tag{5.19}$$

we expect I(Z) to behave in an negative exponential fashion; consequently, ln[I(Z)] should result in a straight line.

Due to the method used to control an STM, only relative distances may be measured (see Chapter 2); absolute distances can be calculated through the use of equation 3.8 but are experimentally difficult to verify. Consequently, the only direct check between experiment and our theoretical model is the verification of the magnitude of the exponent in equation 5.19; this is most easily done from a natural log plot. However, it is more intuitive to check the "average" workfunction of the tunnel barrier as given by equation 3.3:

$$\varphi = \frac{1}{2m}[\kappa h / 2\pi]^2 \tag{5.20}$$

which may be rewritten in terms of the slope measured on a Ln plot:

$$\varphi = \frac{1}{2m}[\text{slope} * h / 4\pi]^2 \tag{5.21}$$

Additionally, equation 3.4 (restated here),

$$\varphi_{th} = (\varphi_s - e|V_{bias}| + \varphi_t)/2 \tag{5.22}$$

gives the theoretical value of φ_{ave} based solely on the measured workfunctions and not taking into account the image charge effect which tends to reduce the effective workfunction of the system.

Seunghun Hong performed a series of I(Z) data on various samples including Au (111); the results were published[12] and are shown below in Figure 5.16 (a). Figure 5.16 (b) shows a theoretical

calculation of I(Z) using the model described above. From equation 5.20 we find that φ_{exp} = 2.1eV and φ_{sim} = 4.5eV and φ_{th} = 5.0eV. As is clear from the values of φ_{sim} and φ_{th} some reduction of effective workfunction is expected due to image charge effects and our model is in good agreement with theory but not the experiment by Hong. "Low" measured values of φ as measured by STM I(Z) have been reported[76-81] and have subsequently resulted in significant controversy. Anomalously low STM I(z) measurements of φ have been explained in terms of sample surface contamination[82] and instrumentation issues.[83] Olesen et.al.[83] contends that high input impedance associated with the current preamplifier results in low measurements of φ especially for small tip-sample separations. On Au (110) Olesen et.al. was able to correct for the inaccuracies resulting from preamplifier input impedance; the subsequently reported measurement of φ on Au (110) is in excellent agreement with my simulation on Au (110) (see Table 5.1).

Table 5.1 summarizes the results from numerous experiments and the corresponding simulations performed using the afore discussed computer model. In an STM experiment the theoretical workfunction, $ö_{th}$, is an average of the tip and substrate workfunctions and is effected by V_{bias} but not image charge effects (see equation 5.22). The simulation calculated values of the workfunctions, $ö_{sim}$, are on average ~0.8eV lower than $ö_{th}$; this is due to image charge effects. As is evident from Table 5.1, STM measurements of ö are lower than expected due to experimental issues. We conclude that measurements of ö as calculated from STM I(Z) are in reality measurements of the tunnel barrier height; which is related to, but not solely determined by the work function of the sample.

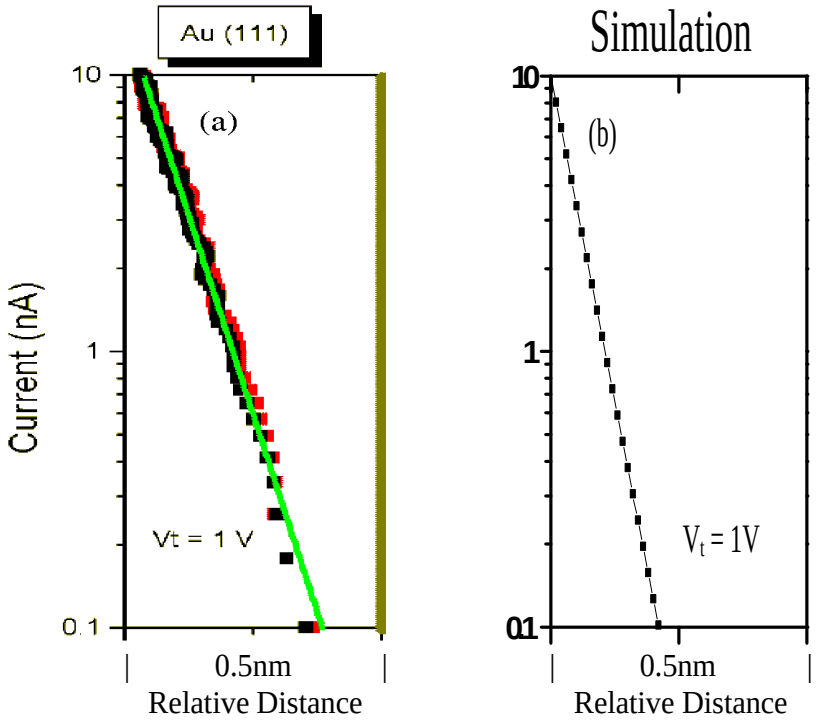

Figure 5.16

Current versus tip-sample separation, I(Z). **(a)** I(Z) data taken by S. Hong[12] on Au (111). **(b)** I(Z) calculated using the simulation program.

Table 5.1

A summary and comparison of workfunction values for various metal surfaces. "Accepted" workfunction values, $\ddot{o}_{acc}$, are based upon a combination of optical measurements and theoretical calculations.[75] "Theoretical" workfunction values, $\ddot{o}_{th}$, are based upon equation 5.22 and do not take into account image charge effects; the tip was assumed to be polycrystalline Pt ($\ddot{o}_{acc}$ = 5.65eV) since cut Pt tips were used in the STM experiments. "Simulated" workfunction values, $\ddot{o}_{sim}$, were numerically calculated using the simulation program described in the text. $\ddot{o}_{sim}$ are ~0.8eV lower than the corresponding $\ddot{o}_{th}$; this is due to image charge effects. "Experimental" values, $\ddot{o}_{exp}$, are based upon STM I(Z) measurements.

Reference	**Sample**	**V_{bias} (V)**	**$\ddot{o}_{acc}$ (eV)**	**$\ddot{o}_{th}$ (eV)**	**$\ddot{o}_{sim}$ (eV)**	**$\ddot{o}_{exp}$ (eV)**
Gimzewski et.al.[76]	Ag (poly)	0.02	4.26	4.95	4.14	1.5-3.5
Wintterlin et.al.[77]	Al (111)	0.05	4.24	4.92	4.13	3.5
Kuk et.al.[78]	Au (100)	0.05	5.47	5.54	4.76	3.5
Berndt et.al.[79]	Au (110)	0.80	5.37	5.11	4.59	4.0
Schuster et.al.[80]	Au (110)	-0.14	5.37	5.44	4.72	2.0
Hong et.al.[12]	Au (111)	1.00	5.31	4.98	4.50	2.1
Olesen et.al.[83]	Ni (100)	0.005	5.22	5.43	4.64	3.7
	Cu (100)	0.005	4.59	5.12	4.31	1.8
	Pt (100)	0.005	~5.65*	5.65	4.86	3.4
	Au (110)	0.005	5.37	5.51	4.72	4.7

$\ddot{o}_{acc}$ = "accepted" value quoted in CRC Handbook of Chem. and Phys. 74th ed. 1993-94.
$\ddot{o}_{th}$ = theoretical value as given by equation 5.22; the tip was assumed to be Pt (poly).
$\ddot{o}_{sim}$ = value calculated using the simulation program in conjunction with equation 5.21.
$\ddot{o}_{exp}$ = experimentally measured value from the given reference.

*$\ddot{o}_{acc}$ for Pt (100) not given, therefore the polycrystalline value was used.

5.6 $Z(V_{set})$ on Au (111)

One of the primary questions always asked by anyone doing STM experiments is: "How far is the tip from the sample?". Using our model, we can answerer that question, the results are shown in Figure 5.17. To generate Figure 5.17 the set voltage was incrementally changed with the feedback turned on for a fixed set current. For V_{set} < 4.0V, $Z(V_{set})$ roughly linear with a slope of ~ 0.5 nm/volt and for V_{set} > 4.0V, $Z(V_{set})$ is again linear with a slope of ~ 1.0 nm/volt. The change in slope of $Z(V_{set})$ at V_{set} = 4.0V is easily explained by examining Figure 5.9. V_{set} = 4.0V corresponds to an

energy of 4eV which is where the barrier sidewall shows a distinct change in its slope; this translates to a significant change in the slope of $Z(V_{set})$. Note that the value of I_{set} acts as a Z-offset and does not alter the functional dependence of Z on V_{set}. This implies that by using voltage instead of current to control the STM, sub-Angstrom control of the tip position relative to the sample may be achieved. Extending this method to molecular samples may allows the tip-molecule separation to be tuned with a high degree of precision. Such an approach could lead to a method of specifying the tip-molecule separation, which subsequently would improve modeling efforts. However, molecular systems have energy states which effect T(E,V) and thus $Z(V_{set})$. Consequently the difficulty that remains is determining the voltage at which the tip comes into contact with the molecule.

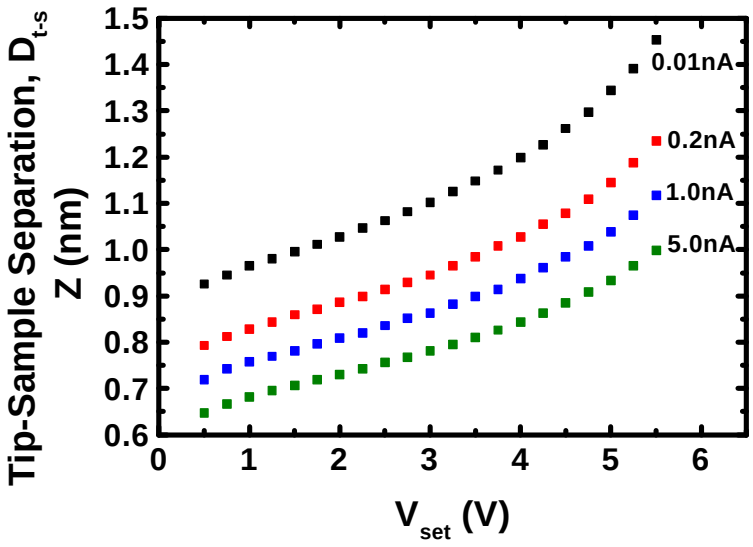

Figure 5.17

$Z(V_{set})$ simulated for Au(111) at different fixed values of I_{set}. The value of I_{set} acts as an offset and does not change the functional dependence of Z on V_{set}.

The simulations of $Z(V_{set})$ combined with actual data provides an estimate for the stability of the experimental apparatus. Figure 5.18(a) shows a series of ten (forward and reverse) I(V) data taken on Au(111) for a set condition of V_{set} = -0.75V and I_{set} = 1.0nA; the average of this data is plotted in

Figure 5.14 and Figure 5.15. Figure 5.18(b) shows the same data but focused in on the set point; almost all the data lies between the two red lines corresponding to 0.95nA and 1.15nA. This -5% +15% spread in I(V_{set}) is typical of any set of I(V) data on any sample. Running the simulation use to generate Figure 5.17, the -5% +15% variation in I(V_{set}) corresponds to a ±0.01nm variation in tip-sample separation. How the asymmetric variation in I(V_{set}) leads to a symmetric variation in tip-sample separation is easily understood by examining equation 3.2; which shows that the tunnel current has an exponential dependence on tip-sample separation.

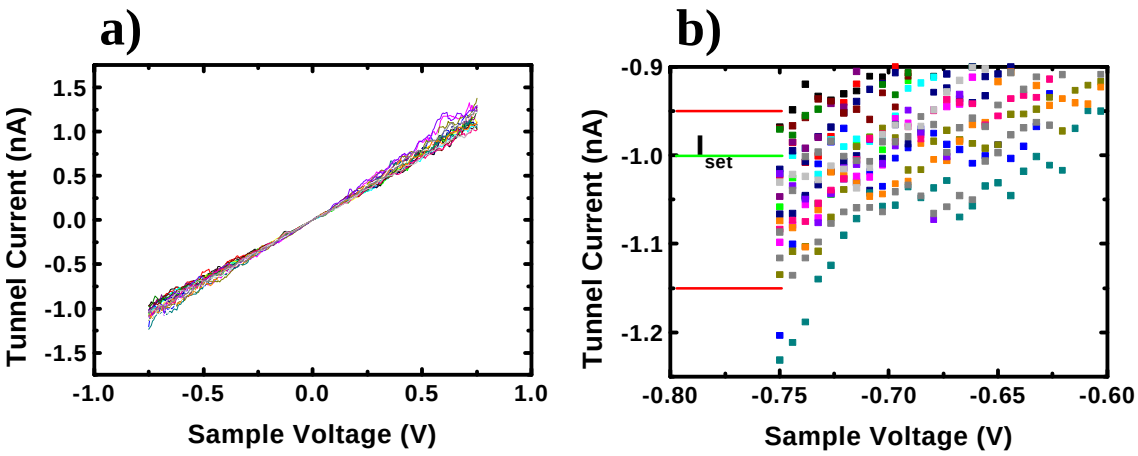

Figure 5.18

a) Ten (forward and reverse) I(V) taken on Au(111) with a set condition of V_{set} = -0.75V and I_{set} = 1.0nA. **b)** A close-in view of the set point shows a -5% +15% spread in the magnitude of the tunnel current at the set point. This is typical of any set of I(V) data on any sample and corresponds to a ±0.01nm variation in tip-sample separation.

5.7 The Dielectric Model

Given the success of modeling Au with the simple one-dimensional tunnel model presented above, the next logical step is to extend the modeling to a Au substrate coated with a molecular SAM. However, unlike Au and Pt, for the molecule the assumption that the density of states is relatively constant, is not valid. Based on calculations,[1,38] most organic molecules exhibit a distinct conduction gap and have HOMO and LUMO states. Consequently, the simple barrier model presented above is

clearly insufficient to the task of calculating I(V) through molecular monolayers. However, many of the characterization techniques[64] discussed in Chapter 4 require knowledge of the dielectric properties of the organic SAMs; consequently, it may be useful to consider the effects of a dielectric layer on STS. In particular, the effects of the molecular density of states become less significant in situations where the energies being probed are constant (i.e. fixed voltage situations). In these situations, dielectric effects may become apparent.

Through the inclusion of a dielectric layer a modified experiment (Figure 5.19) and a modified barrier (Figure 5.20) are generated. The effect of a classical electrostatic dielectric layer is to lower the electric field within the dielectric material, thus resulting in a lowing of the voltage drop in that region. This in turn tends to keep the average voltage in the dielectric region closer to the electrical potential of the substrate then that of the tip; this is because the dielectric layer is in contact with the substrate. The effect on the tunnel barrier can be dramatic, and results in an asymmetry in the barrier with respect to the polarity of the voltage bias. For negative bias voltages, the presence of a dielectric tends to increase the barrier height (Figure 5.20a) and thus reduce the magnitude of the tunnel current (Figure 5.21a). For positive bias voltages, the presence of a dielectric tends to decrease the barrier height (Figure 5.20b) and thus increase the magnitude of the tunnel current (Figure 5.21a). The effect of the dielectric on the I(V) data is dramatic and results in a significant increase in the asymmetry of the I(V), especially for large values of V_{set} (Figure 5.21b).

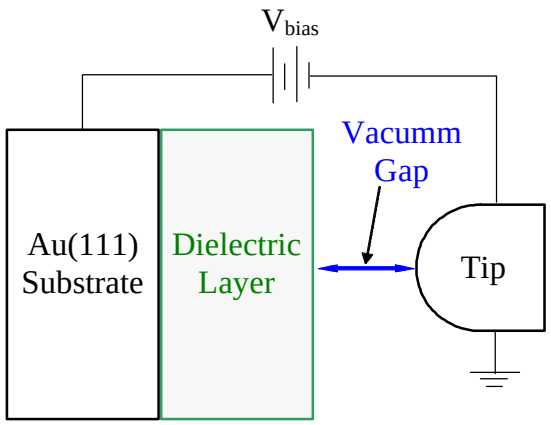

Figure 5.19

Schematic of STM tunnel junction with a dielectric layer between the metal contacts (i.e. the Au substrate and the Pt tip).

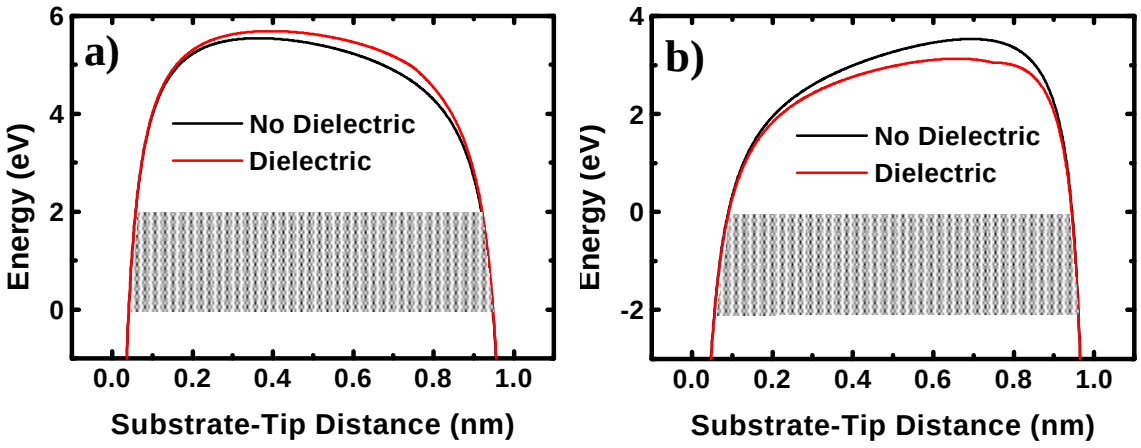

Figure 5.20

The introduction of a dielectric layer (0.75nm) into the barrier region (1.0nm) changes the shape of the barrier when an applied bias is placed across the tunnel junction. The dielectric is placed on top of the substrate (i.e. the left side of the barrier; see Figure 5.19) and a 0.25nm gap exists between the top of the dielectric layer and the STM tip (i.e. the right side of the barrier) The energy scale is relative to the grounded tip ; the gray shaded regions depict the range of energies that would be evaluated in equation 3.8. A derivation of the barrier equations is given in Appendix B. **a)** Schematic of a 1-dimensional tunnel barrier with and without a dielectric layer under a negative applied bias (-2 Volts). For negative bias voltages, the presence of a dielectric tends to increase the barrier height and thus reduce the magnitude of the tunnel current. **b)** Schematic of a 1-dimensional tunnel barrier with and without a dielectric layer under a positive applied bias (+2Volts). For positive bias voltages, the presence of a dielectric tends to decrease the barrier height and thus increase the magnitude of the tunnel current.

Comparing the modeled dielectric I(V) results (Figure 5.21) to actual I(V) data obtained on various variations of alkane chains (Chapter 7 and Chapter 8) we see that the dielectric model behaves in a manner opposite to the molecules. Most notably, the dielectric model predicts increased current flow for large positive bias relative to negative biases where as the majority of molecules studied herein show the opposite behavior.

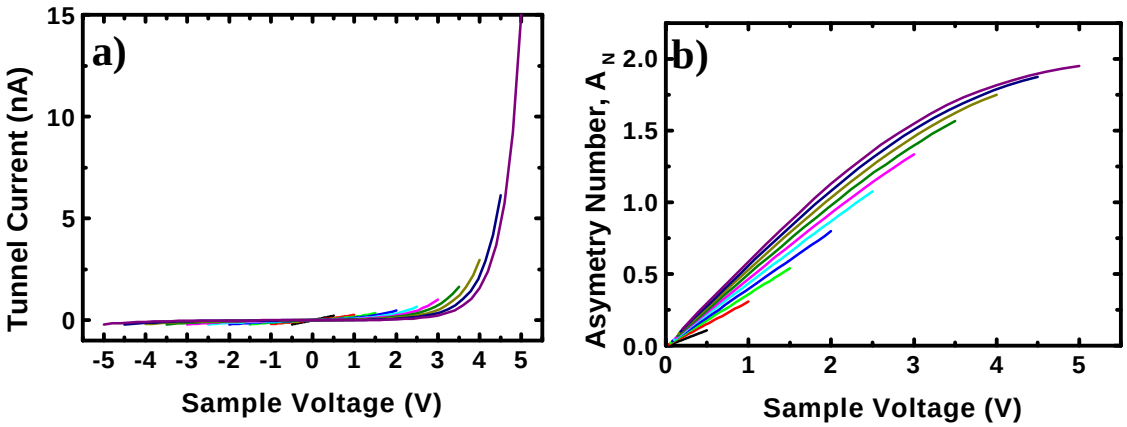

Figure 5.21

a) I(V) data generated using the simulation program. The model barrier in this case includes a 0.75 nm dielectric layer. **b)** The result of inserting the dielectric layer is a large asymmetry in the I(V) resulting in significantly more current flow for positive bias voltages.

Figure 5.22(a) shows I(Z) taken by S. Hong[12] on Terphenylthiol. The change in slope of the Log(I) vs. Z data was interpreted by Hong to be the point at which the tip comes into contact with the molecular SAM. Figure 5.22(b) shows I(Z) data calculated using the dielectric model. The simple dielectric model predicts similar behavior as experiment, a change in the slope of Log(I) becomes apparent when the tip comes into contact with the dielectric layer (as shown by the blue and green lines in Figure 5.22(b)). However, like our simulation on Au presented earlier, $\varphi_{exp} < \varphi_{sim}$ (see Table 5.2) and the change in φ resulting from contact with the SAM is less dramatic in the simulation model then in actual experiment. Additionally, the current magnitudes at which contact with the

molecular/dielectric surface occur in the experiment and in the simulation differ by two orders of magnitude. Presumably, this large difference in the current values is due to the effects of energy states in the Terphenylthiol. The implication is that in constant voltage situations, dielectric effects may be present, but as expected, the dielectric model is insufficient to modeling molecular monolayers.

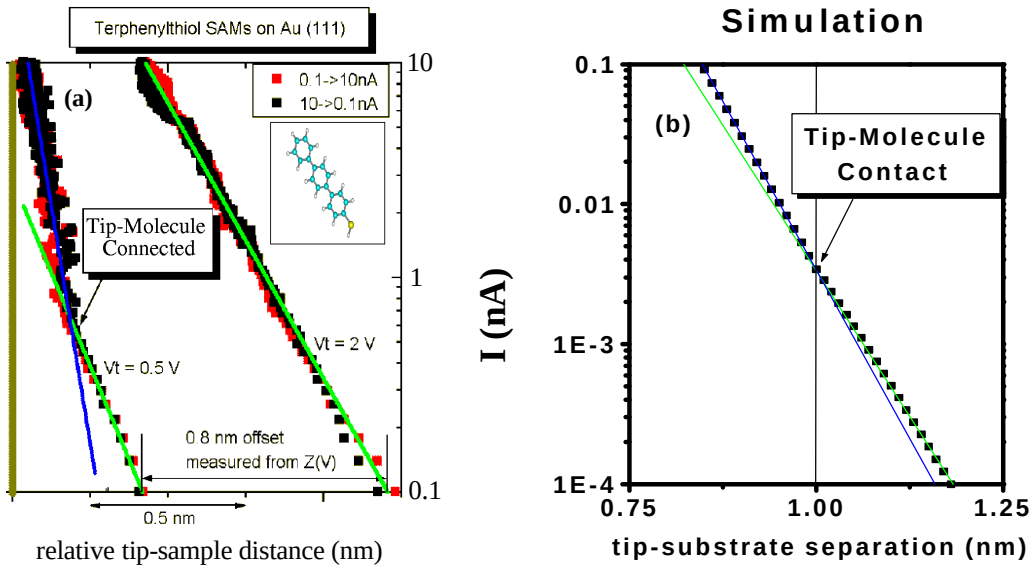

Figure 5.22

(a) I(Z) data taken by S. Hong (Dept. of Physics, Purdue U.) on Terphenylthiol. The change in the slope was interpreted as contact between the tip and molecule. **(b)** Simulation based on the dielectric model shows similar behavior (as shown by the blue and green lines) but a much less dramatic effect.

Table 5.2

Values of φ as calculated from Figure 5.22

	Experiment	Simulation
φ when tip in contact	3.5eV	4.5eV
φ when tip not in contact	0.8eV	3.8eV

5.8 Conclusions

In this chapter a one-dimensional model of an STM tunnel junction has been developed. Numerical calculations show that the model is in good agreement with experimental results, modeling I(V) to within 5% of experimental measurements. Using this model we have gained a critical insight to STM behavior on metal-to-metal tunnel junctions, namely, sub-Angstrom control of the tip position relative to the sample may be achieved through the use of V_{set} as a control variable for fixed values of I_{set}. The implication is that through the use of I_{set} as a coarse control and V_{set} as a fine control of tip-sample position, it may be possible to convincingly approximate a true two-terminal measurement of a molecule through the use of STS. The remaining difficulty lies in knowing when the tip comes into contact with the molecular SAM. Also, high electric fields at the tip apex interacting with the SAM may produce unknown effects. The values of the tip-substrate separation shown in Figure 5.17 are, in general, less than the height of the molecules under investigation. In order for the tip not to be buried in the SAMs, increased electron transmission, possibly resulting from energy states within the molecule, is required.

6. CHEMICALLY DOPING AN ORGANIC MOLECULE

6.1 Background

Prior work[1,34,36] has demonstrated that the location of the equilibrium Fermi level relative to the HOMO-LUMO gap of a molecule is an important factor in determining the molecular resistance. For the case when the molecule makes a good electrical contact to two electrodes, the resistance could be near 12.9KΩ, the quantum of resistance, if the Fermi level is aligned with either the HOMO (or LUMO) of the molecule and the conduction mechanism is ballistic. However, the large resistances measured (on the order of MΩ)[4,17,32] clearly indicate that the Fermi level usually lies close to the center of the HOMO-LUMO gap of common unsaturated organic molecules as depicted in Figure 6.1(A).

The question then arises: *"Can an organic molecule be modified so that the Fermi level is aligned with one of its energy states? i.e. Can an organic molecule be doped and thus become an Ohmic conductor?"* The nature of this "doping" may take several different forms. The molecule could be modified so that its Fermi level aligns itself with a pre-existing energy state of the molecule (Figure 6.1(B). This would be achieved by adding or removing electron charge from the molecule. Alternatively, the molecule could be modified through the generation of a new energy state at or near the Fermi level (Figure 6.1(C)). This could be achieved through a chemical interaction where hybridized energy states are generated. In either case, the result would be a significant drop in the low-bias resistance of the molecule due to enhanced conduction through the energy state at the Fermi level.

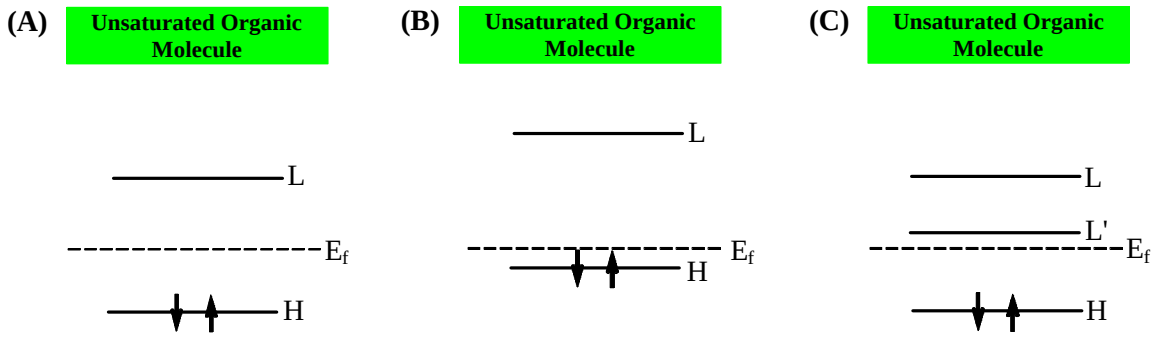

Figure 6.1

(A) Energy diagram appropriate for an unsaturated organic molecule chemically bonded to a metal surface. For such molecules, the Fermi level lies in the HOMO-LUMO gap. **(B)** One possible scheme to make a molecule conducting at low bias is to adjust the location of its Fermi level by adding or removing charge from the molecule. **(C)** Another possible scheme to making an organic molecule conducting for low bias is to introduce states into the gap region through some form of a doping process.

One proposed solution to the "molecular doping" question was proposed by Prof. Kubiak (Department of Chemistry & Biochemistry, University of California, San Diego). He suggested that the formation of a charge-transfer (CT) complex between an electron donor and an electron acceptor (Figure 6.2A), could sufficiently modify the energy state configuration of the electron donor so that the Fermi level would be aligned with an energy state (Figure 6.2B). The basis of this prediction rest upon previous work[84-94] which show that bulk solutions and crystals of many CT complexes are conducting/metallic in their behavior.

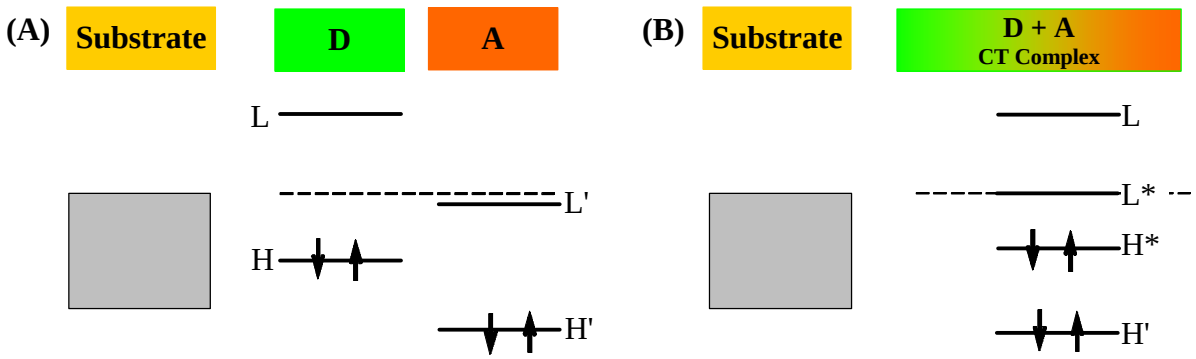

Figure 6.2

(A) A candidate for the formation of a charge transfer (CT) complex requires an electron donor, D, with a HOMO below the Fermi level and an electron acceptor, A, with a LUMO below the Fermi level. Such a situation allows for the chemical `doping' of an individual molecule. **(B)** Once the CT complex is formed, hybridized energy levels L* and H* form. Should one of these hybridized energy levels be at or near the Fermi level, the resulting CT complex will exhibit conducting behavior.

The implication of this previous work is that if a self-assembled monolayer of an appropriate electron donor can be formed, then conducting behavior of a "single" molecule (or small number of molecules) can be changed through the formation of a CT complex with an electron acceptor. However, in order for a CT complex to be conducting, it is not enough to merely have an extensive interaction between the molecular orbital of the donor and acceptor. It is the occupancy of the energy levels that is crucial. For metallic conduction, there must be partially filled energy levels through which the electrons can move easily into infinitesimally higher energy states within the band. Thus, the electrons in the HOMOs very near the Fermi level (E_f) dictate the physical/conductivity properties of CT complexes. A comprehensive review of the developments in the study of conducting charge transfer salts has been written by Bender[95] and more recently, by Bryce.[96] The simplest molecular orbital treatment of the CT complexes involves the transfer of an electron from the HOMO of the donor to the LUMO of the acceptor[97] resulting in an ionicly bonded complex of two separate molecules. The electrical properties vary from insulating to superconducting.[96]

In the study presented here, the formation of a surface charge transfer complex at the molecular length scale is accomplished by the reaction of a strong electron acceptor (tetracyanoethylene, TCNE) (Figure 6.3) with a SAM of an electron donor (tetramethyl xylyl dithiol, TMXYL) (Figure 6.4). This reaction is found to increase the density of states near the Fermi level, resulting in a 50-fold increase in the conductivity as measured by STM. These results demonstrate for the first time that a simple additive chemical reaction can be used to gate current flow through a SAM by inducing a change from insulating to conducting behavior. Such a result implies that a SAM that is normally insulating can be 'doped' to achieve specific conducting or semiconducting electronic properties.

Figure 6.3

Tetracyanoethylene, TCNE, electron acceptor used as the "dopant" in the charge-transfer complex under investigation.

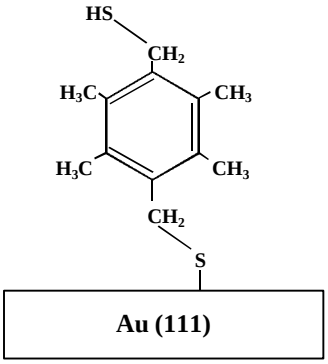

Figure 6.4

Tetramethyl xylyl dithiol, TMXYL, single-thiol bonded to Au(111). TMXYL acts as the electron donor in the charge-transfer complex under investigation.

Organic charge transfer (CT) complexes can be viewed as the result of the reaction of an electron donor molecule (D) with an electron acceptor molecule (A). TCNE is a relatively strong π-acceptor molecule and readily forms a CT complex with the electron donor, hexamethyl benzene. A new dithiol, TMXYL, (see reference 98 and Appendix C) was prepared, since it was expected to possess both the ability to form SAMs and sufficient electron donor character to form an organic CT complex with TCNE. SAMs of TMXYL and TMXYL-TCNE were prepared (Appendix C) on Au substrates (Appendix C) and characterized by Reflection Absorption Infrared Spectroscopy (RAIRS) (Table 6.1), ellipsometry (Table 6.2), electrostatic force microscopy (Table 6.3), and contact angle (Table 6.2) measurements. The characterization of the molecules by these techniques supports the morphology illustrated in Figure 6.5 (note: to avoid confusion, a naming convention is established in Figure 6.5). The conductance of these SAMs was subsequently investigated by Scanning Tunneling Microscopy (STM) using techniques previously discussed in Chapter 4.

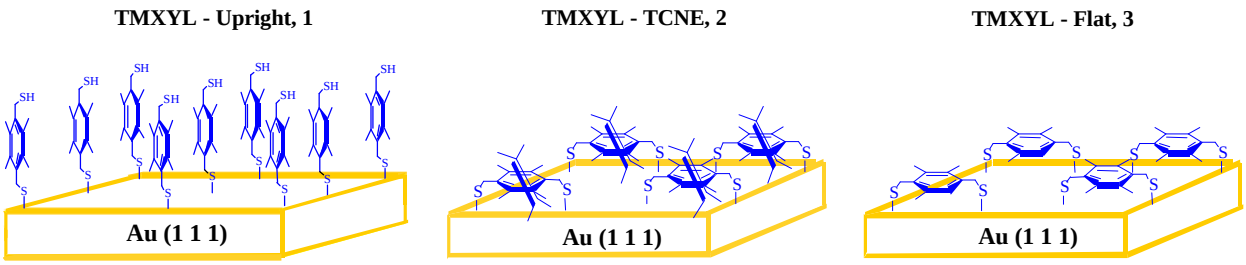

Figure 6.5

A schematic of the three samples prepared in this study. RAIRS data from TMXYL-upright, **1** indicates that TMXYL is single-thiol bonded to Au(111) with an upright orientation. The process of reacting TMXYL with TCNE causes the TMXYL to go from an upright to a horizontal orientation, indicative of a molecule bonded to the Au(111) substrate via both thiol end-groups. RAIRS confirms that the TMXYL molecules are parallel to the Au(111) surface with the TCNE resting on top. After the TCNE is removed, the TMXYL remains bonded to Au(111) through both the thiol groups. Consequently the molecules are parallel to the Au(111) surface. SAMs of **1** were made as a processing step towards SAMs of **2** and **3**.

6.2 Characterization of TMXYL-based SAMs

Synthesis of TMXYL and the subsequent formation and characterization of TMXYL-based SAMs was performed Bala Sundari T. Kasibhatla under the direction of Professor Clifford P. Kubiak (Department of Chemistry & Biochemistry, University of California San Diego). AFM studies were performed by Stephen Howell (Department of Physics, Purdue U.). The results of this work are summarized here and additional information may be found in Appendix C.

6.2.1 The Properties of a SAM of TMXYL: TMXYL – Upright (**1**)

RAIRS data for **1** (Table 6.1) suggest that the TMXYL molecule is oriented vertically on Au(111) (Figure 6.5). This is evident from the increase in the intensity of the infrared (IR) vibrational bands at 1590 cm^{-1} (**8a**) and 1472 cm^{-1} (**19a**). These bands correspond to vibrational modes with a net dipole change that is along the long axis of the TMXYL molecule. Ellipsometry and contact angle measurements are consistent with the proposed vertical orientation of TMXYL (Table 6.2) The relatively small positive surface potential measured via conducting AFM (Table 6.3) is consistent with the dipole associated with Au-S bonds.

6.2.2 Formation of a Surface Confined Charge Transfer Complex: TMXYL-TCNE (**2**)

The SAM of **2** was prepared in two steps. The first step was the formation of a SAM of **1** on Au(111) as described above. The second step involved the immersion of the TMXYL coated Au(111) substrate in a concentrated (0.1M) CH_2Cl_2 solution of TCNE. The RAIRS spectrum of **2** shows an intense band at 1378 cm^{-1}, corresponding to the CH_2 out-of-plane bending mode of TMXYL. In contrast, the in-plane mode at 1437 cm^{-1} (**19b**) decreases significantly in intensity. This suggests that TMXYL is now lying flat with respect to the Au(111) surface, bound through both thiol groups (Figure 6.5). In addition, the out-of-plane "puckering" mode of TCNE at 554 cm^{-1} shows a significant increase in intensity. These data suggest that TCNE is also lying flat with respect to the metal surface, presumably on top of TMXYL. Ellipsometry and contact angle measurements are consistent with the proposed horizontal orientation of TMXYL-TCNE **2** (Table 6.2). In particular, the two-component

SAM of TMXYL-TCNE **2** is found by ellipsometry to have a thickness that is 0.2 nm less than that of a SAM of TMXYL **1** alone. The CT complex is highly ionic in nature, resulting in a strong dipole moment directed towards the electron donor (i.e. TMXYL). The relatively large negative surface potential measured is consistent with the formation of a CT complex with the electron acceptor (i.e. TCNE) sitting on top of the electron donor (TMXYL).

6.2.3 Properties of a SAM of TMXYL after removal of TCNE: TMXYL - Flat (**3**)

TCNE was removed from **2** by immersion in a solution of the strong electron donor, trimethyl tetrathiafulvalene (Me_3TTF). The RAIRS spectrum of **3** shows the same intense band at 1374 cm^{-1}, as seen in the RAIRS of the charge-transfer SAM **2**, suggesting that TMXYL remains flat on Au(111) (Figure 6.5). The absence of the out-of-plane bending mode at 554 cm^{-1} also confirms the removal of TCNE from the surface. The relatively small positive surface potential measured via conducting AFM (Table 6.3) is consistent with the dipole associated with Au-S bonds.

Table 6.1

RAIRS data for the various SAMs used in this study. The direction of the arrows in the last column indicates the relative change in intensity of the appropriate spectral bands for selected vibrational modes relative to the bulk (KBr pellet) IR spectrum. (data taken by Bala Sundari T. Kasibhatla, UCSD)

SAM	**ν (cm^{-1})**	**Vibrational mode Assignment**	**RAIRS Intensity**
TMXYL-Upright, 1	1590	**8a**,C-C stretch	↑
	1472	**19a**,C-C stretch	↑
	1439	**19b**,C-C stretch	↑
	1297	**14**,C-C stretch	↑
TMXYL-TCNE, 2	1437	**19a**,C-C stretch	↓
	1378	CH_2 out of plane bend	↑
	554	C-CN out of plane bend	↑
TMXYL-Flat, 3	1374	CH_2 out of plane bend	↑

Table 6.2

Ellipsometry and water contact angle data for various SAMs used in this study.
(data taken by Bala Sundari T. Kasibhatla, UCSD)

SAM	Ellipsometry Film Thickness (nm)	Contact Angle (θ)
TMXYL-Upright, 1	0.80	80°
TMXYL-TCNE, 2	0.60	71°

Table 6.3

AFM surface potential measurements indicate the relative strength and polarity of surface dipole moments resulting from SAM coating. As expected, the TMXYL-TCNE has a strong dipole moment. The negative value indicates that the TCNE sits on top of the TMXYL molecule. (data taken by Stephan Howell, Purdue U.)

SAM	Surface Potential (mV)
TMXYL - Upright, 1	16 ± 70
TMXYL-TCNE, 2	-142 ± 25
TMXYL - Flat, 3	27 ± 60

6.3 Scanning Tunneling Microscope Results

Scanning Tunneling Spectroscopy (STS) was used to probe films of TMXYL-Upright,**1**, TMXYL-TCNE, **2**, and TMXYL-Flat,**3**. Two physical effects were measured in these experiments: The first effect examined was a change in the conductivity of TMXYL resulting from chemical doping with TCNE; this effect is seen in a comparison of **2** to **3**. The second effect examined was the change in conductivity of TMXYL resulting from a morphology change; this effect is seen in a comparison of **1** to **3**.

Figure 6.6 shows the averaged I(V) data taken on **2** and **3** for a series of V_{set}. The I(V) data for **2** maintains its basic character across set voltages; and the slight increase in asymmetry observed is consistent with field enhancement do to the sharp tip (see Figure 6.7). I(V) data for **3** maintains its insulation behavior for small voltages (V < 1V); however, an interesting feature arises for larger

positive voltages as a function of V_{set}. The lowest set voltage (i.e. V_{set} = 1.5V) results in a relatively symmetric I(V) and the next higher set voltage (V_{set} = 2.0V) results in a highly asymmetric I(V). This change from symmetric to asymmetric I(V) has been observed on numerous molecules and has been explained as a change in the voltage division factor, η (see Chapter 4 and Chapter 7). What complicates the analysis in this case, is the sudden return to a symmetric I(V) for an even higher V_{set} (i.e. V_{set} = 2.5V). This interesting "switching" behavior is as yet unexplained, but may be another mechanism for the development of novel molecular electronic circuit elements.

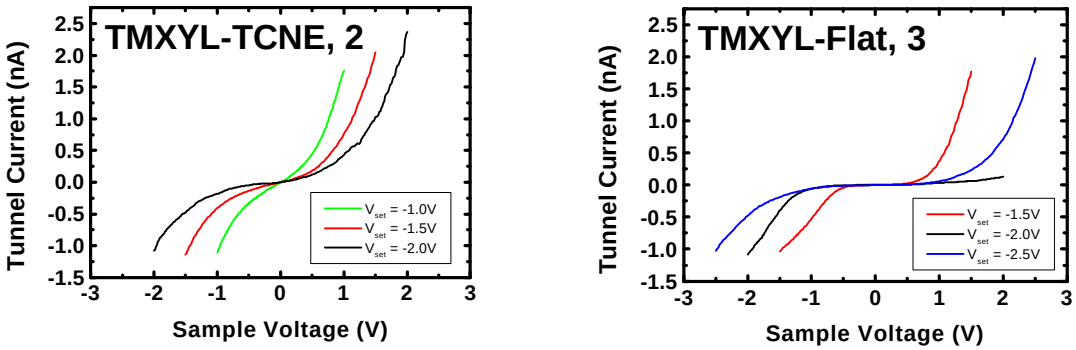

Figure 6.6

I(V) data for TMXYL-TCNE and TMXYL-Flat. TMXYL-TCNE clearly has a non-zero slope for small bias voltages resulting in Ohmic behavior for V_{bias} < 0.5V. TMXYL-Flat demonstrates no appreciable current flow for small bias voltages resulting in a conduction gap. This change in conductivity (from insulating to Ohmic-conducting) is a direct result of the formation of the CT complex.

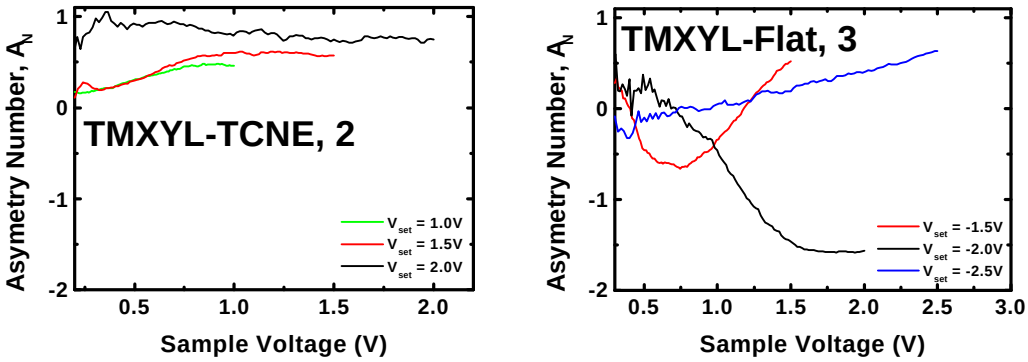

Figure 6.7

The Asymmetry Number, A_N, give a relative measure of the asymmetry in I(V) data. A value of zero indicates prefect symmetry. For TMXYL-TCNE we see a slightly increasing value of A_N for increasing values of V_{set}; this result is consistent with electric field enhancement effects due to the sharp STM tip. For TMXYL-Flat we see that I(V) data for V_{set} = -2.0V is relatively more asymmetric for higher values of V_{bias} than corresponding I(V) data for V_{set} = -1.5V and -2.5V. This is particularly evident if A_N is examined for each I(V) at $|V_{bias}| = |V_{set}|$ Such behavior is currently unexplained and is not consistent with the models previously described.

It is useful to compare the Scanning Tunneling Spectroscopy (STS) results obtained from **2** and **3** (see Figure 6.8) at the same set conditions (i.e. V_{set} and I_{set}). The measured conductance near zero bias has two contributions – one due to the tunnel gap between tip and molecule and a second due to a few molecules (perhaps only one) through which the tunneling current must flow. When the tip is brought close to the molecule so as to produce a negligible tunnel gap, the electronic properties of the molecule can dominate the measured I(V). It is important to be in this regime when comparing STS spectra from **2** and **3**.

In this study, this was accomplished by systematically measuring I(V) as a function of set point voltage and current. As the set point voltage is reduced for a fixed tunnel current, the I(V) data becomes reasonably symmetric, indicating the capacitive coupling between the tip and molecule is comparable to the capacitive coupling between the molecule and the tip. Under these circumstances (a tunnel resistance of ~1.5 GΩ for the SAMs investigated here), we have determined that the apex of the tip is close but not buried in the molecular SAM.

With the STM in stable operation under these conditions, the feedback was disabled and the voltage bias between substrate and tip was ramped, generating I(V) data at 256 different values of the bias voltage. Under ideal circumstances, when I(V) data is acquired as described above, the resulting tunnel gap between tip and molecule should be identical for both **2** and **3**. Thus, any observed changes in the I(V) can be interpreted as changes in molecular conductance, a quantity of considerable interest. Under actual operating conditions, to achieve a given set point, the tip-molecule separation is greater for a more conducting molecule. Since **2** is found to be more conductive than **3**, it follows that differences observed in I(V) (or dI/dV) near zero bias will tend to underestimate the actual differences in the conductance between the two molecular SAMs under investigation.

A comparison of the STM data for **2** and **3** provides important information about the molecular electronic effects induced by the formation of a charge transfer complex. The I(V) data are shown in Figure 6.8. The data were taken at V_{set} = -1.5V and I_{set} = 1.0nA. For **2,** a V_{set} of 2.0V or higher resulted in erratic tunnel current, presumably due to the large electrostatic forces on the CT complex. STM I(V) data for **2** clearly show Ohmic behavior for $|V| \leq 0.5V$, indicating that the TMXYL-TCNE CT complex has a very different electronic behavior compared to **3** (TMXYL- Flat).

The change from insulating to conducting behavior at low bias by the addition of TCNE is most clearly seen by a direct comparison of dI/dV. dI/dV derived from representative I(V) data of **2** and **3** are shown in Figure 3. The data show that the zero-bias conductivity of **2** is a factor of at least 50 greater than that of **3.** In comparing the relative conductivity of **2** and **3** at 0.01nA/V (the estimated noise level of our system), we find that **3** exhibits a conduction gap while **2** does not.

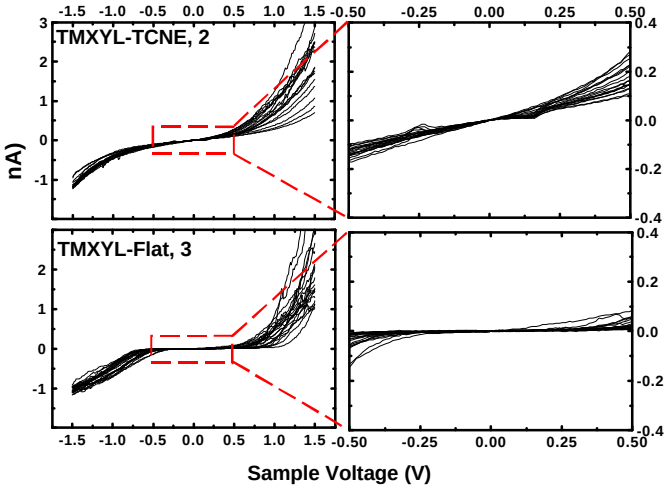

Figure 6.8

A comparison of I(V) data from **2** and **3** at the same set conditions (V_{set} = -1.5V and I_{set} = 1.0nA). I(V) data from **2** indicates that the CT complex is an electrical conductor, with a nearly linear I(V) behavior at V=0. When the TCNE molecule is removed**,** I(V) data from **3** indicates that for small voltages (|V| < 0.5V), TMXYL is an electrical insulator. This data combined with the I(V) data on TMXYL-TCNE indicates that the change from insulator to conductor through the formation of a CT complex results from a change in the molecular energy levels. Approximately 25 separate I(V) spectra, taken from various regions across the sample, are plotted simultaneously to indicate the overall reproducibility of the data. The data have been reproduced on two separate samples.

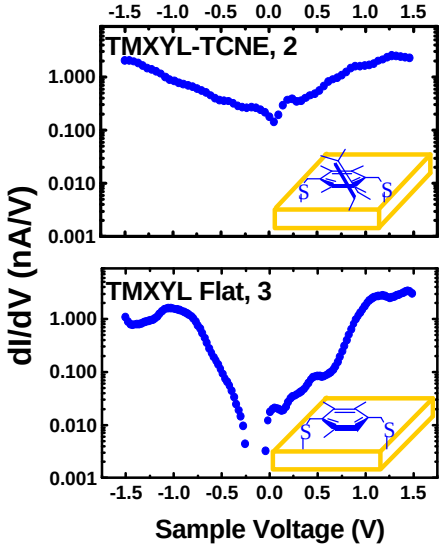

Figure 6.9

A comparison of dI/dV data from **2** and **3** at the same set conditions (V_{set} = -1.5V and I_{set} = 1.0nA).dI/dV data for TMXYL-TCNE, **2** and TMXYL-Flat, **3** plotted on a $\log_{10}$ scale. The dI/dV were calculated from a representative I(V) shown in Figure 6.8. Near zero bias, **2** is found to be approximately 50 times more conductive than **3**.

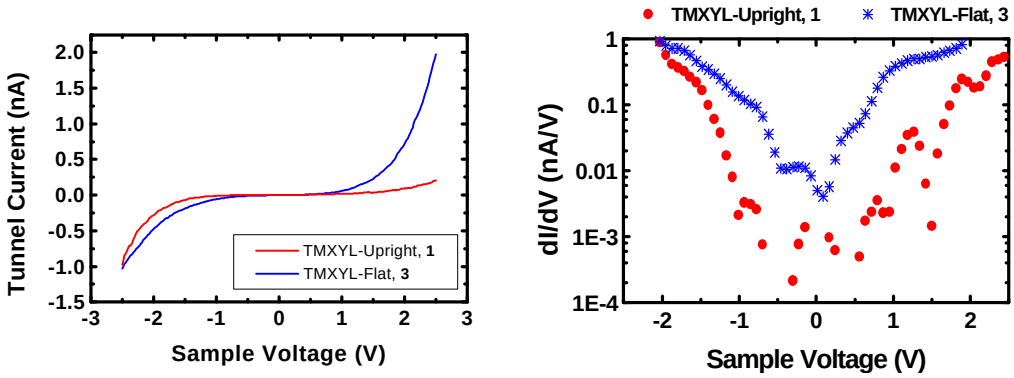

Figure 6.10

I(V) data from TMXYL clearly shows that TMXYL is an insulator for small bias voltages irregardless of orientation. The reduced conductivity of TMXYL-Upright, **1**, relative to TMXYL-Flat, **2**, is due to the increased height of **1** relative to **2**.

It is useful to assess the change in conductivity resulting from the structural change of the TMXYL molecule on the metal surface between **1** and **3**. We therefore examined a SAM of TMXYL – Upright, **1** (see Figure 6.5). I(V) data for **1** indicates insulating behavior with little conduction evident for $|V| \leq 1.0V$ (see Figure 6.10). However, **3** appears somewhat less insulating then **1,** presumably because SAM **3** is not as thick. The relatively small difference in conductivity of **1** and **3** is attributed to the orientation change of the molecule from vertical (**1**) to horizontal (**3**). However, the TMXYL molecules in **2** and **3** share similar physical orientations, but conduct quite differently. Consequently, the change from the Ohmic behavior observed for **2** to the insulating behavior observed for **3** results from the removal of the electron acceptor, TCNE. The removal of TCNE eliminates the CT interactions, which returns insulating properties to the SAM.

The evidence for Ohmic conduction in the TMXYL-TCNE CT monolayer **2** is compelling and indicates that **2** has energy states near the Fermi energy. The clear difference between the I(V) of **2** and **3** demonstrates that a change in the conductance of the TMXYL is due to the creation of the TMXYL-TCNE CT complex and not due to the change in morphology. An energy diagram consistent with these observations is provided in Figure 6.11 (thanks to Ferdows Zahid and Prof. Supriyo Datta,

Purdue University). This energy diagram is obtained using the DFT method, B3PW91 with 6-31G* basis function as implemented in the chemistry software Gaussian 98.[99] This method (B3PW91) combines the Becke exchange functional[100] and Perdew-Wang correlation functional[101]. Figure 6.11 shows the energy levels of TMXYL and TCNE molecules along with those of the CT complex. The CT complex is modeled by placing TCNE on top of TMXYL at a distance of 0.285 nm. The substrate Fermi level can be assumed to be located around –5.1 eV (work function of bulk gold), although a more detailed calculation is needed to locate it precisely with respect to the molecular levels. But the point to note is that the CT complex gives rise to an additional hybridized level (L*) close to the Fermi level leading to an increase in the density of states. This increase contributes to increased conduction since this level is delocalized that is, it hybridizes with the substrate through the sulfur atoms of TMXYL. This simple physical picture provides a mechanism for an important capability in molecular electronics, the ability to alter the electronic properties of an individual molecule by a molecular doping process.

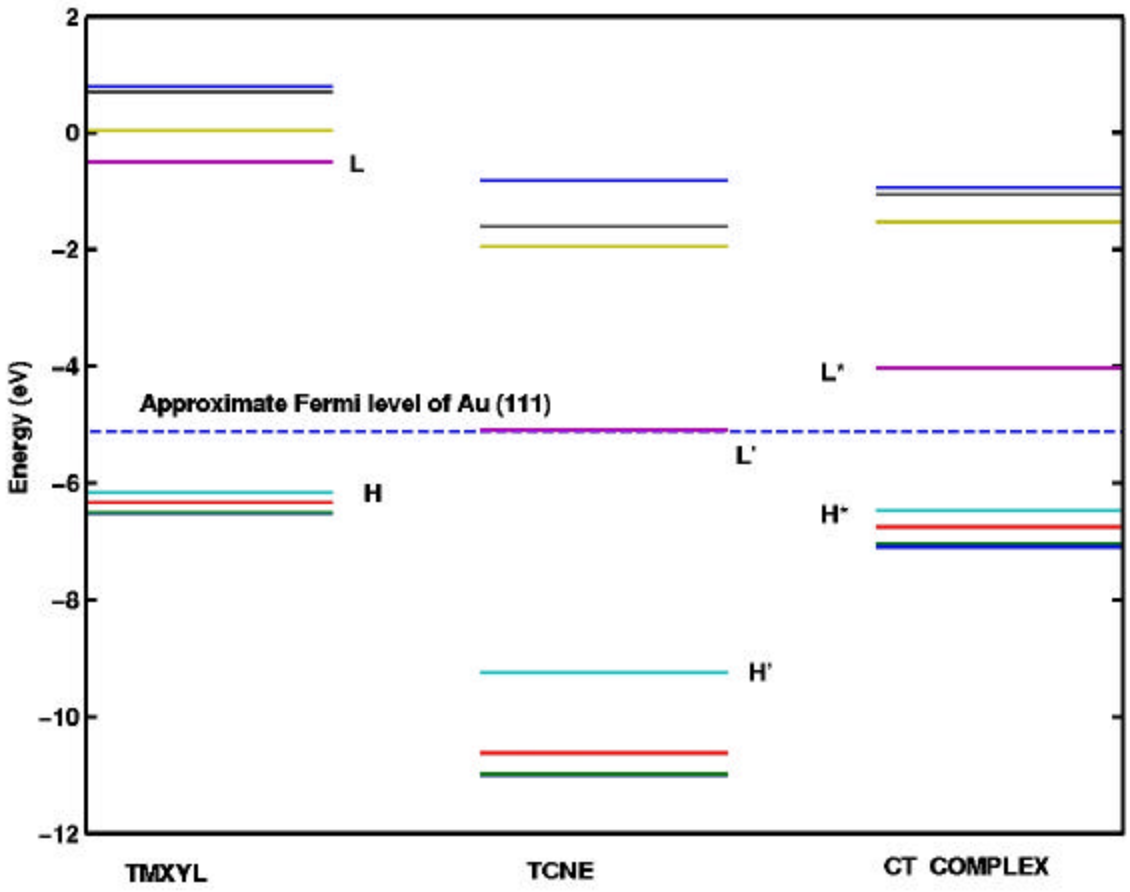

Figure 6.11

Energy levels of TMXYL and TCNE molecules along with those of CT complex. This result is obtained from B3PW91 method with 6-31G* basis using Gaussian 98. Approximate Fermi level (-5.1 eV) of Au (111) is indicated with broken line. (thanks to Ferdows Zahid and Prof. Supriyo Datta, Purdue University)

6.4 Conclusions

In summary, self-assembled monolayers of the dithiol TMXYL were synthesized on a Au(111) substrate. The addition of the electron acceptor, TCNE, caused a charge-transfer complex of TMXYL with TCNE to be formed. The surface morphology of the SAMs were characterized by reflection absorption infrared spectroscopy, ellipsometry, electrostatic force microscopy and contact angle measurement. I(V) data obtained in UHV by an STM revealed a significant change in the

conductance spectra between the TMXYL and TMXYL-TCNE SAMs. SAMs formed from TMXYL alone produced I(V) data similar to that reported elsewhere for poly(phenylene) thiols.[12] The magnitude of the measured energy gap in the conductance spectra places the HOMO of TMXYL (level H in Figure 6.11) approximately 1eV below E_F of Au (111). Upon addition of TCNE, a considerable change in the conductance spectra occurred, resulting in I(V) data that were nearly Ohmic near V= 0 and showed no evidence of a gap in the conductivity. This result is consistent with the introduction of CT complex hybridized levels that coincide with the Fermi energy of the system (see Figure 6.11). Upon removal of the TCNE molecule, the insulating character of the self-assembled monolayer was essentially restored.

The significance of this experiment is the clear demonstration that the conductance of an individual molecule can be altered in a controlled and reversible manner. This establishes the feasibility of using current flow through a suitably designed SAM as a sensitive means of detecting the presence (or absence) of a specific target molecule. It is not possible in general to dope individual molecules to levels of small partial charge, as is commonly practiced with semiconductors and conducting polymers to achieve specific conductivities. However, the large and reversible change in conductivity of individual molecules demonstrated for the TMXYL-TCNE system suggests a new molecular technology for fabricating conductive elements useful in future molecular electronic applications.

7. STS MEASUREMENTS ON HIGHLY RESISTIVE ORGANIC MONOLAYERS

7.1 Background

Self-assembled monolayers (SAMs) of organic compounds on metal surfaces are commonly involved in the proposed design of functional devices with molecular and nanoscale dimensions.[20-24,29] An important quality of many SAMs is their intrinsically low electrical conductance, a passive but essential feature for the realization of nanoscale electronic devices. Inadequate insulation is presently considered to be a serious hindrance to the continued miniaturization of integrated circuits; for example, quantum mechanical electron tunneling becomes the dominant source of leakage current across metal-oxide junctions as gate oxide thickness drops below 5 nm. For silicon dioxide (SiO_2), recent studies indicate that the leakage current will increase by almost 12 orders of magnitude as the thickness changes from 3.5 nm to 1.5 nm.[102] Quantum-mechanical calculations suggest a minimum SiO_2 thickness of 1.5-2.0 nm for chip standby power requirements,[103] but variations in oxide thickness by as little as 0.1 nm on a Si wafer could result in drastic variations in efficiency, making it very difficult to maintain device tolerances.

Organic SAMs are intriguing alternatives to SiO_2 as electrically insulating materials. Well-ordered SAMs have highly uniform thicknesses and can be designed with tunable interfacial properties, providing unique processing advantages for device fabrication. The electrical properties of SAMs have obvious ramifications for nanostructured device engineering; for example, SAMs comprised of bifunctional molecules have enabled the layered deposition of conductive or semiconductive nanoparticulate films.[17] Electron-transfer rates across insulative SAMs on Au(111) surfaces have been studied by bulk electrochemical methods in aqueous environments, and have been correlated with changes in chain length and SAM thickness.[64,104-106] However, these methods are

limited by the heterogeneity of the environmental conditions and the presence of pinhole defects, and cannot be interpreted straightforwardly for quantitative measurements of electrical resistance.

In this paper we present a systematic method for characterizing the tunneling barrier across highly insulating SAMs on Au(111) using scanning tunneling spectroscopy (STS) techniques. Previous STS studies[1,4,17] have been used in conjunction with theoretical developments pioneered by Datta[1,34,36,38] to estimate the electrical resistance of organic molecules as a function of molecular structure and chemical bonding.[12] Such treatments can in principle be extended to more insulating molecules if significant transmission is achieved with higher bias voltages, but the low tunneling currents involved (often less than 1 pA) can introduce substantial experimental error, to the extent that it may overwhelm the actual measurement. To this end, we have determined that the systematic evaluation of conductance as a function of the applied tip voltage significantly reduces the error, thereby enabling us to make more reliable estimates for the resistance of a single or "small number" of molecules.

7.2 Theoretical Considerations

Chapter 3 provides the theoretical background behind the experiments presented here. However, as a result of my experiments, my understanding and interpretation of certain aspects of that theory have been modified and expanded. Consequently, a brief review of that theory combined with a discussion of the new implications is required.

The tip-molecule-substrate system can be modeled as a tunnel junction with the molecule serving as a dielectric.[1,4,12,17] Ideally one would like to measure the resistance of a molecule within a SAM as a function of applied voltage (V_{bias}), but direct measurements are difficult to interpret if the STM tip is not in physical contact with the transporting molecule, presenting a gap of unknown dimensions. Formally, using the Landauer-Buttiker formalism, the current-voltage ($I(V)$) relationship can be calculated if the transmission probability $T(E, V_{bias})$ of an electron through a molecule is known as a function of applied bias voltage V_{bias}. The operational equation is equation 3.8 and is restated here:

$$I = \frac{2e}{h} \int_{-\infty}^{\infty} dE \cdot T(E,V)\left[f(E-\mu_t) - f(E-\mu_s) \right] \tag{7.1}$$

In equation 7.1, E is the electron energy, μ_t and μ_s are the Fermi energy levels of the tip and the substrate respectively (see Figure 7.1a) and $f(E)$ is the Fermi-Dirac distribution function. At room temperature, the cut-off in the Fermi-Dirac function effectively restricts the limits of the integral in equation 7.1 to μ_t and μ_s. Calculations based on this formalism have been widely used to describe the molecular conductance (and resistance) of a number of organic structures based on their conductance spectra.[12,32-36,39,107] It is worth mentioning that molecules with similar chemical structures can give rise to completely different conductance spectra if the transmission function is modulated by extrinsic factors such as differences in chemical bonding at the substrate-molecule interface.

Two factors are critical in determining molecular conductance: $T(E,V)$ itself, which in principle can be derived from the energy levels of a molecule adsorbed onto the substrate, and the alignment of μ_t and μ_s with respect to the molecular energy levels. The latter can be parameterized in terms of the equilibrium Fermi energy level E_f and the applied voltage V_{bias}, by introducing a voltage division factor h.[1,12,36,38] This voltage division factor in turn effects the limits of integration since(equations 3.9 and 3.10):

$$m_s = E_f - heV_{bias} \tag{7.2}$$

$$m_t = E_f + (1 - h)eV_{bias} \tag{7.3}$$

The value of h is expected to be close to 0.5 when the electrostatic potential drop at the tip-molecule interface is comparable to the electrostatic potential drop at the molecule-substrate interface, similar to a break junction where the two contacts are nominally symmetric.[20]

The challenge experimentally is to control h. A hint on how to achieve this control is provided from numerical simulations of equation 7.1. For reasonable models of T(E,V), it is easy to show that departures of h from 0.5 result in a visibly asymmetric $I(V)$. This is illustrated in Figure 7.1(b) and Figure 7.1(c) where the effect of two different values of h are shown. The value of h has a dramatic

effect on the shape of the *I(V)* curve, producing a discernable asymmetry as the bias voltage changes polarity. Experimentally, by increasing the applied voltage at a fixed tunnel current, the tip withdraws from the molecule, reducing h. Thus by systematically increasing the set voltage at a fixed tunnel current, *I(V)* data as a function of h can be produced.

It should be noted that the framework discussed above provides a useful approximation for analyzing electrons tunneling through molecules with low polarizabilities, but is limited to situations in which the electric field across the molecule has a minimal effect on its conductance spectrum. Molecules with delocalized electronic structures (e.g. linear molecules with highly overlapping π orbitals) are susceptible to polarization at high voltage bias, leading to an effective decrease in η as a function of V_{bias}.[1,36,38]

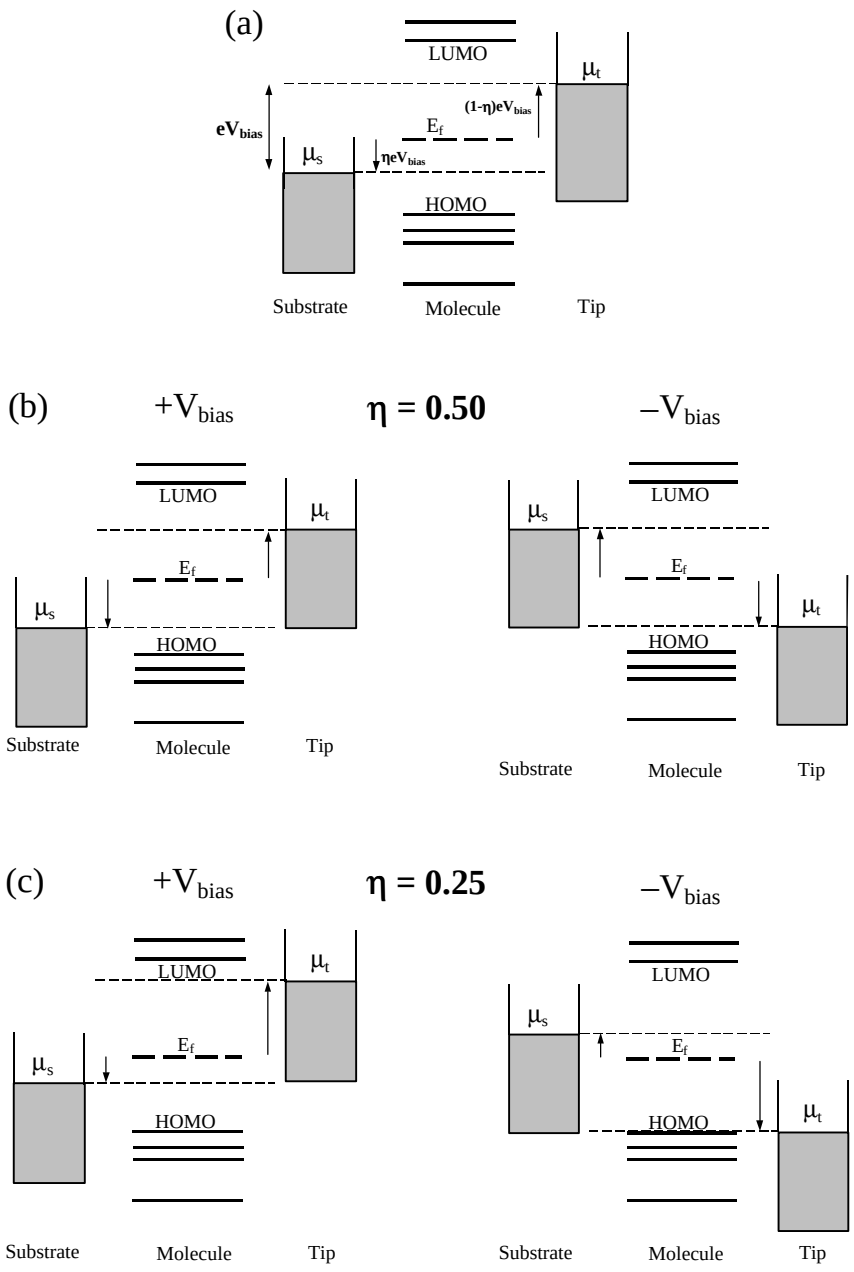

Figure 7.1

(a) Energy diagram for STS experiment showing the positions of μ_t and μ_s relative to the equilibrium Fermi energy, E_f.[1,12,36,38] The voltage division factor, η, affects the limits of integration in equation 7.1. **(b)** The situation for η=0.5. The limits of integration for $+V_{bias}$ and $-V_{bias}$ are the same; only μ_s and μ_t have interchanged positions as the bias polarity reverses. The result is the I(V) generated under these conditions are symmetric about V=0. **(c)** The situation for η=0.25. The limits of integration for $+V_{bias}$ and $-V_{bias}$ are different, resulting in a non-symmetric I(V).

A unique feature of this study is the high voltage and currents used to perform the scanning tunneling spectroscopy (STS) measurements. It has long been known that the current in an STM tunnel junction has an exponentially dependence on tip-sample separation (equation 3.2):[42]

$$I \propto e^{-2\kappa z} \tag{7.4}$$

Referring back to Chapter 5 Section 6 we examined the Z(V) behavior of an STM for a series of tunnel current values. As shown in Figure 5.17 (reshown below in Figure 7.2) for V_{set} < 2.0V the tunnel current must be less then 10pA in order to obtain a tip sample separation of 1nm or more.

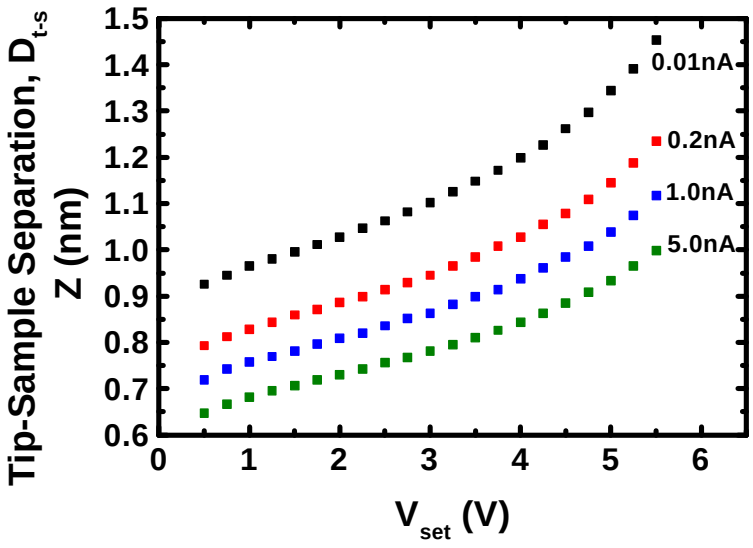

Figure 7.2

$Z(V_{set})$ simulated for Au(111) at different fixed values of I_{set}. The value of I_{set} acts as an offset and does not change the functional dependence of Z on V_{set}.

Consequently, past studies[5,6,13,108-114] on similar molecules studied herein have used tunnel currents on the order of 3 to 30pA in order to keep the tip from being buried in the molecule (see Table 7.1). Due to the low voltages used in these studies, typically $|V_{set}|$ is 0.1 to 1.2V, the energies probed lie well within the energy band gap of the molecules in question. By going to higher voltages ($|V_{bias}|$ = 2.0V to 5.0V) energy states of the molecules are accessed and increased conduction is evident.

Calculations[1,38] suggest that conduction through molecules can improve several orders of magnitude if appropriate states are accessed, typically delocalized HOMO levels. Consequently, through the use of higher voltages, significantly higher currents may be realized while still keeping the STM tip clear of the molecule.

An understanding of $D_{t\text{-}s}$ as a function of higher values of V_{set} and I_{set} is critical to my experiments because relatively higher voltages and currents (i.e. $V_{set} > 2.5V$ and $I_{set} = 200pA$) were routinely used to probe the organic films under consideration. This was in part motivated by the desire to study these molecules at voltage seen in common CMOS semiconductor devices (i.e. ± 5V). However, in order to approach the $h = 0.5$ conditions (as discussed earlier) while using higher voltages, it is then necessary to use higher currents.

Table 7.1

Set conditions (V_{set}, I_{set}) used by other research groups to study similar molecules.

Who	**Molecule**	**V_{set} (V)**	**I_{set} (pA)**
Raible et. al.[13]	RC10TS	1	17, 90
Bumm et. al.[5]	C12 alkane	1	10
Anselmetti et. al.[108]	C12 alkane	1.2	3
Delamarche et. al.[109]	C12 alkane	1.2	3
Delamarche et. al.[110]	C12 alkane	1	7
Poirier et. al.[111]	C4,6 alkane	0.3	100 - 200
	C8,10 alkane	0.3	10 - 30
Poirier et. al.[112]	C4,6,8,10 alkanes	0.1 - 0.3	10 - 100
Schönenberger et. al.[113]	C12 alkane	0.01 - 1	1 - 10
Kang et. al.[114]	C4 alkane	0.1	25 - 40
Bumm et. al.[6]	C10,12 alkane	1	10
This Study	C12, C18 alkanes and RC10TS	2.5-5.0	200

7.3 Experimental Results & Discussion

SAMs prepared from dodecanethiol (DDT), octadecanethiol (ODT) and resorcinarene C10 tetrasulfide (RC10TS) on Au(111) (see Figure 7.3) were selected for study because of their well-characterized structures and electrochemically insulative properties.[16,67,115-118] The high degree of order in alkanethiol and resorcinarene tetrasulfide SAMs has been confirmed by a number of experimental methods, including scanning tunneling microscopy.[5,6,13,66,108-114] RC10TS was prepared according to literature procedures.[119] Micron-sized domains of atomically flat Au(111) were prepared from commercial gold films evaporated onto a Cr-backed borosilicate glass substrate (Metallhandel Schroer GmbH) by heat treatment with a propane flame. Substrates were rinsed sequentially in deionized water and ethanol, and then soaked overnight in millimolar alcoholic solutions of DDT, ODT or RC10TS according to literature procedures.[64,117,118] SAMs were characterized by reflective-absorption infrared spectroscopy (RAIRS) and optical ellipsometry and were found to be consistent with values reported in the literature (1.5nm for DDT, and 2.0nm for ODT and RC10TS).[16; 115; 118] For the STS studies, immediately after preparation SAMs were transported in a vacuum desiccator and then transferred into an ultrahigh vacuum (UHV) insertion chamber operating at a pressure of 5×10^{-9} Torr.

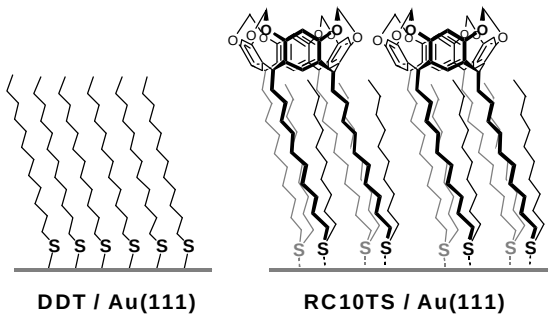

Figure 7.3

Self-assembled monolayers (SAMs) of dodecanethiol (DDT) and resorcinarene C10 tetrasulfide (RC10TS) adsorbed on Au(111) (only a few molecules are presented for clarity).The estimated thicknesses of the DDT and RC10TS SAMs are 1.5 nm and 2.0 nm, respectively.[64,115,118]

STS studies were performed on a home-built STM housed in a stainless-steel vacuum chamber operating under UHV conditions at pressures below 2×10^{-9} Torr. STS measurements of the SAMs

were conducted using mechanically cut Pt/Ir tips; measurements were repeated with two different tips in order to ensure reproducibility and to minimize any possible tip artifacts. Tip-sample distances were set using a constant tunnel current (I_{set}) at a given voltage bias (V_{set}) and maintained by a computer-controlled proportional-integral-differential (PID) feedback. High-quality images of the underlying Au grain structure could routinely be achieved with monolayers of DDT. Imaging the Au substrate through monolayers of ODT and RC10TS proved more difficult and any images obtained were often characterized by tip switching that would occur randomly throughout the image, indicative of a lower conductance for RC10TS. Conductance spectra were derived from averaged I(V) curves at different set point voltages; measurements comprised of 20 scans per set point voltage over a two-second interval were repeated at several locations across the SAM to ensure reproducibility. First-order derivatives (dI/dV) were obtained by performing a point-to-point sliding average of the I(V) data. I/V normalized by G_0, the quantum of conductance, were generated directly from the I(V) data. The noise level of the instrument corresponds to $(I/V)/G_0 = 1.0 \times 10^{-8}$.

The conductance spectra are presumed to represent tunneling through a single or small number of molecules within a SAM. Conductance across a single (or small number of) molecule(s) is strongly favored for several reasons:

(i) The molecular orbital nodes within a single molecule offer the most efficient electronic path between tip and substrate.

(ii) There is no evidence for orbital overlap or charge-transfer mechanisms between adjacent molecules.

(iii) The lateral tip drift within the timescale of the measurement is estimated to be much less than the molecular cross section ($\geq$ 0.2 nm).

(iv) Evidence provided by Reinhoudt and co-workers (in the case of RC10TS) suggest a nearly normal orientation to the Au(111) surface,[118] such that the most direct link between tip and substrate is defined by the molecule itself.

In order to meaningfully interpret the *I(V)* data as a function of applied voltage bias, it is important to define the set point voltage at which the I(V) data becomes relatively symmetric, i.e. when $h \sim 0.5$. This corresponds to the molecular equivalent of a symmetric tunnel junction, in which the electrostatic coupling between molecule and substrate is nominally equal to that between molecule

and tip.[4] As introduced in Chapter 4, based upon the studies we have performed where molecules were systematically probed for a series of V_{set} values (see Chapters 6, 7 and 8), we believe that the condition where $h \sim 0.5$ is attained at a characteristic set point voltage for a fixed value of tunnel current. This characteristic voltage is referred to as "critical V_{set}" and is marked by the transition between stable and unstable feedback, the latter characterized by high levels of noise in the z-piezo feedback voltage. At this time, it is an unsettled question whether the tip actually becomes embedded in the SAM or whether the electric field between the tip and upper surface of the SAM becomes so great as to produce instability in the tunneling current. For a set current of 0.2nA, this transition occurs roughly at a set point voltage of 2.5 V for DDT, 3.5V for ODT, and 4.0V for RC10TS. It is important to note that the I(V) data systematically become more symmetric as the applied set voltage approaches this characteristic set point voltage (see Figure 7.4, Figure 7.5 and Figure 7.6), confirming the model above.

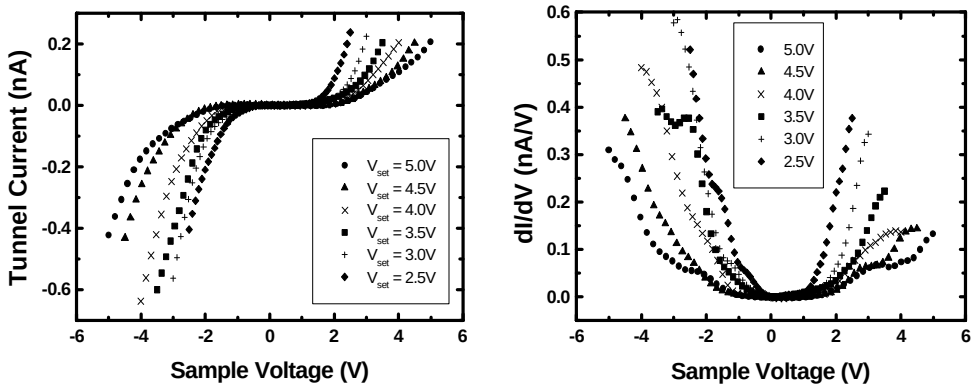

Figure 7.4

(*left*) *I(V)* data for DDT for a series of set voltages and a set current of 0.2 nA. (*right*) *dI/dV* data for DDT for a series of positive set voltages and a set current of 0.2 nA. The most symmetric *dI/dV* data is observed at a set voltage of 2.5 V. For set point voltages below 2.5 V, topographic images become noisy, indicating that the tip is buried in the SAM.

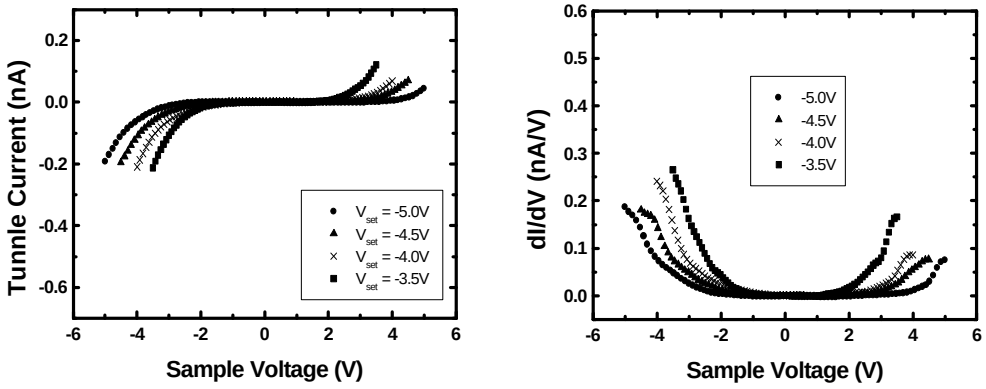

Figure 7.5

(*left*) *I(V)* data for ODT for a series of set voltages and a set current of 0.2 nA. (*right*) *dI/dV* data for ODT for a series of negative set voltages and a set current of 0.2 nA. The most symmetric *dI/dV* data is observed at a set voltage of 3.5 V. For set point voltages below 3.5 V, topographic images become noisy, indicating that the tip is buried in the SAM.

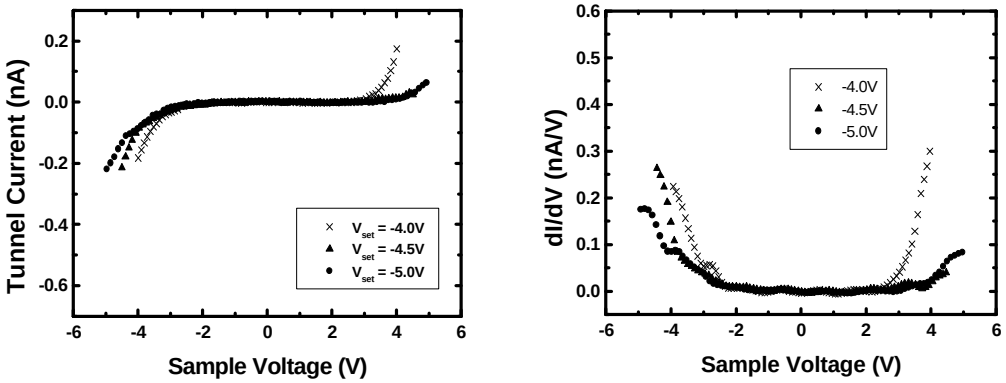

Figure 7.6

(*left*) *I(V)* data for RC10TS for a series of set voltages and a set current of 0.2 nA. (*right*) *dI/dV* data for RC10TS for a series of negative set voltages and a set current of 0.2nA. The most symmetric *dI/dV* data is observed at a set voltage of 4.0 V. For set point voltages below 4.0 V, topographic images become noisy, indicating that the tip is buried in the SAM.

The *I(V)* data obtained on SAMs of DDT, ODT and RC10TS yield dramatic differences in their electrical conductivities. Analysis of the conductance spectra indicates that the *I(V)* curves are

reasonably symmetric at the characteristic set point voltage defined by h = 0.5 but become more asymmetric as the separation increases, in accord with the model discussed above. The gap in conductance for DDT can be determined straightforwardly from the *dI/dV* data at the characteristic set voltage of 2.5 V. We estimate this gap to be 1.5 ± 0.5 eV. The E_f - HOMO energy difference is simply one-fourth of the conductance gap when η= 0.5,[1,36,38] which gives 0.4 ± 0.2 eV for DDT. The *I(V)* curves and conductance spectra of ODT are similar to those of DDT but lose their symmetry more rapidly at higher set voltages (see Figure 7.5). The estimated conductance gap and E_f - HOMO separation for ODT is 4.0 ± 0.5 eV and 1.0 ± 0.2 eV respectively, nearly than 2.7 times larger than that of DDT. The estimated conductance gap and E_f - HOMO separation for RC10TS is 5.5 ± 0.5 eV and 1.4 ± 0.2 eV respectively, nearly four times larger than that of DDT. (see Table 9.1 for summary)

Table 7.2

Summary of measured values from SAMs

Molecule	**Conduction Gap**	**E_f - E_{Homo}**	**$(I/V)/G_0$ $\|_{V=-1.5V}$**	**V/I $\|_{V=-1.5V}$**
DDT	1.5 ± 0.5 V	0.4 ± 0.2 eV	7.9×10^{-7}	1.6×10^{10} Ω
ODT	4.0 ± 0.5 V	1.0 ± 0.2 eV	4.1×10^{-8}	3.2×10^{11} Ω
RC10TS	5.5 ± 0.5 V	1.4 ± 0.2 eV	1.0×10^{-8}	1.3×10^{12} Ω

The relative increase in the E_f -HOMO separation for RC10TS on Au(111) compared to ODT on Au(111) has important implications for their insulating properties. Molecular resistance values can be estimated at small tip-molecule separations when the conductance at zero bias is dominated by the molecular conductance rather than the tunnel gap conductance. The tunneling junction resistance at zero bias can be expressed simply as:

$$R(V=0) = \frac{1}{\left(\partial I / \partial V\right)} \qquad 7.4$$

The noise level in the I(V) data (~ 1pA) prevents a straightforward evaluation of equation 7.4. The best we can do is to compare the normalized conductivity (i.e. $[I/V]/G_0$) of the three molecules at a given voltage. To minimize the effects of the tip-molecule gap, this evaluation was done for each molecule on data taken near the $\eta = 0.5$ condition. Also, to obtain an estimate as close to zero bias as possible, we chose the lowest bias that would allow a common comparison above the noise level for all three molecules. The results are $[I/V]/G_0|_{V=-1.5V}$ is equal to 7.9×10^{-7} G_0 for DDT, 4.1×10^{-8} G_0 for ODT and 1.0×10^{-8} G_0 for RC10TS (see Figure 7.7).

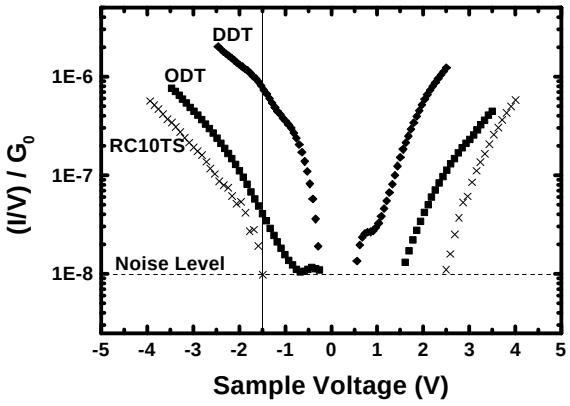

Figure 7.7

Plots $(I/V)/G_0$ generated from the $\eta = 0.5$ data for each molecule (i.e. $V_{set} = 2.5V$ for DDT, $V_{set} = -3.5V$ for ODT, $V_{set} = -4.0V$ for RC10TS). Using the $\eta = 0.5$ data minimizes the effect of the tip-molecule gap on the conductivity data. The low values shown are indicative of highly insulating molecular films of each molecule. The limiting noise level of $(I/V)/G_0 = 1.0 \times 10^{-8}$ results in resistances of on the order of 100s up to 1000 GΩ depending on voltage. For the purposes of comparison, values $(I/V)/G_0$ are evaluated at $V_{bias} = -1.5V$ and are tabulated in Table 9.1.

Not surprisingly, as one would predict from equation 4, we see slightly more than an order of magnitude difference in $[I/V]/G_0$ between DDT and ODT. The static resistance scales in a similar fashion. What is more interesting is the factor of four difference between ODT and RC10TS where RC10TS exhibits less conductivity than ODT. This is especially surprising given that RC10TS is bonded to the Au substrate via four sulfide bonds. Additionally, the resistance of the RC10TS

monolayer is already on the order of 1000 GΩ at -1.5V implying that a reasonable estimate of the zero-bias resistance of RC10TS is at least 1000GΩ. Similarly, both DDT and ODT drop below $[I/V]/G_0 = 1.0 \times 10^{-8}$ level as V_{bias} 0V , indicating that these films are also highly resistive and may have zero bias resistance values on the order of 100s of GΩs. These resistance values are several orders of magnitude greater than those of relatively conductive molecules such as xylyl dithiol or the oligophenylene dithiols, whose resistances have been determined theoretically and in some cases experimentally.[4,17, 32]

What is responsible for the very high resistance of the RC10TS molecule? ODT and RC10TS are of similar length. One significant factor is the strength of chemical bonding to the Au(111) surface. Individual Au-sulfide ($Au-SR_2$) interactions are substantially weaker than Au-thiol (Au-HSR) or Au-thiolate (Au-SR) interactions, implying that the electronic energy levels of the sulfide are less polarized by adsorption. A careful examination of various organosulfur adsorbates on Au(111) by X-ray photoelectron spectroscopy (XPS) demonstrated that the S(2p) binding energies of sulfides are hardly affected by adsorption onto gold, whereas those of thiols and disulfides are shifted by 1 eV or more upon binding.[120] Therefore, the molecular orbitals of ODT are likely to experience large perturbations in their energy levels and subsequently greater overlap with the gold substrate, while the higher resistance for RC10TS correlates with the weak electronic coupling of the sulfide orbitals to the metal surface.

Based on these estimates of molecular conductivity, we can estimate the leakage current density through insulating SAMs on Au(111) and compare them to theoretical estimates of the leakage current through thin SiO_2 layers on Si.[103] Assuming once again that the electrical conductances measured above are representative of single molecules, it follows that the leakage current density *J(V)* through a molecular SAM can be expressed as:

$$J(V) \cong VG(V)/(\pi r^2) \qquad 7.5$$

where *G(V)* is the conductance approximated from the *I(V)* data for which $h \sim 0.5$ and *r* is the effective radius of the molecular "wire" conducting the flow of electrons. The latter quantity cannot be precisely determined, but can be assigned an upper limit based on the molecular periodicities of the SAMs. Thus we infer that $r_{DDT} = 0.21$ nm and $r_{RC10TS} = 0.6$ nm, as determined from previous structural studies.[13,60,61]

A semilogarithmic plot of $J(V)$ for the 1.5-nm DDT SAM and the 2.0-nm RC10TS SAM reveals the superior insulating properties of the latter at higher voltages (see Figure 7.8). SiO_2 layers with comparable leakage current densities were calculated to have thicknesses of 1.0 nm and 1.5 nm SiO_2, respectively.[103] Although this comparison is semi-quantitative at best, it strongly suggests that organic SAMs indeed have the potential to provide the necessary insulation for the efficient operation of nanoscale electronic circuits. The ease of fabricating high-quality molecular SAMs over relatively large areas may provide a viable approach for producing insulative ultrathin films for future device applications.

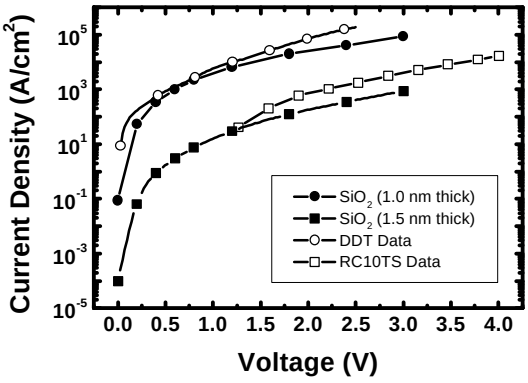

Figure 7.8

J-V plots comparing voltage-dependent leakage current through DDT on Au and RC10TS on Au with 1.0 nm and 1.5 nm SiO_2 layers on Si, as calculated in Ref. 103.

7.4 Summary

We have demonstrated that the resistances of highly insulative SAMs can be estimated using systematic STS to obtain conductance spectra over a range of set point voltages. Estimates for the zero-bias resistance in SAMs RC10TS on Au(111) are essentially that of a single molecule; analysis of the *I(V)* data gives a zero-bias resistance over 1000 GΩ for RC10TS. The conductance gap for these three SAMs is 1.5 ± 0.5 eV, 4.0 ± 0.5 eV and 5.5 ± 0.5 eV, respectively. The effective leakage current density across the RC10TS SAM on Au(111) is particularly low, and its electrical resistance is comparable to a 1.5-nm layer of SiO_2 on Si.

8. STS MEASUREMENTS ON ALKANE-ESTERS

8.1 Background

In Chapter 6 it was demonstrated that the conductance of a molecules could be significantly altered through the use of a chemical doping event, the formation of a charge-transfer complex. Hong, et. al.[12] and myself (Chapter 7) demonstrated that changing the nature of the interface between molecules and the metal probe contacts has significant effects on molecular conduction. Naturally these discoveries lead to the question: "Can the conductivity of a molecule be altered through an internal change or variation?" To test this, Elwyn Shelly working under the direction of Professor Preece (Haworth School of Chemistry, University of Birmingham, U.K.) synthesized two new molecules (see Appendix C for summary of the synthesis) consisting of an alkane chain with an ester group located in the center of the chain (see Figure 8.1). An ester is the product of the reaction between an organic acid and an alcohol [56]; the general formula for an ester is shown schematically in Figure 8.1. The difference between alkane-ester+ and alkane-ester- is the orientation of the ester group within the alkane chain. SAMs of both alkane-esters were formed and probed with STS.

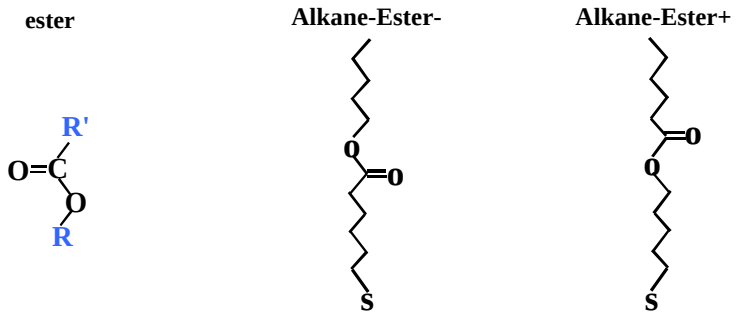

Figure 8.1

Schematics of an ester and of the two molecules under investigation: Alkane-Ester- and Alkane-Ester+. R and R' groups on the ester indicate the presence of additional organic components to which the ester is attached. The difference between Alkane-Ester- and Alkane-Ester+ is the orientation of the ester group within the alkane chain.

8.2 STM Data

Figure 8.2 and Figure 8.3 summarize the I(V) and dI/dV data respectively for both molecules. Two differences between alkane-ester+ and alkane-ester- are readily apparent from the I(V) data: (i) The η=0.5 condition occurs 0.5V lower for alkane-ester- than for alkane-ester+. This indicates a smaller conduction gap and separation between the Fermi and HOMO levels for alkane-ester- as compared to alkane-ester+ (see Table 8.1). (ii) Alkane-ester+ and alkane-ester- have opposite behaviors for large positive values of V_{bias} where V_{set} is above the η=0.5 condition. For V_{set} > 2.5V alkane-ester- shows reduced current for large positive voltages relative to negative voltages. For V_{set} > 3.0V alkane-ester+ shows increased current for large positive voltages relative to negative voltages.

Table 8.1

Summary of measured values from SAMs

	Conduction Gap	**E_f - HOMO**
Alkane-Ester -	0.8 ± 0.5 V	0.2 ± 0.2
Alkane-Ester+	1.2 ± 0.5 V	0.3 ± 0.2

The behavior of alkane-ester- is similar to that of other alkane chain molecules (see Figure 7.3 and Figure 7.4) in that it shows "suppressed" current flow for positive bias relative to negative biases. The transition to the $\eta = 0.5$ condition occurs at $V_{set} = -2.5V$, the same V_{set} magnitude where the $\eta = 0.5$ occurs for DDT; both molecules are nominally the same height. The most notable difference between alkane-ester- and the other alkane chains is the abrupt change in the shape of the I(V) between the $\eta = 0.5$ condition and higher set voltages. For the alkane chains, the change in the asymmetry occurs slowly. Additionally, the dI/dV from alkane-ester- shows far more symmetry when $\eta = 0.5$ then for the alkane chains.

Alkane-ester+ shows the gradual change in the asymmetry that is exhibited by ODT and DDT. However, instead of a decrease in current magnitude for positive V_{bias} as a V_{set} increases, alkane-ester+ shows increased current flow for positive V_{bias}; presumably this is due to the accessing of LUMO levels or some mechanical deformation of the molecule. The opposite behaviors of alkane-ester- and alkane-ester+ clearly demonstrate that small internal changes within a molecule can result in significant changes in electrical conduction. In the next section, some possible explanations are presented.

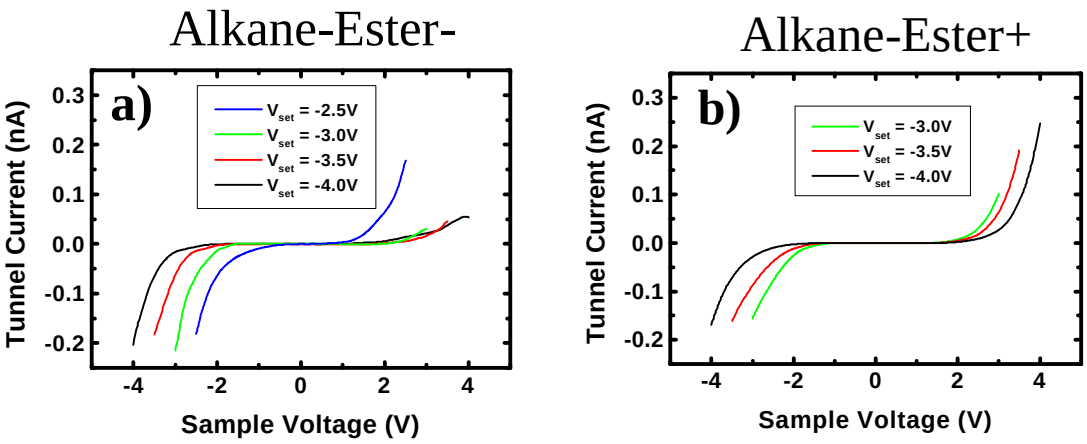

Figure 8.2

a) I(V) data for Alkane-Ester-. As V_{set} is increased above |2.5V|, the current for high positive bias voltages is suppressed relative to negative bias voltages. **b)** I(V) data for Alkane-Ester+. As V_{set} is increased above |3.0V|, the current for high positive bias voltages increases relative to negative bias voltages

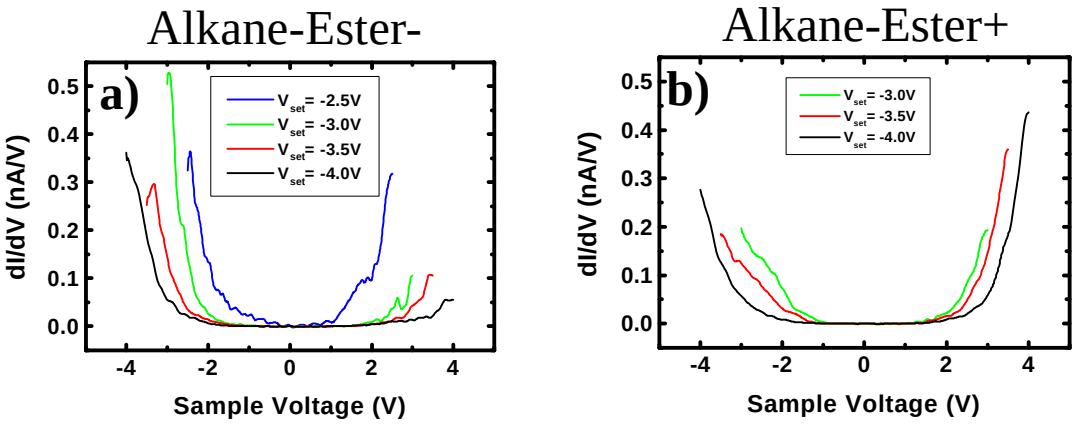

Figure 8.3

a) dI/dV data for Alkane-Ester-. **b)** dI/dV data for Alkane-Ester+. For both molecules, the dI/dV at the $\eta = 0.5$ condition are remarkably symmetric in comparison to other alkane-chains (see Figure 7.3 and Figure 7.4)

8.3 Explanations

Several possible explanations for the behavior of the alkane-esters have been proposed and are summarized here. The first proposed explanation resorts to methods previously used[1,36,38] where T(E) of the molecule is calculated through the use of theoretical models. The second proposed explanation considers the effects of an electrostatic dipole layer on current flow. As will be shown, a combination of these two approaches results in relatively good fits to the data.

8.3.1 Changing T(E)

Like a particle in a box, it is hypothesized that small changes to the geometry of a molecule can result to significant changes to the molecular energy states. To test the feasibility of this explanation, transmission functions, T(E), were calculated for both molecules using programs available on the Purdue Nanoelectronics HUB (http://punch.ecn.purdue.edu) and based on known theories[1,34,36,38].

Figure 8.4 a) and b) shows the results of the HUB calculations for alkane-ester- and alkane-ester+ respectively. Immediately, we see the emergence of LUMO levels on the alkane-ester+; this is consistent with increased conduction for positive bias voltages. However, the transmission probability of theses LUMO states is four orders of magnitude below the HOMO making symmetric or significantly increased conduction for positive bias voltages unlikely at best.

The HUB calculations demonstrates that orientation of the ester group does in fact alter the energy states of the alkane-ester molecule. The change appears to be insufficient to account for the corresponding change in the I(V) data. This result may be a function of the calculation used; a more progressive model such as the one used on TMXYL-TCNE (see Chapter 6 and reference 99) may provide an explanation that is more consistent with the experimental results.

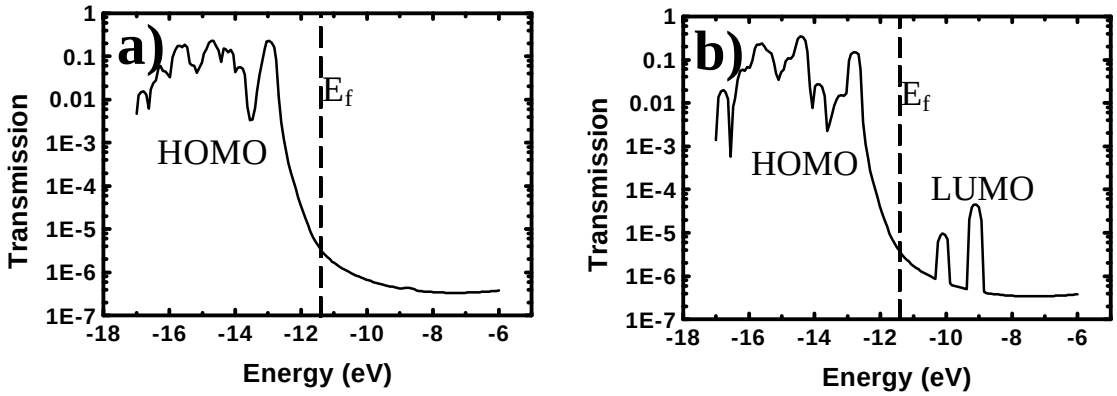

Figure 8.4

a) Transmission function, T(E), for alkane-ester-. The presence of a LUMO level is not detected. **b)** Transmission function, T(E), for alkane-ester+. The emergence of two LUMO level is evident.

8.3.2 Alkane-esters and Dipoles

Associated with the ester is an electric dipole resulting from the chemical bonding (see Figure 8.5). The SP2 bond between the exterior oxygen and the ester carbon is highly ionic in nature resulting in a strong dipole indicated by the red arrow. The P-orbitals of the two oxygens and the ester carbon form a conjugated π system, but the strong electron acceptor nature of the O=C bond causes the interior oxygen to obtain a slightly positive charge resulting in a small component of the dipole to be along the molecular axis. Additionally, the sulfur-gold thiol bond has a dipole associated with it. When the S-Au bond forms, a fractional electron is transferred from the S atom to the Au substrate; the result is an electric dipole moment pointing from the Au to the S. The net dipole of the system is a superposition of these two dipoles and may be effected by the detailed configuration of each molecule.

Model calculations on each molecule were performed by Steve Tripp (Dept. of Chemistry, Purdue U.) and myself using HyperChem.[121] The programs available to us are incapable of properly modeling an Au surface or atom. Consequently, the molecules were modeled with a hydrogen taking the place of the Au. Although this is not an accurate representation of the molecule in a SAM, it is my hope that the resulting calculations capture the essence of the system. The results of the calculations are shown in Figure 8.6.

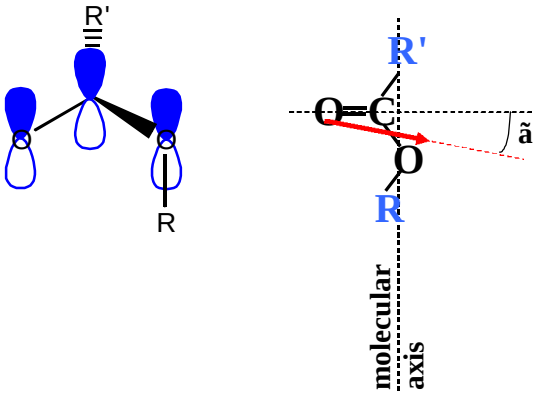

Figure 8.5

Associated with the ester group is an electric dipole moment. The primary component of this dipole is oriented perpendicular to the molecule axis. A comparatively small component of the dipole is oriented along the molecular axis; this component of the dipole changes orientation with the ester group. The dipole results from the highly ionic nature of the O=C bond combined with the conjugation of the π-orbitals of the three atoms comprising the ester group.

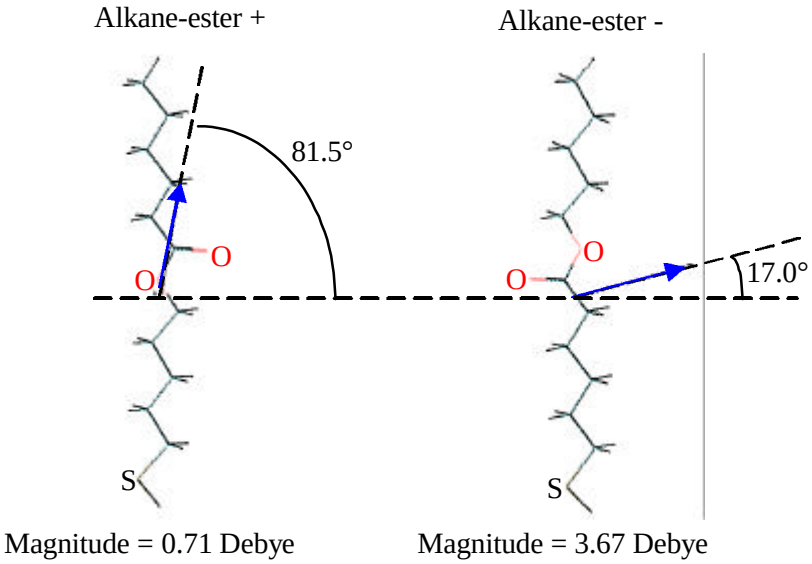

Figure 8.6

Based on a HyperChem[121] models the dipole moments for alkane-ester+ and alkane-ester- were calculated (special thanks to Steve Tripp, Dept. of Chemistry, Purdue U for his help). In this model, single molecules not bonded to a substrate were used.

The difficulty with this picture is that alkane chains have been shown to form SAMs with the molecular axis at a 32° angle relative to the surface normal.[109] The question then arises: "Are the alkane-esters tilted? And, if so, how much?" However, for the purposes of a thought experiment, let us assume that the alkane-ester behave in a manner similar to alkane chains and are tilted at 32° when they form a SAM on Au (111) as shown in Figure 8.7. The direction of the 32° tilt was chosen so that the SP3 "zigzag" of the alkane chain immediately above the sulfur atom is preserved.

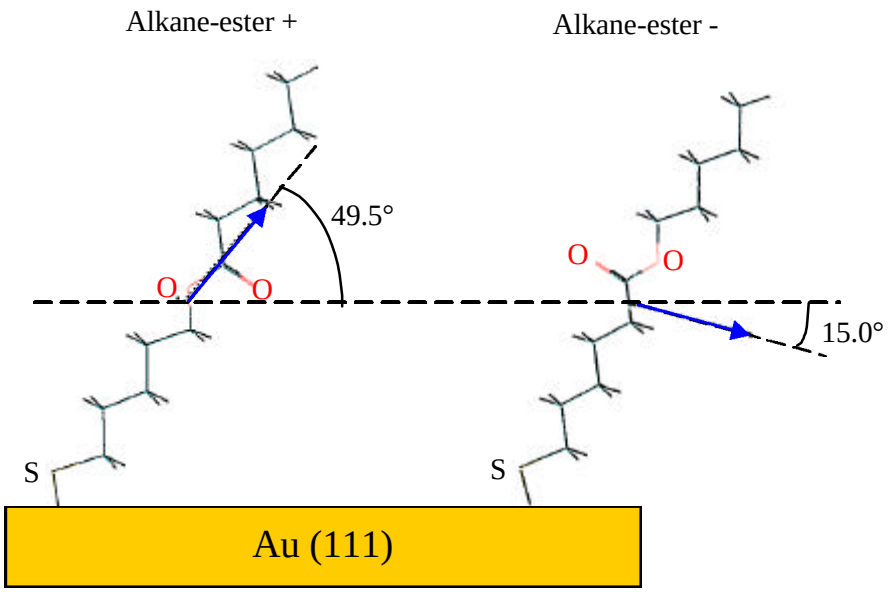

Figure 8.7

The same calculations as shown in Figure 8.6 but with a 32° tilt added to the orientation of the molecule relative to the vertical.

The inclusion of the 32° tilt in the molecule orientation significantly changes the orientation of the molecular dipole moments. Table 8.2 summarizes the information on the dipole moments for both molecules in the tilted configuration. From Table 8.2 we see a number of differences between the dipole moments of the two molecules: i) The total dipole moment of alkane-ester- is four times greater than the total dipole moment of alkane-ester+. ii) The vertical components of alkane-ester- and

alkane-ester+ are oriented in opposite directions. iii) The horizontal component of alkane-ester- is over seven times larger than horizontal component of alkane-ester+.

Table 8.2

Summary information about the dipole moments present in alkane-ester- and alkane-ester+ based upon the model described above (see Figure 8.7). (D = 1 Debye = 3.336 x 10^{-30} C·m).

	Alkane-ester-	**Alkane-ester+**
horizontal component	3.54 D	0.46 D
vertical component	-0.95 D	0.54 D
magnitude	3.67 D	0.71 D
angle above horizontal	-15°	+49.5°

8.3.3 Electrostatic Dipole Layer

An electrostatic dipole layer in an organic film establishes a fixed surface potential (V_{dip}) on the sample and is given by:[65]

$$V_{dip} = N_p p / 2\varepsilon \qquad 8.1$$

where N_p is the density of dipoles per unit area and **p** is the strength of the vertical component of dipole moments. Using typical parameters, $N_p = 4.46 \times 10^{18}$ molecules/meter, [122] dielectric constant = 2.25, we can calculate V_{dip} for both molecules: $V_{dip} = -0.32V$ for alkane-ester- and $V_{dip} = 0.18V$ for alkane-ester+; a total difference of: $\Delta V_{dip} = 0.5V$.

The question is: "what does this do to the I(V)?" To answer this question, let us consider the thought experiment depicted in Figure 8.8. In Figure 8.8 we compare a molecular SAM with and without a surface dipole layer. Experimentally we cannot "turn on" and "turn off" the dipole within the molecule, however, it is instructive to consider the effects of such an action on the I(V).

We start with a molecular SAM which does not have a dipole moment as shown in Figure 8.8 top; an I(V) is taken as shown by the blue line. With no surface dipole, the potential drop across the molecule, V_{mol}, and the actual applied bias, V_{bias}, equal each other. Now if a positive dipole moment is turned on, a net positive surface potential, V_d, develops in the SAM as shown in Figure 8.8 middle.

The result is that the potential drop across the molecule is shifted (to the left) relative to the applied bias. Since the feedback is on and a negative set voltage is used to maintain the feedback, the tip must move closer to the sample in order to maintain the desired tunnel current. Notice that for negative bias voltages, $|V_{mol}| < |V_{bias}|$. For our purposes, we wish to compare I(V) data with the tip at the same height above the SAM. To return the tip to its original height (i.e. its height before the dipole was turned on) we must increase $|V_{bias}|$ by the $|V_d|$ as shown in Figure 8.8 bottom. Now we take an I(V) and we note two changes in the I(V): i) the value of V_{set} is shifted more negative, and ii) since $|V_{mol}| > |V_{bias}|$ for positive values of V_{bias} we get additional current flow for large positive values of V_{bias}.

Repeating the same thought experiment for a negative surface dipole moment (see Figure 8.9), we find that the I(V) behaves in exactly the opposite manner: i) the value of V_{set} is shifted more positive, and ii) since $|V_{mol}| < |V_{bias}|$ for positive values of V_{bias} we get less current flow for large positive values of V_{bias}.

Finally, in Figure 8.10 we compare I(V) data taken with V_{set} one volt above the $\eta = 0.5$ condition on alkane-ester+ and alkane-ester- respectively. We see that $\Delta V_{set} = 0.5V = \Delta V_{dip}$ and the direction of the change is predicted by our model (i.e. Vset shifted more negative for + dipole and more positive for a – dipole). Additionally, as predicted by the model, the I(V) for the alkane-ester+ shows increased current flow for large positive V_{bias} and the alkane-ester- shows decreased current flow for large positive V_{bias}.

When V_d is +

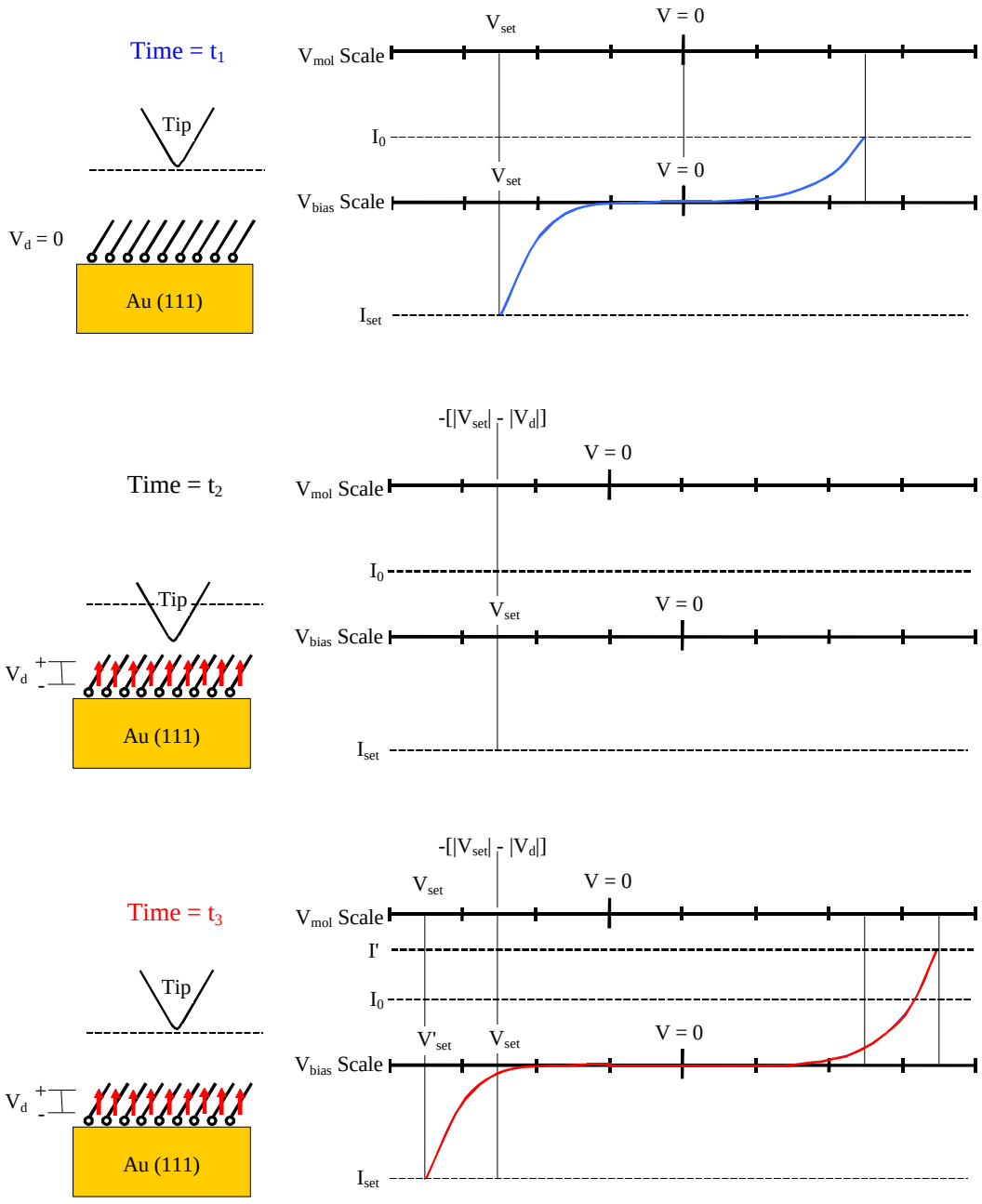

Figure 8.8

Behavior of the I(V) resulting from a positive surface dipole layer.

When V_d is -

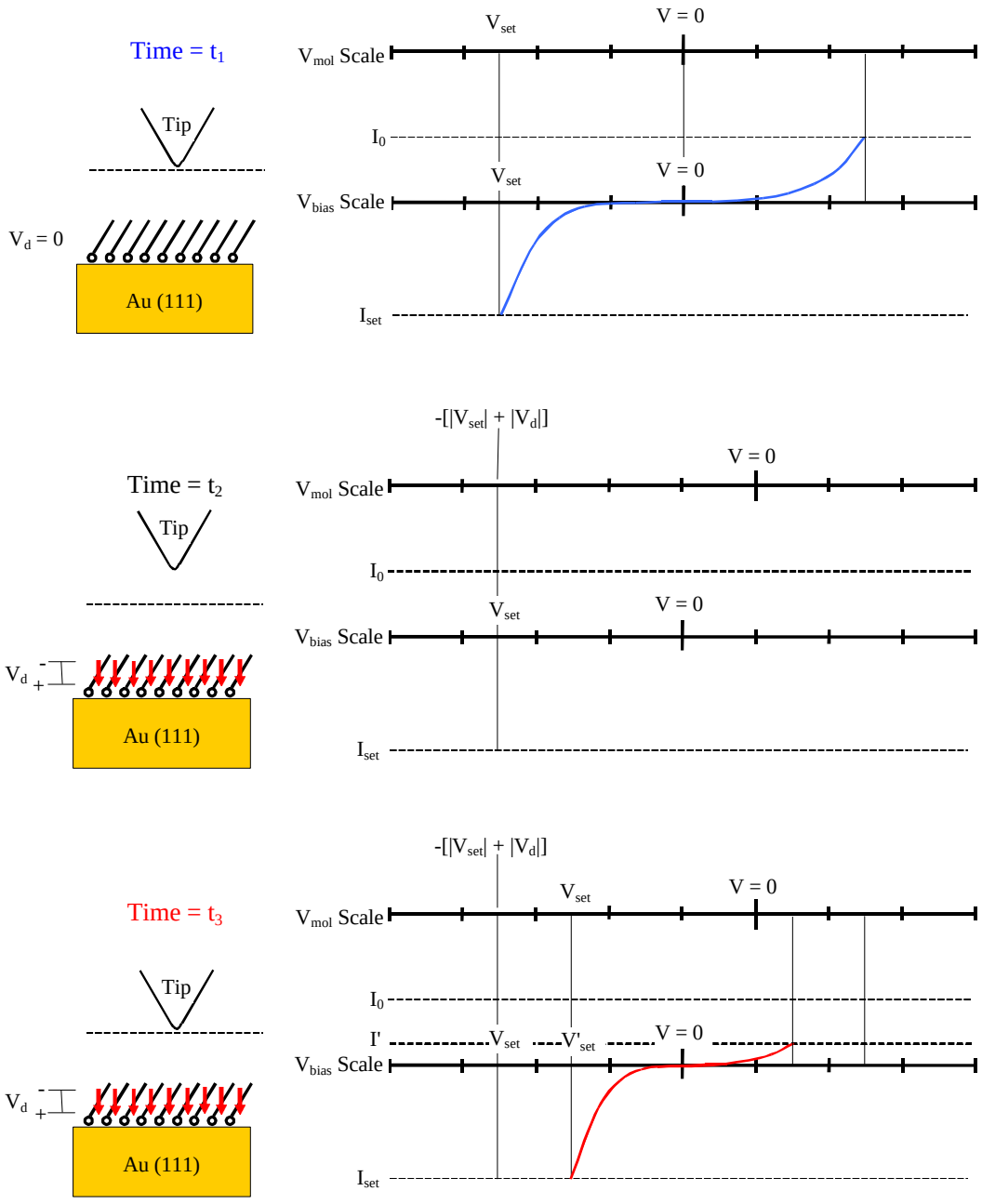

Figure 8.9

Behavior of the I(V) resulting from a negative surface dipole layer.

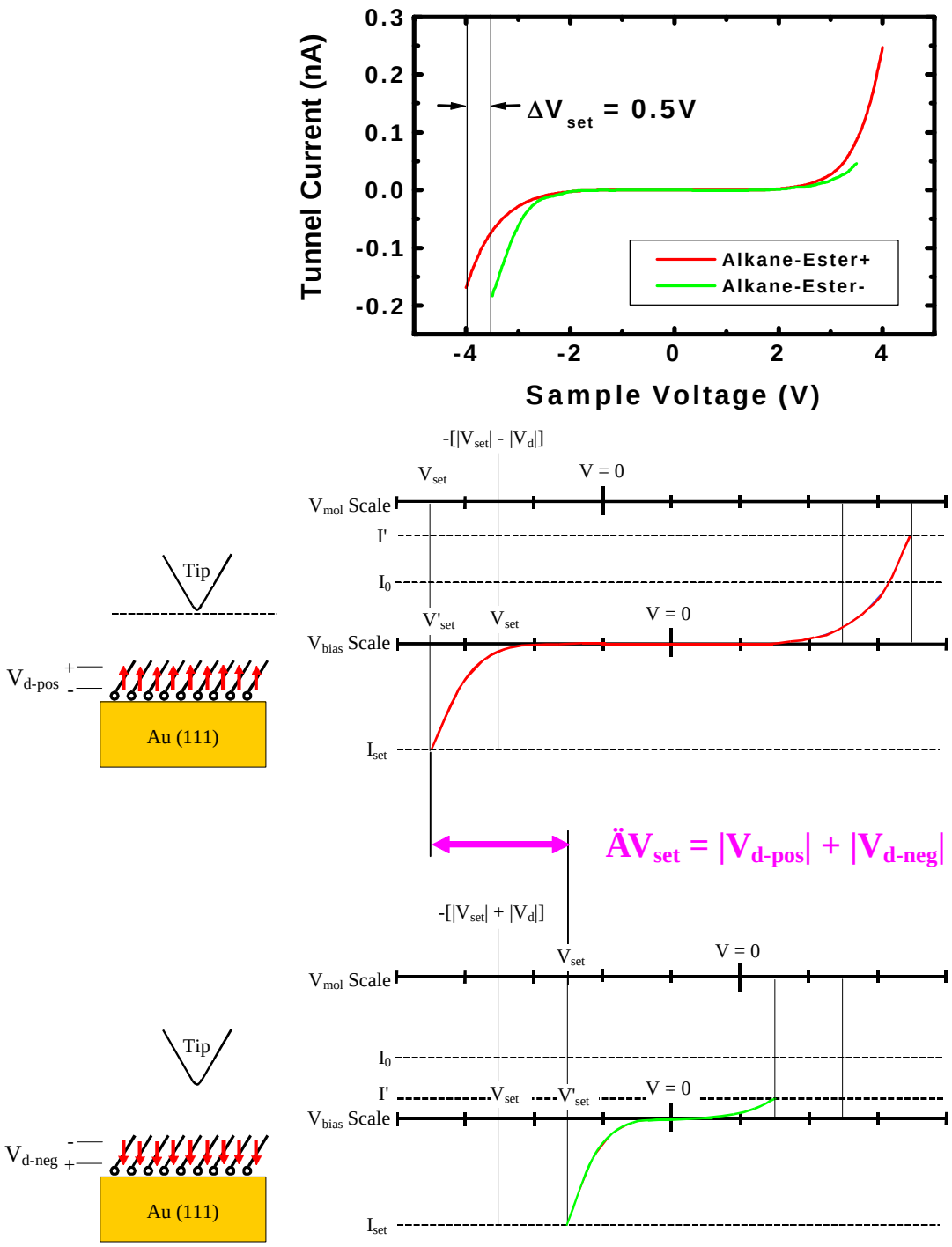

Figure 8.10

Comparison of I(V) data (top) to the predictions of the model (center and bottom).

Our dipole model (Figure 8.8, Figure 8.9 and Figure 8.10) was combined with the transmissions functions shown in Figure 8.4 and I(V) was calculated for both alkane-ester+ and alkane-ester-. The results are shown in Figure 8.11. Clearly the model accurately predicts the effects of a surface dipole layer on I(V) data taken with STS. Furthermore, the fits to the actual data are in relatively good agreement but more accurate calculations of T(E) and I(V) are in order.

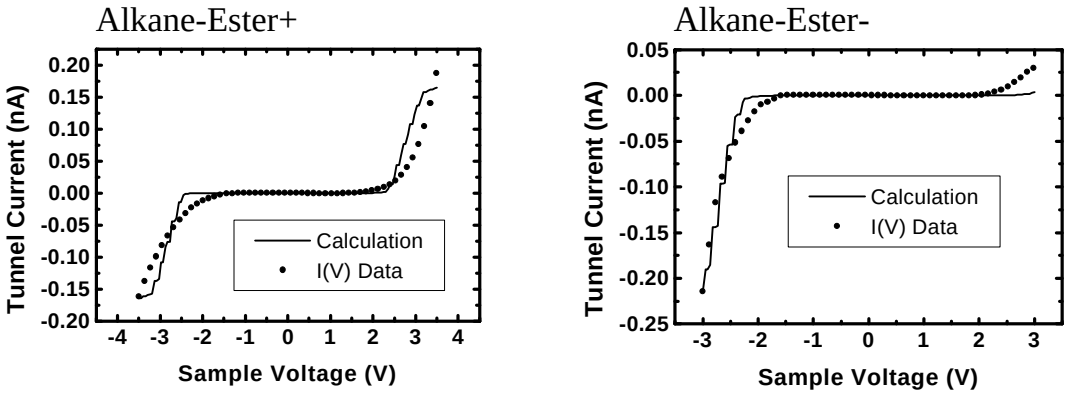

Figure 8.11

Comparison of I(V) data for alkane-ester+ and alkane-ester- to model calculations based on T(E) given in Figure 8.4. An overall normalizing constant was required because the details of the tip-molecule coupling are not known.

8.3.4 Deforming the Molecule Using Dipoles

Another proposed explanation of the data proposed that the presence of the ester dipole in an electric field may account for the differences between alkane-ester- and alkane-ester+ through mechanical deformation of the molecules. In considering this explanation, we may ignore the vertical components of the dipoles since they are oriented parallel to the external electric field resulting from V_{bias}. In the external electric field, the dipoles attempt to rotate and align themselves to the external electric field, thus applying a torque ($\boldsymbol{\tau} = \mathbf{p} \times \mathbf{E}$) to the center of the flexible alkane chains. Clearly, the dipole in the alkane-ester- experiences a torque over seven times greater that the torque experience by the alkane-ester+ dipole.

Additionally, the heights of the two molecules are changed when a torque is applied to the ester dipole. For both molecules we see that the molecule will tend to increase in height for a positive voltage bias applied to the substrate, $+V^{bias}$, and decrease in height for a negative voltage bias, $-V_{bias}$. The hypothesis is that this deformation accounts for the differences in the conduction of the two molecules. The increased conduction may be realized in a number of ways:

i) one of the alkane-esters may be pulled into or pushed out of contact with the STM tip,

ii) the energy states of the alkane-esters may be significantly altered as a result of its mechanical deformation. (consider a particle in a box when the dimensions of the box are changed).

8.4 Conclusions

The significance of the alkane-ester results is the demonstration that a small change to the internal structure of a molecule may significantly impact its electrical conduction. All three proposed explanations of the I(V) data show some promise; however, the electrostatic dipole model is particularly simple and seems most promising. The electrostatic dipole model can be greatly improved if combined with calculations of T(E) so that theoretical fits to the I(V) can be calculated.

9. SUMMARY & CONCLUSIONS

9.1 Ways to Change the Conductivity of a Molecule

In the introduction, data were presented which showed that changing the endgroups of a molecule changes the conduction properties of that molecule.[12] In the work presented herein, it was demonstrated that the conduction of a molecule can be changed in several other ways:

- Changing the morphology of the molecule on the surface.

  In Chapter 6 it was shown that changing TMXYL from an "upright" to a "flat" orientation relative to the Au substrate resulted in an order-of-magnitude change in the conductivity of the molecule (see Figure 6.10)

- A chemical doping event.

  In Chapter 6 it was shown that the "flat" orientation of TMXYL could be changed from a relatively insulating or at most, semiconducting behavior to a conducting behavior through the formation of a charge transfer (CT) complex with TCNE (see Figures 6.6, 6.7 and 6.8).

- Altering the orientation of a small internal component of a molecule.
  In Chapter 8 it was shown that changing the orientation of the ester group situated in the center of an alkane chain, drastically change the behavior of the alkane-ester for large positive bias voltages (see Figure 8.2). This is a particularly remarkable result since the position of only 2 of 32 atoms in the molecule were switched (see Figure 8.3).

It has now been experimentally shown that the conduction of a molecule may be controllably altered by four different methods: 1) altering endgroups, 2) altering orientation, 3) chemical doping, and 4) altering the orientation of an internal element of the molecule. Such basic proof-of-concept experiments are necessary to the advancement of molecular electronics and demonstrate that the designer of molecular electronic circuits has numerous options with just a small set of molecules.

9.2 Measured Values

It has been demonstrated that organic molecules exhibit conducting (TMXYL-TCNE), semiconducting (TMXYL-Flat) and insulating (Alkanethiols, Alkane-Esters, Resorcinarene) behavior. Also, several quantities have been measured for each molecule: conduction gap, E_f - HOMO, "critical V_{set}" (as defined in Ch4 and Ch7) and I_{set}; this information is summarized in Table 9.1. It should be noted that the values of "critical V_{set}" listed in Table 9.1 are associated with the particular value I_{set} also listed. These two values are linked through the feedback system of the STM; the value of "critical V_{set}" will change for different values of I_{set} in a manner as described in Table 9.2. The magnitude of I_{set} listed in Table 9.1 is an indication of the relative conductivity between the molecules; higher values of I_{set} indicate greater conductivity. Additionally, for any given value of I_{set}, the value of "critical V_{set}" further differentiates the relative conductivity of the molecules; lower values of "critical V_{set}" indicate greater conductivity. Thus, TMXYL-TCNE with the lowest "critical V_{set}" and highest I_{set} (and no conduction gap) is the most conducting molecule listed in Table 9.1. Conversely, RC10TS with the highest "critical V_{set}" and lowest I_{set} (and largest conduction gap) is the most insulating molecule listed.

Table 9.1

Summary of the quantitative values measured on a number of organic molecules. The molecules listed show a range of behavior, from conducting to insulating.

Molecule	**Conduction Gap (Volts)**	**E_f - HOMO (eV)**	**"Critical V_{set}" (Volts)**	**I_{set} (nA)**
TMXYL-TCNE	NA	NA	1.0	1.0
TMXYL-Flat	1.0 ± 0.25	0.25 ± 0.06	1.5	1.0
TMXYL-Upright	2.0 ± 0.5	0.5 ± 0.13	2.5	1.0
DDT	1.5 ± 0.5	0.4 ± 0.13	2.5	0.2
Alkane-Ester-	1.5 ± 0.5	0.4 ± 0.13	2.5	0.2
Alkane-Ester+	3.0 ± 0.5	0.8 ± 0.13	3.0	0.2
ODT	4.0 ± 0.5	1.0 ± 0.13	3.5	0.2
RC10TS	5.5 ± 0.5	1.4 ± 0.13	4.0	0.2

Table 9.2

When the total barrier width is kept fixed such as in the $\eta = 0.5$ condition, then the "critical" value of Vset must increase or decrease to compensate for changes in the value of I_{set}. The arrows represent a relative increase or decrease in the parameter listed above.

$D_{t\text{-}s}$	"Critical V_{set}"	I_{set}
Fixed		
Fixed		

9.3 Conclusions & Future

In this body of work, it has been shown that STM is a useful method for probing nanostructured materials and in particular, for performing conductance measurement on organic molecules. A new systematic technique resulting in a new characterization parameter, "critical V_{set}", has been developed. Additionally, simple models have been explored. The "simple barrier with a dielectric" model was shown to be insufficient to the task of modeling I(V) on molecules.

A variety of conductance behavior has been observed and includes conducting, semiconducting and insulating behavior. It was also demonstrated that the conductivity and I(V) behavior of molecules can be altered in a number of ways: 1) changing endgroups, 2) changing morphology, 3) a chemical doping event and 4) altering the orientation of an internal element within a molecule. A direct result of this work is the tabulated results (Table 9.1) for a small library of organic molecules.

There are several ways this work can be improved and expanded. One characterization technique that must be focused on is atomic resolution imaging of the SAMs. This has proven difficult except with the most stable of STM systems, and low noise in the tunnel current electronics is critical (this proved to be the primary hindrance to atomic resolution with the STM used for these studies). Atomic resolution provides clear evidence of SAM quality and would potentially allow the placement of the tip over specific areas of a molecule.

In the exploration of the correlation between "critical" V_{set} and the value of the voltage division factor, η, it would be most useful to have an independent feedback system to control tip-sample

separation, such as is found in conducting AFMs. The problems apparent with conducting AFM is the relatively more blunt tips which subsequently probe tens of molecules rather than one or a few (i.e. less than 10) molecules at a time. In essence, a marriage of these two techniques may provide the experimental apparatus required to fully explore STS and achieve the desired "two-terminal" electrical measurement on a molecule.

Finally, a more complete study on mono and dithiol versions of a molecule combined with the techniques described herein for changing molecular conduction would provide a more complete "big picture" of molecular electronics. A carefully designed project of this nature has the potential of demonstrating in full, the versatility of organic based molecular electronics that is suggested by the work presented herein. In particular, the systematic variation of V_{set} for fixed I_{set} is well suited to a study of this nature.

LIST OF REFERENCES

1. S.Datta, W.Tian, S.Hong, R.Reifenberger, J.I. Henderson, and C.P. Kubiak, Phys. Rev. Lett. **79**, 2530 (1997).

2. R.M. Feenstra, J.A. Stroscio, A.P. Fein, Surface Science **181**, 295 (1987).

3. R.M. Feenstra, Phys. Rev. Lett. **63**, 1412 (1989).

4. M. Dorogi, J.Gomez, R. G. Osifchin, R. P. Andres, R. Reifenberger, *Phys. Rev.* **B52**, 9071 (1995).

5. L. A. Bumm, J. J. Arnold, M. T. Cygan, T. D. Dunbar, T. P. Burgin, L. Jones II, D. L. Allara, J. M. Tour, P. S. Weiss, *Science* **271**, 1705 (1996).

6. L. A. Bumm, J. J. Arnold, L. F. Charles, T. D. Dunbar, D. L. Allara and P. S. Weiss, J. Am. Chem. Soc. **121**, 8017 (1999).

7. L.A. Bumm, J.J. Arnold, D.L. Allara and P.S.Weiss, J. Phys. Chem. **B102**, 8122 (1999).

8. F.T. Arce, M.E. Vela, R.C. Salvarezza and A.J. Arvia, Langmuir **14**, 7203 (1998).

9. W. Mizutani, T. Ishida and H. Tokumoto, Langmuir **14**, 7197 (1998).

10. H. Schönherr, G.J. Vancso, B. Huisman, F.C.J.M. van Veggel, and D.N. Reinhoudt, Langmuir **15**, 5541 (1999).

11. Y Xue, S. Datta, S. Hong, R. Reifenberger, J.I. Henderson, and C.P. Kubiak, Phys. Rev. **B59**, R7852 (1999).

12. S. Hong, W. Tian, J. Henderson, S. Datta , C. P. Kubiak , R. Reifenberger, *Superlattices and Microstructers* **28**, 289 (2000).

13. S. Raible, J Pfeiffer, T. Weiss, W. Clauss, W Goepel, V Schurig, D.P. Kern, *Appl. Phys.* **A70**, 607 (2000).

14. D. J. Wold, C. D. Frisbie, *J. Am. Chem. Soc.* **122**, 2971 (2000).

15. C. D. Bain, G. M. Whitesides, *Angew. Chem. Int. Ed. Engl.* **28**, 506 (1989).

16. C. D. Bain, E. B. Troughton, Y. T. Tao, J. Evall, G.M. Whitesides, *J. Am. Chem. Soc.* **111**, 321 (1989).

17. R.P. Andres, T. Bein, M. Dorogi, S. Feng, J.I. Henderson, C.P. Kubiak, W. Mahoney, R.G. Osifchin, and R. Reifenberger, Science **272**, 1323 (1996).

18. R.P. Andres, J.D. Bielefeld, J.I. Henderson, D.B. Janes, V.R. Kolagunta, C.P. Kubiak, W.J. Mahoney and R.G. Osifchin, Science **273**, 1690 (1996).

19.J.Jortner and M. Ratner, editors, *Coulomb blockade and digital single-electron devices*, Blackwell Science Ltd., Oxford, 1997.

20. J. Chen, M. A. Reed, A. M. Rawlett, and J. M. Tour, Science **286**, 1550 (1999).

21. D. S. Everhart, Chemtech **29** (4), 30 (1999).

22. T. Lee, J. Liu, J. Dicke, R. P. Andres, J. Lauterbach, M. R. Melloch, D. McInturff, J. M. Woodall, R. Reifenberger, *Appl. Phys. Lett.* **74**, 2869 (1999).

23. R. M. Metzger, *Acc. Chem. Res.* **32**, 950 (1999).

24. R.P. Andres, S. Datta, D.B. Janes, C.P. Kubiak and R. Reifenberger, Handbook of Nanostructured Materials and Nanotechnology, **3**, 179 (2000).

25. T.Lee, N. Chen, J. Liu, R.P. Andres, D.B. Janes, E.H. Chen, M.R. Melloch, J.M. Woodal, and R. Reifenberger, Appl. Phys. Lett. **76**, 212 (2000).

26. D. M. Collard, M. A. Fox, *Langmuir* **7**, 1192 (1991).

27. J. J. Hickman, P. E. Labinis, D. I. Auerbach, C. Zou, T. J. Gardner, G. M. Whitesides, M. S. Wrighton, *Langmuir* **8**, 357 (1992).

28. H. A. Biebuyck, G. M. Whitesides, *Langmuir* **9**, 1766 (1993).

29. M.A. Reed, C.Zhou, C.J. Muller, T.P. Burgin, and J.M. Tour, Science **278**, 252 (1997).

30. C. Kergueris, J.-P. Bourgoin, S. Palacin, D. Esteve, C. Urbina, M. Magoga, C. Joachim, *Phys. Rev* **B59**, 12505 (1999).

31. G. Leatherman, E.N. Duantini, D. Gust, T.A. Moore, A.L. Moore, S. Stone, Z. Zhou, P. Rez, Y.Z. Liu and S.M. Lindsay, *J. Phys. Chem.* **B103**, 4006 (1999)

32. S.Datta, *Electronic Transport in Mesoscopic Systems*, Cambridge University Press, Cambridge, 1995.

33. C.Joachim and J.F. Vinuesa, Europhys. Lett. **33**, 635 (1996).

34. M.P. Samanta, W.Tian, S.Datta, J.I. Henderson, and C.P. Kubiak, Phys. Rev. B **53**, 7626 (1996).

35. V.Mujica, M.Kemp, A.Roitberg, and M.A. Ratner, J. Chem. Phys. **104**, 7296 (1996).

36. W.Tian, S.Datta, S.Hong, R.Reifenberger, and J.I. Henderson, Physica E **1**, 304 (1997).

37. C.P. Tsu and R.A. Marcus, J. Chem. Phys. **106**, 584 (1997).

38. W.Tian, S.Datta, S.Hong, R.Reifenberger, J.Henderson, and C.Kubiak, J. of Chemical Physics **109**, 2874 (1998).

39. E. Emberly, G. Kirczenow, *Nanotechnology* **10**, 285 (1999).

40. M. D. Ventra, S. T. Pantelides, N.D. Lang, *Phys. Rev. Lett.* **84**, 979 (2000).

41. A. I. Onipko, K. -F. Berggren, Y. O. Klymenko, L. I. Malysheva, J. J. W. M. Rosink, L. J. Geerlings, E. van der Drift, S. Radelaar, *Phys Rev.* **61**, 11118 (2000).

42. John G. Simmons, J. of App. Phys. **34**, 1793 (1963).

43. J.A. Appelbaum and W.F. Brinkman, Phys. Rev. **186**, 464 (1969).

44. T.E.Feuchtwan, P.H. Cutler and N.M. Miskovsky, Phys Lett. **99**, 167 (1983).

45. A. Goswami, Quantum Mechanics, Wm. C. Brown Publishers, Dubuque IA (1992).

46. D. J. Griffiths, Introduction to Quantum Mechanics, Prentice-Hall, Englewood Cliffs, NJ (1995).

47. G. Binnig and H. Rohrer, Helv. Phys. Acta. **55**, 726 (1982).

48. G. Binnig and Rohrer, Surf. Sci. **152/153**, 17 (1985).

49 W.A. Hofer, A.J. Fisher, R.A. Wolkow and P. Grütter, Phys. Rev. Lett. **87**, (2001).

50. PID feedback control theory is available at:
http://newton.ex.ac.uk/teaching/CDHW/Feedback/SystemModel.html

51. PID Fabrication available at:
http://mechatronics.me.vt.edu/_vti_bin/shtml.exe/book/Section3/PID.html

52. Basics of Proportional-Integral_Derivative Control by Vance vanDoren available at:
Contol Engineering ONLINE (http://www.controleng.com)

53. J. Tersoff and D.R. Hamann, Phys. Rev. Lett. **50**, 1998 (1983).

54. J. Tersoff and D.R. Hamann, Phys. Rev. B **31**, 805 (1985).

55. C. Kittel, *Introduction to Solid State Physics 7th ed.*, John Wiley & Sons, New York, 1996.

56. D. A. McQuarrie and P. A. Rock, *General Chemistry 3rd ed.*, W. H. Freeman and Co., New York, 1991.

57. Ashcroft and Mermin, *Solid State Physics*, W. B. Saunders, Philadelphia, 1976.

58. K. L. Westra, "Tip Artifacts In Atomic Force Microscope Imaging of Thin Film Surfaces," J. App. Phys. **74**, 3608 (1993).

59. W.J. Kaiser and R.C. Jaklevic, *IBM J. Res. Develop.* **30**, 411 (1986).

60. L.H. Dubois and R.G. Nuzzo, *Annu. Rev. Phys. Chem.* **43**, 437 (1992).

61. H. Schönherr, G.J. Vancso, B. Huisman, F.C.J.M. van Veggel, and D.N. Reinhoudt, Langmuir **13**, 1567 (1997).

62. R.J. Hamers, R.M. Tromp, and J.E. Demuth, Phys. Rev. Lett. **56**, 1972 (1986).

63. P.E. Laibinis, B.J. Palmer, S. Lee and G.K. Jennings, *The Snthesis of Organothiols and Their Assembly into Monolayers on Gold*, in *Thin Films*, edited by A. Ulman, pages 1-41, Academic Press, San Diego, 1998.

64. M.D. Porter, T.B. Bright, D.L. Allara and C.E.D. Chidsey, *J. Am. Chem. Soc.* **109**, 3559 (1987).

65. S.W. Howell, *Ph.D. Thesis: "Electrostatic Force Microscopy Studies of Nanoscale Systems"*, Purdue University (2001).

66. C.A. Widrig, C.A. Alves and M.D. Porter, *J. Am. Chem. Soc.* **113**, 2805 (1991).

67. E. Delamarche, B. Michel, H.A. Biebuyck, C. Gerber, *Adv. Matter.* **8**, 719 (1996).

68. A. Dhirani, R.W. Zehner, R.P. Hsung, P.Guyot-Sionnest and L.R. Sita, *J. Am. Chem. Soc.* **118**, 3319 (1996).

69. J.P. Vigneron and Ph Lambin, J. Phys A: Math. Gen. **12**, 1961 (1979).

70. J.P. Vigneron and Ph Lambin, J. Phys A: Math. Gen. **13**, 1135 (1980).

71. J.P. Vigneron and Ph Lambin, J. Phys A: Math. Gen. **14**, 1815 (1981).

72. T.G. Miller, Ph.D. Thesis: "Studies in Layered High Temperature Superconductors With a Low Temperature Scanning Tunneling Microscope", Purdue University (1994).

73. W.R. Smythe, Static and Dynamic Electricity, McGraw-Hill, New York (1968).

74. A.M. Russell, J. of Appl. Phys. **53**, 970 (1962).

75. CRC Handbook of Chemistry and Physics 74th Edition, edited by D.R. Lide, CRC Press, Boca Raton (1993).

76. J.K. Gimezewski and R. Möller, Phys. Rev. **B36**, 1284 (1987).

77. J. Wintterlin, J. Wichers, H. Brune, T. Grisch, H. Höfer and R.J. Behm, Phys. Rev. Lett. **62**, 59 (1989).

78. Y. Kuk and P.J. Silverman, J. Vac. Sci. Tehnol. **A8**, 289 (1990).

79. R. Berndt, J.K. Gimzewski and R.R. Schlittler, Ultramicroscopy **42-44**, 528 (1992).

80. R. Schuster, J.V. Barth, J. Wintterlin, R.J. Behm and G. Ertl, Ultramicroscopy **42-44**, 533 (1992).

81. P. Avouris, I.-W. Lyo and Y. Hasegawa, J. Vac. Sci. Technol. **A11**, 1725 (1993).

82. J.H. Coombs and J.B. Pethica, IBM J. Res. Dev. **30**, 455 (1986).

83. L. Olesen, K. Hansen, E. Lægsgaard, I. Stensgaard and F. Besenbacher, *Metallic Nanowires: Formation and Quantized Conductance*, in *Nanowires*, edited by P.A. Serena and N. García, pages 191-210, Kluwer Academic Publishers, Netherlands, 1997.

84. H. Akamatsu, H. Inokushi, Y. Matsunaga, *Nature* **173**, 168 (1954).

85. L.B. Coleman, M.J. Cohen, D.J. Sandman, F.G. Yamagishi, A.F. Garrito, A.J. Hegger, *Solid State Commun.* **12**, 1125 (1973).

86. J. Ferraris, D.O. Cowan, J.V. Walatka, J.H. Perlstein, *J. Am. Chem. Soc.* **95**, 948 (1973).

87. T.J. Kistenmacher, T.E. Phillips, D.O. Cowan, *Acta Crystallogr. Sect.* **B30**, 763 (1974).

88. R.V. Gemmer, D.O. Cowan, T.O. Poehler, A.N. Bloch, R.E. Pyle, R.H. Banks, *J. Org. Chem.* **40**, 3544 (1975).

89. H. Shirakawa, E.J. Louis, A.G. MacDiarmid, C.K. Chiang, A.J. Heeger, *J Chem. Soc. Chem. Commun.*, 578 (1977).

90. A. Aumuller, P. Erk, S. Hunig, H. Meixner, J.U. von Schutz, H.P. Weiner, *Liebigs. Ann. Chem.*, 997 (1987).
91. S. Kagoshima, H. Nagasawa, T. Sambongi, *One-Dimentional Conductors*; Springer, Berlin, 1988.

92. S. Sakura, H. Anzai, *Electrochimica Acta* **38**, 2343 (1993).

93. S. Horiuchi, H. Yamoshi, G. Saito, K.I. Sakaguchi, M. Kusunoki, *J. Am. Chem. Soc.* **118**, 8604 (1996).

94. S. Hunig, K. Sinzger, M. Kemmer, U. Langhor, H. Rieder, S. Soderholm, J.V. von Schutz, H.S. Wolf, *Eur. J. Org. Chem.*, 1977 (1998).

95. C.J. Bender, *Chem. Soc. Rev.* **15**, 475 (1986).

96. M.R. Bryce, *Chem. Soc. Rev.* **20**, 355 (1991).

97. A.R. Lepley, *J. Am. Chem. Soc.* **86**, 2545 (1964).

98. R. Frank, P. V. Smith, *J. Am. Chem. Soc.* **68**, 2103 (1946).

99. Gaussian 98, Revision A.7, M. J. Frisch, G. W. Trucks, H. B. Schlegel, G. E. Scuseria, M. A. Robb, J. R. Cheeseman, V. G. Zakrzewski, J. A. Montgomery, Jr., R. E. Stratmann, J. C. Burant, S. Dapprich, J. M. Millam, A. D. Daniels, K. N. Kudin, M. C. Strain, O. Farkas, J. Tomasi, V. Barone, M. Cossi, R. Cammi, B. Mennucci, C. Pomelli, C. Adamo, S. Clifford, J. Ochterski, G. A. Petersson, P. Y. Ayala, Q. Cui, K. Morokuma, D. K. Malick, A. D. Rabuck, K. Raghavachari, J. B. Foresman, J. Cioslowski, J. V. Ortiz, A. G. Baboul, B. B. Stefanov, G. Liu, A. Liashenko, P. Piskorz, I. Komaromi, R. Gomperts, R. L. Martin, D. J. Fox, T. Keith, M. A. Al-Laham, C. Y. Peng, A. Nanayakkara, C. Gonzalez, M. Challacombe, P. M. W. Gill, B. Johnson, W. Chen, M. W. Wong, J. L. Andres, C. Gonzalez, M. Head-Gordon, E. S. Replogle,and J. A. Pople, Gaussian, Inc., Pittsburgh PA, 1998.

100. A. D. Becke, J. Chem Phys **98**, 5648 (1993).

101. J. P. Perdew and Y. Wang, Phys. Rev. B **45**, 13344 (1992).

102. D. A. Buchannan, IBM J. Res. Develop. **43**, 245 (1999).

103. S.-H. Lo, D. A. Buchannan, and Y. Taur, IBM J. Res. Develop. **43**, 327 (1999).

104. T. T.-T. Li and M. J. Weaver, J. Am. Chem. Soc. **106** 6107 (1984).

105. J. F. Smalley, S. W. Feldberg, C. E. D. Chidsey, M. R. Linford, M. D. Newton, and Y.-P. Liu, J. Phys. Chem. **99**, 13141 (1995).

106. S. B. Sachs, S. P. Dudek, R. P. Hsung, L. R. Sita, J. F. Smalley, M. D. Newton, S. W. Feldberg, and C. E. D. Chidsey, J. Am. Chem. Soc. **119**, 10563 (1997).

107. C.-P. Hsu and R. A. Marcus, J. Chem. Phys. **106**, 584 (1997).

108. D. Anselmetti, A. Bartoff, H. J. Guntherodt, E. Delamarche, B. Michel, Ch. Gerber, H. Kang, H. Wolf and H. Ringsdorf, Europhys. Lett. **27**, 365 (1994).

109 E. Delamarche, B. Michel, Ch. Gerber, D. Anselmetti, H. J. Guntherodt, H. Wolf and H. Ringsdorf, Langmuir **10**, 2869 (1994).

110. E. Delamarche, B. Michel, H. Kang and Ch. Gerber, Langmuir **10**, 4103 (1994).

111. G. E. Poitier and M. J. Tarlov, Langmuir **10**, 2853 (1994).

112. G. E. Poitier, M. J. Tarlov and H. E. Rushmeier, Langmuir **10**, 3383 (1994).

113. C. Schonenberger, J. Jorritsma, J. A. M. Sondag-Huethorst and L. G. J. Fokkink, J. Phys. Chem. **99**, 3259 (1995).

114. J. Kang and P. A. Rowntree, Langmuir **12**, 2813 (1996).

115. C. E. D. Chidsey, C. R. Bertozzi, T. M. Putvinski, and A. M. Mujsce, J. Am. Chem. Soc. **112**, 4301 (1990).

116. C. E. D. Chidsey and D. N. Loiacono, Langmuir **6,** 682, (1990).

117. E. U. Thoden van Velzen, J. F. J. Engbersen, and D. N. Reinhoudt, J. Am. Chem. Soc. **116**, 3597 (1994).

118. E. U. Thoden van Velzen, J. F. J. Engbersen, P. J. de Lange, J. W. G. Mahy, and D. N. Reinhoudt, J. Am. Chem. Soc. **117**, 6853 (1995).

119. E. U. Thoden van Velzen, J. F. J. Engbersen, and D. N. Reinhoudt, Synthesis, 989 (1995).

120. C.-J. Zhong, R. C. Brush, J. Anderegg, and M. D. Porter. Langmuir **15**, 518 (1999).

121 HyperChem AM1 Semi-emprical Geometry Optimization (Polak-Ribiere), 3-21G Single Point ab initio Orbital Calculation.

122 C.A. Alves, E.L. Smith and M.D. Porter, J. A. Chem. Soc. **114**, 1222 (1992).

123 D.D. Perrin and W.L.F. Armerego, *Purification of Laboratory Chemicals*, 4th Ed., Butterworth-Heinemann, Oxford, (1996).

APPENDIX A: Sample PERL code from the programs used to perform tunnel barrier simulations.

BAR11

BAR11.txt is the tunnel barrier simulation program. This program builds the tunnel barrier and runs either I(V) or I(Z) simulations based on parameters specified in **param11.txt** (shown below the sample code). The source code of BAR11.txt is written in PERL; samples of the code are shown below. Of particular interest are the subroutine which calculates the transmission through the barrier and the subroutine that generates the barrier.

```
# BAR11.txt
# Tunnel Barrier and Current Calculations
# Written by: Andre Labonte
# Last Updated: 9/14/2001

# SUBROUTINES
#*********************************************************************************
sub calctrans
{
# This subroutine calculates the transmission probability of an electron through a
# one-dimentionalenergy barrier using the Lambin-Vigneron numerical method for
# calculating transmission probability (J. Phys. A: Math, vol. 13, pp. 1135-1144, 1980).
# The following information must be passed to the subroutine:
#
# (name of array containing barrier, minimum energy, maximum energy,
#  number of steps in energy, number of steps in X, size of the step in X)
#
# The subroutine returns the reference to the array in which it placed the
# transmission data followed by the energy step size calculated.

# Variables Passed-In

     my $barrier = shift(@_);        # Reference to the array containing the barrier
     my $minenergy = shift(@_);      # minimum energy for which the transmission will be
calculated
     my $maxenergy = shift(@_);      # maximum energy for which the transmission will be
calculated
     my $numestep = shift(@_);       # number of steps in the energy between minenergy and
maxenergy
     my $numberofx = shift(@_);      # number of steps in X across the barrier
     my $xstep = shift(@_);          # size of the step in X.

# Variables Passed-Out

     my $transmission;               # Reference to the array that will contain the transmission numbers
     my $estep;                  # The energy step size to be calculated
```

```
# Loacal Constants & Variables

    my $schodinger = 2.6245674E1;       # 2 * electron mass / h-bar^2  in units of 1/(eV * nm^2)

    my $energy;             # energy at which the calculation is being done at

    my $beta1;              # The following variable are coeficients need for the
    my $beta3;              # Lambin-Vigneron method and follow the variable names
    my $reRminus;               # used in the referenced paper.
    my $imRminus;               #
    my $reRplus;                #
    my $imRplus;                #
    my $reRn;               #
    my $imRn;               #
    my $bn;                 #

    my $reNumerator;            # The following variable are used at the end to evaluate
    my $imNumerator ;           # the real and imaginary parts of the reflection coeficient.
    my $reDenominator;          #
    my $imDenominator;              #

    my $reflection;             # The reflection coeficient
    my @divide;                 # array used to tempararily store numbers from the complex
division subroutine


    $estep = ( ($maxenergy - $minenergy) / $numestep);
    $energy = $minenergy;

    for (my $m = 0; $m <= $numestep; $m++)
    {
        $beta1 = ( 2 + $schodinger * (($xstep)**2) * ($barrier->[0][1] - $energy) );
        $beta3 = ( 2 + $schodinger * (($xstep)**2) * ($barrier->[$numberofx + 1][1] - $energy) );

        if ($beta1 < 2)
        {
            $reRminus = $beta1 / 2;
            $imRminus = - ( 1 - (($beta1 / 2)**2) )**(1/2);
            $reRplus = $beta1 / 2;
            $imRplus = + ( 1 - (($beta1 / 2)**2) )**(1/2);
        }
        else
        {
            $reRminus = $beta1 / 2 + ( (($beta1 / 2)**2) - 1 )**(1/2);
            $imRminus = 0;
            $reRplus = $beta1 / 2 - ( (($beta1 / 2)**2) - 1 )**(1/2);
            $imRplus = 0;
        }

        if ($beta3 < 2)
        {
```

```
            $reRn = $beta3 / 2;
            $imRn = - ( 1 - (($beta3 / 2)**2) )**(1/2);
        }
        else
        {
            $reRn = $beta3 / 2 + ( (($beta3 / 2)**2) - 1 )**(1/2);
            $imRn = 0;
        }

        my $n = $numberofx;

        while ($n > 0)
        {
            $bn = 2 + $schodinger * (($xstep)**2) * ($barrier->[$n][1] - $energy);
            @divide = &complexdiv (1, 0, $reRn, $imRn);
            $reRn = $bn - $divide[0];
            $imRn = $divide[1];
            $n--;
        }

        $reNumerator = ($reRn - $reRminus);
        $imNumerator = ($imRn - $imRminus);
        $reDenominator = ($reRn - $reRplus);
        $imDenominator = ($imRn - $imRplus);
        @divide = &complexdiv ($reNumerator, $imNumerator, $reDenominator, $imDenominator);
        $reflection = ( ($divide[0])**2 + ($divide[1])**2 );
        $transmission->[$m][0] = $energy;
        $transmission->[$m][1] = (1 - $reflection);
        $energy = $energy + $estep;
    }
    return($transmission, $estep);
}


#*****************************************************************************
sub buildbarrier
{
# This subroutine builds a potential barrier based on a simple 1-dimentional vacuum gap with two
dielectic constants;
# it chages main program values.

    $hnumx = int ($parameters{numberofx}/2);
    $barrierwidth = $parameters{molheight} + $parameters{gapwidth};
    $xstep = $barrierwidth / ($parameters{numberofx} + 1);
    $x = $parameters{startx};

    if ($parameters{efermi1} < $parameters{efermi3})
    {
        $energyoffset = 0;
    }
    else
    {
```

```
        $energyoffset = $parameters{efermi3} - $parameters{efermi1};
    }

    $barrier[0][0] = $x;
    $barrier[0][1] = $energyoffset - $voltage;
    $maxenergy = $barrier[1][0];

    # numerical variables need if field-enhancment done
    if ($parameters{doFieldEnh} == 1)
    {
        $zetta = 1/((1 + $parameters{tipradius}/$barrierwidth)**0.5);
        $VnotMod = log((1+$zetta)/(1-$zetta));
        $fofT = log((1 - $zetta * $parameters{molheight} / $barrierwidth)/(1 + $zetta *
$parameters{molheight} / $barrierwidth));
        $alpha = ($parameters{dielectric} * $VnotMod) / ($parameters{dielectric} * $VnotMod +
$fofT * ($parameters{dielectric} - 1) );
    }

    for ($n = 1; $n <= $parameters{numberofx}; $n++)
    {
        $x = $x + $xstep;

        if ($parameters{doFieldEnh} == 1)
        {
            if ($parameters{molheight} == 0)
            {
                $trapazoid = (($parameters{workfunc3} - $parameters{workfunc1}) * ($x -
$parameters{startx}) / $barrierwidth) + ($parameters{efermi1} + $parameters{workfunc1} +
$energyoffset );
                $fieldvolts = -$voltage * (1 + log( ( 1-( $zetta*($x-
$parameters{startx})/$barrierwidth ) ) / ( 1+( $zetta*($x-$parameters{startx})/$barrierwidth ) ) ) /
$VnotMod);
            }
            elsif ($x - $parameters{startx} <= $parameters{molheight} && $parameters{gapwidth}
> 0)
            {
                $trapazoid = (($parameters{workfunc3} - $parameters{workfunc1}) * ($x -
$parameters{startx}) / ($parameters{molheight} + $parameters{dielectric} *
$parameters{gapwidth})) + ($parameters{efermi1} + $parameters{workfunc1} + $energyoffset );
                $midintercept = $trapazoid;
                $fieldvolts = -$voltage * (1 + $alpha * log( ( 1-( $zetta*($x-
$parameters{startx})/$barrierwidth ) ) / ( 1+( $zetta*($x-$parameters{startx})/$barrierwidth ) ) ) /
($VnotMod * $parameters{dielectric}) );
                $midvolt = ($fieldvolts + $voltage) * (1 - $parameters{dielectric}) ;
            }
            elsif ($x - $parameters{startx} <= $parameters{molheight} && $parameters{gapwidth}
<= 0)
            {
                $trapazoid = (($parameters{workfunc3} - $parameters{workfunc1}) * ($x -
$parameters{startx}) / $barrierwidth) + ($parameters{efermi1} + $parameters{workfunc1} +
$energyoffset );
```

```
                $fieldvolts = -$voltage * (1 + log( ( 1-( $zetta*($x-
$parameters{startx})/$barrierwidth ) ) / ( 1+( $zetta*($x-$parameters{startx})/$barrierwidth ) ) ) /
$VnotMod );
            }
            else
            {
                $trapazoid = ($parameters{dielectric} * ($parameters{workfunc3} -
$parameters{workfunc1}) * ($x - $parameters{startx} - $parameters{molheight}) /
($parameters{molheight} + $parameters{dielectric} * $parameters{gapwidth})) + ($midintercept);
                $fieldvolts = $midvolt - $voltage * (1 + $alpha * log( ( 1-( $zetta*($x-
$parameters{startx})/$barrierwidth ) ) / ( 1+( $zetta*($x-$parameters{startx})/$barrierwidth ) ) ) /
$VnotMod );
            }
        }
        else
        {

            $fieldvolts = 0;

            if ($parameters{molheight} == 0)
            {
                $trapazoid = (($parameters{workfunc3} + $voltage - $parameters{workfunc1}) *
($x - $parameters{startx}) / $barrierwidth) + ($parameters{efermi1} + $parameters{workfunc1} +
$energyoffset - $voltage);
            }
            elsif ($x - $parameters{startx} <= $parameters{molheight} && $parameters{gapwidth}
> 0)
            {
                $trapazoid = (($parameters{workfunc3} + $voltage - $parameters{workfunc1}) *
($x - $parameters{startx}) / ($parameters{molheight} + $parameters{dielectric} *
$parameters{gapwidth})) + ($parameters{efermi1} + $parameters{workfunc1} + $energyoffset -
$voltage);
                $midintercept = $trapazoid;
            }
            elsif ($x - $parameters{startx} <= $parameters{molheight} && $parameters{gapwidth}
<= 0)
            {
                $trapazoid = (($parameters{workfunc3} + $voltage - $parameters{workfunc1}) *
($x - $parameters{startx}) / $barrierwidth) + ($parameters{efermi1} + $parameters{workfunc1} +
$energyoffset - $voltage);
            }
            else
            {
                $trapazoid = ($parameters{dielectric} * ($parameters{workfunc3} + $voltage -
$parameters{workfunc1}) * ($x - $parameters{startx} - $parameters{molheight}) /
($parameters{molheight} + $parameters{dielectric} * $parameters{gapwidth})) + ($midintercept);

            }
        }

        if ($parameters{doImChrg} == 1)
        {
```

```
            $imagepot = (1.15 * $echarge * $ln2 * $barrierwidth * $nano) / (16 * $pi * $epsilon0 *
($x - $parameters{startx}) * $nano * $nano * ($barrierwidth - ($x - $parameters{startx})));
        }
        else
        {
            $imagepot = 0;
        }


        if ($parameters{doShockey} == 1 && ($x - $parameters{startx}) <
$parameters{shockeywidth})
        {
            $shockey = (- $parameters{shockeyheight} / $parameters{shockeywidth} ) * ($x -
$parameters{startx}) + $parameters{shockeyheight};
        }
        else
        {
            $shockey = 0;
        }

        $barrier[$n][0] = $x;
        $temp = ($trapazoid + $fieldvolts - $imagepot + $shockey);
        $temp2 = ($parameters{efermi1} - $parameters{efermi3} + $energyoffset);

        if ($n < $hnumx)
        {
            if ($parameters{doShockey} == 1 && $parameters{doImChrg} == 1 && ($x -
$parameters{startx}) < $parameters{shockeywidth})
            {
                $barrier[$n][1] = ($trapazoid + $fieldvolts - (($x -
$parameters{startx})/$parameters{shockeywidth}) * $imagepot + $shockey);
            }
            elsif ($temp < $barrier[0][1])
            {
                $barrier[$n][1] = $barrier[0][1];
            }
            else
            {
                $barrier[$n][1] = ($trapazoid + $fieldvolts - $imagepot + $shockey);
            }
        }
        else
        {
            if ($temp < $temp2)
            {
                $barrier[$n][1] = ($parameters{efermi1} - $parameters{efermi3} + $energyoffset);
            }
            else
            {
                $barrier[$n][1] = ($trapazoid + $fieldvolts - $imagepot + $shockey);
            }
        }
```

```
        if ($maxenergy < $barrier[$n][1])
        {
            $maxenergy = $barrier[$n][1];
        }
    }

    $barrier[$n][0] = $x + $xstep;
    $barrier[$n][1] = ($parameters{efermi1} - $parameters{efermi3} + $energyoffset);

    if ($maxenergy < $barrier[$n][1])
    {
        $maxenergy = $barrier[$n][1];
    }
}
```

Param11

param11.txt is the file that contains all the conrol parameters required by **BAR11.txt**. The use of a separate parameter file was motivated by the need to alter simulations quickly and easily. One example of paramll.txt is shown below.

Voltage(V)	setvoltage	-0.5
Current(nA)	setcurrent	1.1
error(nA)	currenttol	0.05
FermiLevel1(eV)	efermi1	9
FermiLevel3(eV)	efermi3	9
WorkFunction1(eV)	workfunc1	5.31
WorkFunction3(eV)	workfunc3	5.7
StartingX	startx	0
MoleculeHight(nm)	molheight	0
GapWidth(nm)	gapwidth	1.0
StopWidth(nm)	stopwidth	0.0
Dielectric	dielectric	1
ShockeyHeight(eV)	shockeyheight	0
ShockeyWidth(nm)	shockeywidth	0
TipRadius(nm)	tipradius	2.4
XIncriments	numberofx	1000
EnergyIncriments	numestep	100
VoltageIncriments	numvstep	50
ZIncriments	numzstep	50
DoTransmission(yes=1)	doT	1
DoCurrentInt(yes=1)	doI	1
DoFeedback(yes=1)	doFeedback	1
DoI(V)(yes=1)	doIV	1
DoDI/DV(yes=1)	doDIDV	1
DoImageCharge(yes=1)	doImChrg	1
DoI(Z)(yes=1)	doIZ	0
DoShockeyBarrier(yes=1)	doShockey	0
DoFieldEnhanced(yes=1)	doFieldEnh	1

APPENDIX B: Barrier Equation for tunnel barrier with a dielectric layer

The following is a derivation of the field enhanced potential when a dielectric layer is present in an STM tunnel junction as shown in Figure 5.19. From equation 5.17 we find that the potential in the dielectric layer is given by:

$$V_{dielectric}(z) = -V_0\left[1 + \frac{A}{k\ \ln\left[\frac{1+h_e}{1-h_e}\right]}\ln\left[\frac{1-\frac{h_e z}{D_{t-s}}}{1+\frac{h_e z}{D_{t-s}}}\right]\right] \quad \text{B1}$$

where k is the dielectric constant and A is a constant to be found by matching boundary conditions. In the region of the tunnel gap (between the dielectric layer and tip) the potential is given by

$$V_{gap}(z) = -V_0\left[1 + \frac{A}{\ln\left[\frac{1+h_e}{1-h_e}\right]}\ln\left[\frac{1-\frac{h_e z}{D_{t-s}}}{1+\frac{h_e z}{D_{t-s}}}\right]\right] + C \quad \text{B2}$$

Where C is found by matching boundary conditions. Now we match boundary conditions: at the grounded tip V = 0 and Z = $D_{t\text{-}s}$, thus, from equation B2 we find

$$A = \frac{V_0 - C}{V_0} \quad \text{B3}$$

At the dielectric-gap interface (i.e. Z = T where T = dielectric thickness), $V_{dielectric} = V_{gap}$. Solving for C we get:

$$C = [-V_{dielectric}(T) - V_0] \bullet [k-1] \quad \text{B4}$$

and finally solving for A:

$$A = \frac{kg}{kg + (k-1)f(T)}$$

where

$$f(T) = \ln\left[\frac{1 - \frac{h_e T}{D_{t-s}}}{1 + \frac{h_e T}{D_{t-s}}}\right]$$

and

$$g = \ln\left[\frac{1+h_e}{1-h_e}\right]$$

APPENDIX C: Supplemental Sample Information

Au Substrate Preperation

All substrates consist of a layer of Cr (1-4 nm) and Au (200-300 nm) evaporated onto a borosilicate glass. Before use, all Au substrates are front-side flamed until bright red for 30 to 40 seconds producing flat grains of a few microns in diameter having a Au (111) orientation. Just prior to use, all wafers were rinsed in distilled ethanol to remove residual contamination.

TMXYL Synthesis

Synthesis of 2, 3, 5, 6-Tetramethyl-*p*-xylene-α, α' dithiol (TMXYL). This work was performed by Bala Sundari T. Kasibhatla, Department of Chemistry & Biochemistry, University of California San Diego, La Jolla, CA 92093-0358. The information shown below is a summary of Bala's work and is shown here for completeness since these results are yet unpublished.

TMXYL was synthesized by a modification of existing procedure [R. Frank and P.V. Smith, *Am. Chem. Soc.* ***68,*** 2103 (1946)]. 2, 3, 5, 6-tetramethyl -*p*-xylene-α, α'-diol (5.5g; 0.028 mol) was placed in a 3-necked, 100mL flask, along with 70mL acetonitrile. The solid was dissolved with heating and stirring, followed by the addition of thiourea (4.3g; 0.056 mol) and approximately 40mL water. Next, aqueous 48 wt% HBr (28.1g; 0.169 mol) was added to the solution, which was then refluxed, with stirring, for 30-36 hours. To the reaction mixture, 67.4mL of 2.5M aqueous KOH was added, and the mixture refluxed for 12 hours under nitrogen. It was then allowed to cool to room temperature whereupon a pale yellow solid precipitated. The solid was dissolved in $CHCl_3$, dried over anhydrous $MgSO_4$, and solvent removed under reduced pressure. The solid was then loaded on a silica gel column (60-200 mesh) and eluted with a 9:1 mixture of hexanes:EtOAc to obtain 4.52g (71% yield) of a white crystalline material. IR (KBr): ν(SH), 2549cm^{-1} (weak). ^{1}H NMR ($CDCl_3$): 1.52 ppm (t, 2H), 2.3 ppm (s, 12H), 3.8 ppm (d, 4H). ^{13}C NMR ($CDCl_3$): 16.2 ppm, 24.3 ppm, 132.3 ppm, 136.3 ppm.

MS: 226 (M+), 193 (M - SH), 161. C, H, N (vs. *calcd.*): 63.68% C (*63.66%*), 8.00% H (*8.00%*), 28.22% S (*28.32%*).

Doping Project SAM Preperation

A SAM of TMXYL, was prepared by immersing a clean Au(111) wafer into ca. 1mM CH_2Cl_2 solutions of the respective compound for 12-16 hours. The wafers were then thoroughly rinsed with CH_2Cl_2 and dried overnight under a stream of nitrogen. A SAM of TMXYL-TCNE, **2**, was prepared by immersing a Au(111) wafer previously coated with **1**, in a concentrated solution of TCNE in CH_2Cl_2, for 48 hours. The wafer was rinsed with CH_2Cl_2 and dried under nitrogen. A SAM of TMXYL with two thiol bonds to the Au(111) surface, **3**, was prepared by immersing the TMXYL-TCNE SAM, **2**, in a concentrated solution of Trimethyltetrathiafulvalene (Me_3TTF) in CH_2Cl_2 for 30 hours.

Alkane-Ester Synthesis

The synthesis of the two target disulfide esters **1** (alkane-ester-) and **2** (alkane-ester+) is discussed briefly below. The overall synthesis scheme is represented schematically in Figure C1.

The synthesis of 6-(5-pentyloxycarbonyl-pentyldisulfanyl)-hexanoic acid pentyl ester **1** began with the conversion of commercially available 1-bromohexanoic acid to mercaptohexanoic acid **3** *via* the *in situ* hydrolysis of the *iso*-thiouronium salt formed in the reaction of 1-bromohexanoic acid with thiourea. After purification of the mercaptohexanoic acid **3** *via* flash column chromatography, iodine induced oxidation of the mercaptohexanoic acid **3** to the disulfide in the presence of pentanol afforded 6-(5-pentyloxycarbonyl-pentyldisulfanyl)-hexanoic acid pentyl ester **1**. The purification of ester **1** was achieved by evaporation of the excess pentanol, washing the iodine residue out with sodium thiosulfate solution and finally flash column chromatography.

The synthesis of hexanoic acid 5-(5-hexanoyloxy-pentyldisulfanyl)-pentyl ester **2** began with the BBr_3 induced, bromination accompanied, ring opening of tetrahydropyran to afford 1-bromopentanol

4. Following purification *via* flash column chromatography, 1-bromopentanol **4** was found to slowly decompose at room temperature and so was stored at -20 °C until its conversion to mercaptopentanol **5** *via* the *in situ* hydrolysis of the *iso*-thiouronium salt formed in the reaction of 1-bromopentanol **4** with thiourea. After flash column chromatographic purification, mercaptopentanol **5** was converted to the corresponding disulfide *via* iodine induced oxidation. Purification of dipentanol disulfide **6** was achieved by washing the iodine residue out with sodium thiosulfate solution followed by flash column chromatography. Reaction of disulfide **6** with hexanoic acid in the presence of DCC / DMAP afforded hexanoic acid 5-(5-hexanoyloxy-pentyldisulfanyl)-pentyl ester **2** in good yield after flash column chromatography.

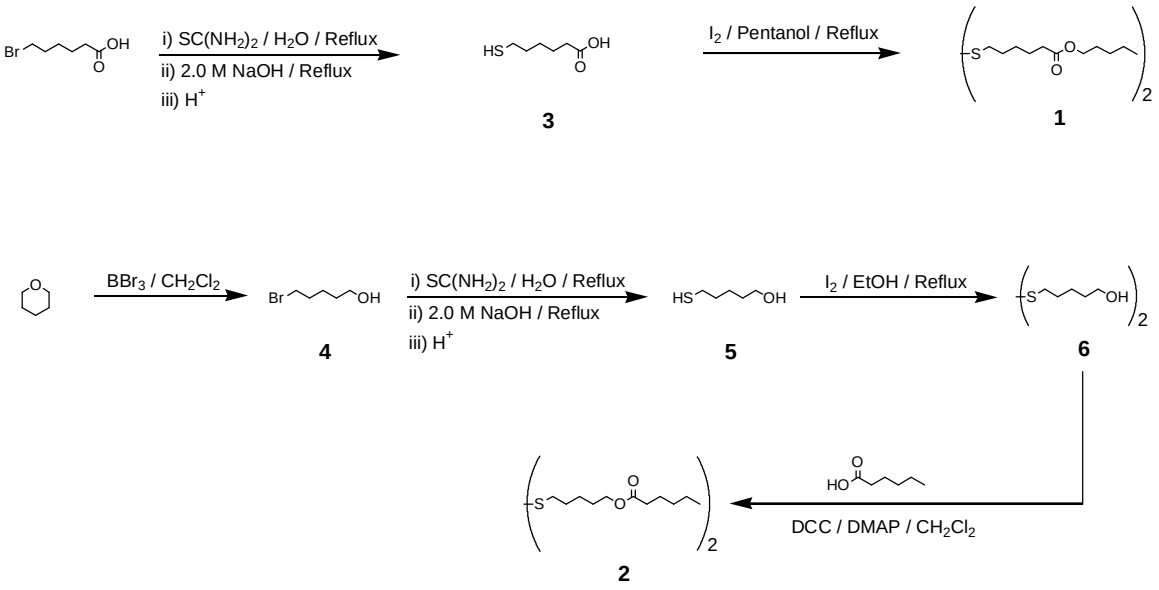

Figure C1

Synthesis of compounds **1-6.**

All chemicals were purchased from the Aldrich Chemical Company and were used as received. Solvents were either used as received or dried (CH_2Cl_2 from CaH_2 under a N_2 atmosphere) according to procedures described in the literature.[123] Thin layer chromatography (TLC) was performed on

aluminium sheets coated with kieselgel 60 F_{254} (Merck 5554). After development, plates were initially scrutinised under ultraviolet light, stained with I_2 vapour or treated with a 5% solution of H_2SO_4 (EtOH) followed by charring. Flash column chromatography was carried out using kieselgel 60 F_{254} (Merck 9385, 230-400 mesh). Electron impact ionisation mass spectra (EIMS) were recorded on a VG Zabspec spectrometer. Chemical ionisation mass spectra (CI) were recorded on a VG ProSpec mass spectrometer with ammonia as the reactant gas. Nuclear magnetic resonance (NMR) spectra were recorded on a Brucker AC300 spectrometer operating at 300 MHz (^{1}H) or 75.5 MHz (^{13}C, PENDANT pulse sequence) using a deuterated solvent as the lock and the residual solvent as the internal reference. Elemental microanalysis was performed using an EA 1110 (Carlo-Erba) microanalysis instrument. Fourier transform infrared spectra were recorded on a 1600 FTIR (Perkin-Elmer) spectrometer utilising a thin film (KBr plates) for liquids or incorporating a finely ground sample in a compressed KBr disc for solids.

SAMs of both **1** and **2** were formed on Au(111) substrates. Substrates were rinsed sequentially in deionized water and ethanol, and then soaked overnight in millimolar solutions of the appropriate molecule.

VITA

André Paul Labonté was born December 30, 1972 in Point Claire, Quebec, Canada, the son of Jean Paul and Eva Labonté. He grew up in Lewiston, Maine and graduated from the University of Maine in 1996 with a B.S. in engineering physics with a concentration in electrical engineering. He married Janice Lynn Dent on July 6, 1996 and subsequently had two children, Chandra Anne and Benjamin Dale. Janice passed away November 1, 1999 in an automobile accident. André entered the physics program at Purdue University in 1996